Title
Dynamic Change of Totten Glacier, East Antarctica

Permalink
https://escholarship.org/uc/item/8qt6g2cw

Author
Li, Xin

Publication Date
2016

Peer reviewed|Thesis/dissertation

UNIVERSITY OF CALIFORNIA,
IRVINE

Dynamic Change of Totten Glacier, East Antarctica

DISSERTATION

submitted in partial satisfaction of the requirements
for the degree of

DOCTOR OF PHILOSOPHY

in Earth System Science

by

Xin Li

Dissertation Committee:
Prof. Eric Rignot, Chair
Prof. Mathieu Morlighem
Prof. Eric Saltzman

2016

TABLE OF CONTENTS

LIST OF FIGURES

LIST OF TABLES

ACKNOWLEDGMENTS

I have been very fortunate to work with my advisor Eric Rignot. He took me as a Ph.D. student in 2010, by the time I had no background in glaciology. He has been very patient and supportive over the past five years. His broad knowledge, keen insights and deep experience in the field of glaciology guided me through this project. He set a great example for me in my future academic career.

This project would not have been possible without the support and help from a lot of people. Jeremie Mouginot taught me how to process satellite data from the very beginning. He always kept his door open, he helped me solve technical problems and discussed my research with me. I would like to thank Bernd Scheuchl for his advice and encouragement. Mathieu Morlighem, Eric Saltzman, Eric Larour and Todd Dupont served on my committee, they gave me many constructive suggestions about my research along the way. Helene Seroussi, Ala Khazendar, Michael Schodlok and Benoit Legresy have been great collaborators and provided me many inspiring perspectives.

I was lucky to be a part of the cryosphere group at University of California, Irvine. I learned a lot from the weekly meetings. I thank the other graduate students in our group, Yun Xu, Lu An, Hongju Yu and Cilan Cai. Their company and encourage helped me survive graduate school. I also thank other people in Department of Earth System Science. I enjoyed the classes and the atmosphere here.

I thank my parents and friends for their love, company and support in the past five years. They kept my spirit up during difficult times.

Parts of Chapter 2 and 4 are reprinted from a publication in Geophysical Research Letters with permission from John Wiley and Sons. Parts of Chapter 3 and 5 are reprinted from a publication recently submitted to Geophysical Research Letters with permission from all coauthors. Part of Chapter 2 is reprinted from a conference paper in 10th European Conference on Synthetic-Aperture Radar (EUSAR) with permission from all coauthors.

CURRICULUM VITAE

Xin Li

EDUCATION

Doctor of Philosophy in Earth System Science   **2016**
University of California, Irvine   *Irvine, California*

Master of Science in Earth System Science   **2012**
University of California, Irvine   *Irvine, California*

Bachelor of Science in Physical Geography   **2010**
Nanjing University   *Nanjing, CHINA*

RESEARCH EXPERIENCE

Graduate Research Assistant   **2010–2015**
Advisor: Prof. Eric Rignot   *UC Irvine*

TEACHING EXPERIENCE

The Atmosphere Instructor   **Summer 2015**
Department of Earth System Science   *UC Irvine*

Introduction to Earth System Science Teaching Assistant   **Fall 2014**
Instructor: Dr. Julie Ferguson   *UC Irvine*

The Atmosphere Teaching Assistant   **Spring 2014**
Instructor: Dr. Julie Ferguson   *UC Irvine*

Introduction to Earth System Science Teaching Assistant   **Fall 2012**
Instructor: Dr. Julie Ferguson   *UC Irvine*

The Atmosphere Teaching Assistant   **Spring 2012**
Instructor: Dr. Julie Ferguson   *UC Irvine*

Physical Environment Teaching Assistant   **Fall 2011**
Instructor: Prof. Todd Dupont   *UC Irvine*

PUBLICATIONS

Li, X., E. Rignot, M. Morlighem, J. Mouginot and B. Scheuchl (2015), Grounding line retreat of Totten Glacier, East Antarctica, 1996 to 2013, *Geophys. Res. Lett., 42.*

Li, X., E. Rignot, J. Mouginot and B. Scheuchl (2016), Ice flow dynamics and mass loss of Totten Glacier, East Antarctica from 1989 to 2015, *Geophys. Res. Lett., in review.*

Xu, Y., E. Rignot, D. Menemenlis, J. Mouginot, B. Scheuchl, **X. Li**, M. Morlighem, M. van den Broeke, I. Fenty and C. Cai (2016), Modeling of the ocean-induced ice melting speed of West Greenland glaciers over the past decades, *Geophys. Res. Lett., in review*

Mouginot, J., B. Scheuchl, E. Rignot and **X. Li** (2014), Monitoring Polar Ice Sheets using TanDEM-X, in *10th European Conference on Synthetic Aperture Radar (EUSAR)*, pp. 858-861.

CONFERENCE PRESENTATIONS

Li, X., E. Rignot, J. Mouginot, B. Scheuchl and L. An (2015), Changes in ice dynamics of Totten Glacier, East Antarctica in the past two decades, *2015 AGU Fall Meeting*

Li, X., E. Rignot, J. Mouginot, B. Scheuchl and L. An (2014), Changes in ice flow dynamics of Totten Glacier, East Antarctica and impacts on ice mass balance, *2014 AGU Fall Meeting*

Li, X., J. Mouginot and E. Rignot (2013), Observations of changes in ice flow of Totten Glacier, East Antarctica, *2013 AGU Fall Meeting*

Li, X., E. Rignot, J. Mouginot, B. Scheuchl and B. Legresy (2012), Observations on the ice flow structure of Totten Glacier, East Antarctica, *2013 AGU Fall Meeting*

Li, X., E. Rignot, M. Morlighem and J. Mouginot (2012), Basal drag pattern and grounding line sensitivity of the ice flow of Totten Glacier, East Antarctica, *2012 IGS Symposium*, Fairbanks, Alaska.

Li, X., E. Rignot, M. Morlighem, H. Seroussi, E. Larour, J. Mouginot, B. Scheuchl, D. Young and D. Blankenship (2011), Basal drag pattern and grounding line sensitivity of the ice flow of Totten Glacier, East Antarctica, *2013 AGU Fall Meeting*

ABSTRACT OF THE DISSERTATION

Dynamic Change of Totten Glacier, East Antarctica

By

Xin Li

Doctor of Philosophy in Earth System Science

University of California, Irvine, 2016

Prof. Eric Rignot, Chair

Totten Glacier, East Antarctica, a glacier that holds a 3.9 m sea level change equivalent, has thinned and lost mass for decades. Change in surface elevation calculated from high-resolution DEM differencing shows significant surface lowering rates concentrated in areas of fast flow, hence is probably of dynamic origin. A 26-year long ice velocity time series (1989-2015) consisting of 13 maps is developed from Landsat and interferometric synthetic aperture radar (InSAR) data. We find significant speed-up in ice velocity, especially in 2002-2007, followed by a period of slow decrease in 2010-2014. Comparing the ice discharge with surface mass balance suggests that the glacier mass balance was already negative in 1996 and became more negative into the 2000s. Grounding line mapping using differential InSAR, combined with high resolution topographies of the ice surface and ice draft, reveals a 1,500-2,300 m deep grounding zone. The grounding line extends 15 km inland along two prominent side lobes. Immediately upstream of the grounding line, there is an ice plain which is slightly grounded, only 15-50 m above hydrostatic equilibrium. At the glacier center, we detect a retreat of the grounding line up to 2.6±0.1 km by comparing differential InSAR data acquired 17 years apart. The retreat is asymmetrical along the two lobes, but consistently indicates a total thinning of 11.9±1.5 m from 1996 to 2013. On the ice plain, the glacier is prone to rapid retreat around a region about 7 km long, but inland the bed elevation rises. Sustained thinning will cause further retreat and speed up, but will not be conducive to a

marine ice sheet instability. The ultimate cause of the changes is not known, but probably of oceanic origin. Comparison of the velocity time series and reanalysis sub-surface ocean temperatures indicates that Totten Glacier may be very sensitive to oceanic perturbations.

Chapter 1

Introduction

Proxy records show abrupt global sea level rise 19,000 years ago (*Clark et al.*, 2004). The rapid sea level rise was associated with meltwater pulse, indicating significant contribution from ice sheets (*Clark et al.*, 2004). Observations suggest a sea level rise rate of 3.2±0.4 mm/yr over the period 1993-2010, with an Antarctic contribution of 0.27±0.09 mm/yr (*Church et al.*, 2013). There is a large uncertainty in projections of Antarctic contribution to future sea level rise, because of the poor understanding of ice sheet mass balance and a lack of observations.

Totten Glacier has the largest ice discharge (71±3 Gt/yr) of any glacier in East Antarctica (*Rignot et al.*, 2013). If all the ice in its drainage basin were to melt into the ocean, the global sea level would rise by 3.9 m (*Li et al.*, 2015a). In recent decades, significant thinning (*Pritchard et al.*, 2009) and mass loss (*Velicogna et al.*, 2014) has been observed on this glacier. However, the cause of thinning and related dynamic processes are unclear. In order to better understand the dynamics and mass balance of Totten Glacier, we need a comprehensive observational record of the evolution of the glacier to understand its dynamics and mass budget.

This dissertation presents a comprehensive collection of observational records on Totten Glacier over the past 26 years. Chapter 1 gives an overview of the background information of this study. Chapter 2, 3, and 4 discuss the observed dynamical change, and the total mass balance is presented in Chapter 5.

Chapter 2 reviews the ice-sheet topography and changes in surface elevation of Totten Glacier. Results from section 2.1.2, 2.2.2, 2.3 and 2.4.1 are original work from this study. Contents of section 2.1.2, 2.2.2 and 2.3 are published in *Li et al.* (2015a). The elevation change analysis from section 2.4 is published in a conference paper (*Mouginot et al.*, 2014a).

13 years of ice velocity spanning 26 years are derived from satellite optical and synthetic aperture radar (SAR) data. Four different processing approaches have been used to map the ice velocity from different data types. Chapter 3 discusses the velocity change on Totten Glacier. The 2007-2009 velocity record is from *Rignot et al.* (2011a), with the rest from this study. The results in this chapter is summarized in a manuscript submitted to Geophysical Research Letters (*Li et al.*, 2015b).

The grounding line of Totten Glacier is mapped in 1996 and 2013 using interferometric SAR (InSAR) data. The analysis of the grounding line is described in Chapter 4, with related results published in *Li et al.* (2015a).

All the results mentioned are synthesized to assess the mass balance of the glacier. The mass balance estimates are presented in Chapter 5, with results summarized in *Li et al.* (2015b).

The evolution of Totten Glacier over the 26 years is summarized in Chapter 6. In this chapter, the technical limitation and scientific implications of this study are discussed as well.

1.1 Background

In the 20th century, the global sea level has been rising persistently at a rate of 1.7 mm/yr (*IPCC*, 2013). This rate almost doubled in the past 20 years, and is very likely to keep increasing in the coming century (*IPCC*, 2013). Thermal expansion of seawater due to climate warming, and mass loss from glaciers and ice sheets have been thus far the dominant contributors to global sea level rise for the past century. The most recent report from the Intergovernmental Panel of Climate Change (IPCC) estimated 0.27±9 mm/yr sea level rise contribution from Antarctica, the world's largest ice sheet (*IPCC*, 2013). As summarized in Section 1.2, the mass loss from Antarctica is mostly dynamic, through increased ice flow from the peripheral outlet glaciers.

Scientific evidence reveals a strong increase in ice discharge in West Antarctica and the Antarctic Peninsula over the past decade (*Rignot*, 2008; *Thomas et al.*, 2004; *Mouginot et al.*, 2014b). In comparison, East Antarctica remains in near balance. However, the mass balance of East Antarctica is far from being spatially homogeneous. Totten Glacier, the biggest ice discharger in East Antarctica (*Rignot et al.*, 2013), has been thinning and losing mass for the past decade (*Pritchard et al.*, 2009; *Chen et al.*, 2009; *Rignot*, 2002; *Rignot et al.*, 2008). The drainage basin of Totten Glacier sits deep below sea level, potentially conducive to a marine ice sheet instability. This dissertation therefore focuses on the evolution of this glacier over the past 26 years.

Most of the dynamic changes of the Antarctic ice sheet are observed in marine-based sectors, indicating a potential instability in these regions. Paleoclimate records and process-based numerical models suggest possible abrupt, irreversible retreat and mass loss of these marine-based sectors in response to the ongoing climate change, through a dynamic process called the marine ice sheet instability, as explained in section 1.3.

Antarctica is probably the least-known landscape on this planet. Observations used to

be difficult due to its vastness and remoteness. Spaceborne and airborne remote sensing techniques have revolutionized the study of polar ice sheets by providing accurate, large-scale, high density data to help constrain and validate ice sheet models. By simulating the governing physical processes of the ice sheet system, the models can expand the short observational records to long term trends and further predict the future response of the ice sheet to climate change. A summary of the established remote sensing techniques is presented in section 1.4.

1.2   Mass balance of the Antarctic ice sheet

1.2.1   Large sea level rise potential of the Antarctic ice sheet

Holding more than 2×10^7 Gt of ice (*Marshall*, 2012), the Antarctic ice sheet is the largest reservoir of fresh water on Earth, capable of raising the global sea level by 56 m (*Marshall*, 2012). The mass loss from Antarctic ice sheet is an imminent threat to future sea level rise under a warming climate. During the last interglacial period ($\sim$125,000 years ago) when the Earth's surface temperature was 2°C warmer, global sea level was 5-10 m higher than present (*Kopp et al.*, 2009; *Dutton and Lambeck*, 2012). The high sea level in part results from disintegration of the Antarctic ice sheet. Records and reconstructions of past sea level provide evidence of rapid sea level rise due to discharge from continental ice sheets in Earth's history (*Clark et al.*, 2004; *Deschamps et al.*, 2012).

1.2.2   Methods of estimating ice sheet mass balance

The ice sheets gain mass through snowfall accumulation and lose mass through surface melting, iceberg calving and basal melting. The ice sheet mass balance is the difference

between mass gain and mass loss. There are three widely-used approaches to determine the mass balance of ice sheets. Firstly, satellite time-variable gravity survey from the Gravity Recovery and Climate Experiment (GRACE) mission provides direct measurements on the mass change of the ice sheets (*Velicogna and Wahr*, 2006; *Velicogna*, 2009; *Chen et al.*, 2009). The second approach makes use of satellite altimetry data and integrates the elevation change of the ice sheet to derive its mass balance (*Shepherd and Wingham*, 2007; *McMillan et al.*, 2014; *Pritchard et al.*, 2012). Lastly, one can compare the snowfall accumulation with the mass output to estimate the mass budget of the ice sheet and determine its mass balance (*Rignot*, 2002; *Rignot et al.*, 2008). Most of the Antarctic ice sheet will stay below the freezing point in the recent future despite of the warming climate (*Kuipers Munneke et al.*, 2012), therefore ice discharge from outlet glaciers is the only source of mass output in Antarctica. Each method has its own strengths and weaknesses, further details on these methods of estimating ice sheet mass balance will be provided in Chapter 5.

1.2.3 Contemporary Antarctic ice sheet mass balance

Table 1.1 summarizes the estimated mass balance of Antarctic ice sheet documented in the literature. Considerable uncertainties still remain in these estimates, especially for East Antarctica. Most studies reported a negative mass balance for West Antarctica driven by ice dynamics in the Amundsen Sea sector and the Antarctic Peninsula (Figure 1.1). In comparison, East Antarctica remains fairly stable, or perhaps even gaining mass. The dynamic ice loss over Wilkes and Victoria Land is largely compensetated by increased accumulation along the coast of Dronning Maud Land. Increasing mass loss is also detected in several regions where ice dynamics plays the most important role.

The Amundsen Sea Embayment in West Antarctica drains more ice than any other outlet glacier in Antarctica. It is now the most active sector of Antarctic ice sheet. Changes in ice
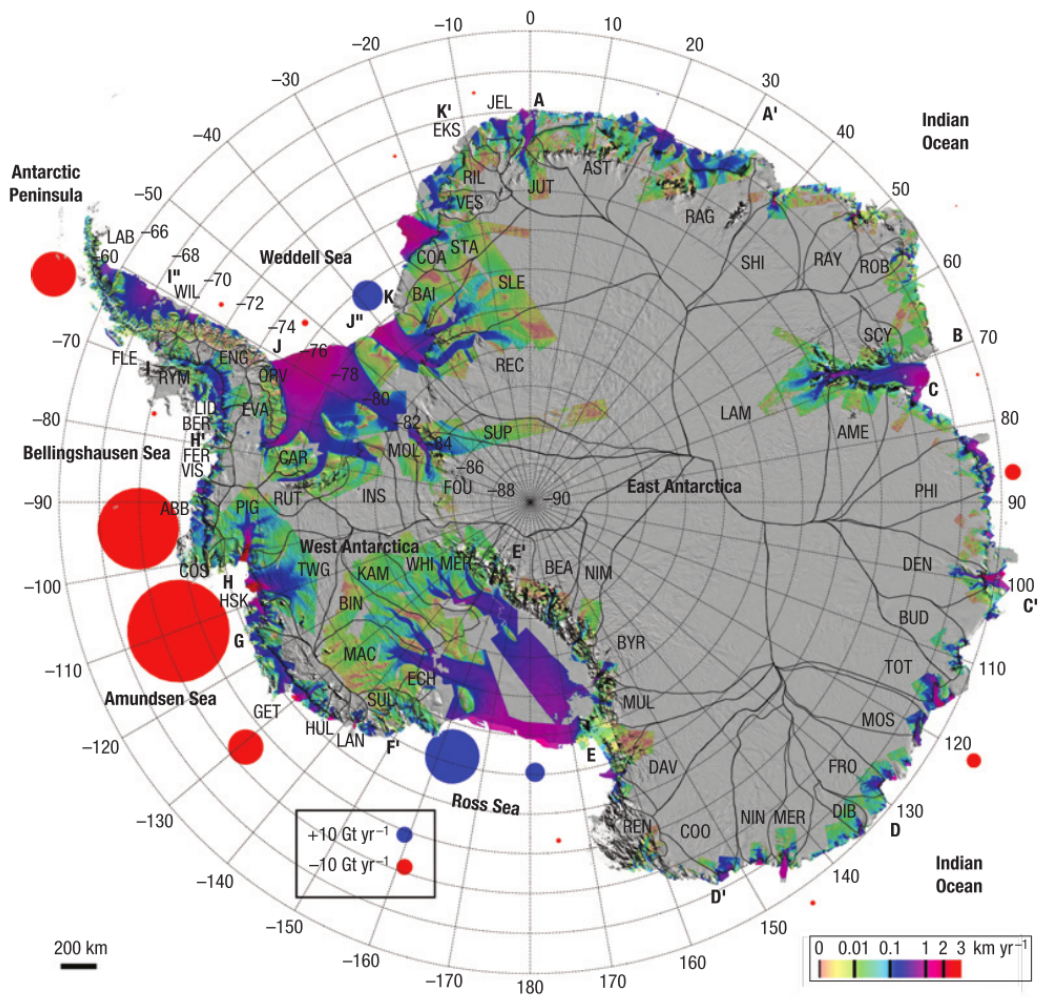
Figure 1.1: Mass balance of the Antarctic ice sheet. The map shows ice velocity color coded on a logarithmic scale overlaid on a MODIS mosaic (*Scambos et al.*, 2007). The circles show the mass loss (red) and gain (blue) in Gt/yr of the major basins. Black lines denote the drainage basins. This figure is from *Rignot et al.* (2008).

Study	Period	Method	EAIS	WAIS	AIS
Wingham et al. (1998)	1992-1996	altimetry	-1±53	-59±50	-60±76
Rignot and Thomas (2002)	1995-2000	mass budget	20±21	-44±13	-24±34
Davis et al. (2005)	1992-2003	altimetry	45±7		
Zwally et al. (2005)	1992-2001	altimetry	16±11	-47±4	-31±12
Velicogna and Wahr (2006)	2002-2005	GRACE	0±51	-136±19	-139±73
Ramillien et al. (2006)	2002-2005	GRACE	67±28	-107±23	-129±15
	1996			-83±59	-112±91
Rignot et al. (2008)	2000	mass budget	-4±61	-106±60	-138±92
	2006			-132±60	-196±92
Chen et al. (2009)	2002-2009	GRACE	-57±52	-132±26	-190±77
McMillan et al. (2014)	2005-2010	altimetry	-3±36	-137±27	-159±48
Zwally et al. (2015)	2003-2008	altimetry	136±28	-25±15	82±25
	1992-2001		136±50	-16±20	112±61

Table 1.1: Mass balance in Gt/yr of the East Antarctic Ice Sheet (EAIS), West Antarctic Ice Sheet (WAIS) and Antarctic Ice Sheet (AIS) as estimated by previously published studies using different methods. 360 Gt of mass loss is equivalent to 1 mm of global sea level rise.

flow dominates the mass loss in this sector (*Mouginot et al.*, 2014b), widespread grounding line retreat and flow speed-up (*Mouginot et al.*, 2014b; *Rignot et al.*, 2014) leads to an acceleration of 16.3±5.6 Gt/yr^2 in mass loss from 2003 to 2009 (*Sutterley et al.*, 2014). Dynamic loss in Amundsen Sea Embayment is triggered by enhanced basal melting of ice shelves due to warm water intrusion (*Pritchard et al.*, 2012; *Jacobs et al.*, 2011; *Shepherd et al.*, 2004). The bed topography in this sector is mostly retrograde, where the bed deepens from the coast to the interior. The retrograde bedrock elevation provides favorable conditions for the retreat to proceed (*Rignot et al.*, 2014), through a dynamic mechnism called the marine ice sheet instability.

1.3 Marine ice sheet instability

The bed topography in large parts of Antarctica becomes deeper from the peripheral towards the interior of the ice sheet due to the effect of isostatic depression. *Weertman* (1974) proposed that this retrograde bed configuration makes the ice sheet on top inherently unstable

(Figure 1.2a), such that small perturbations can cause large-scale, irreversible retreat. This theory, so-called marine ice-sheet instability, has been complemented and refined by many successive theoretical and modeling studies (e.g. *Thomas* (1979); *Schoof* (2007a,b)). The mechanism of marine ice sheet instability provides theoretical grounds for rapid disintegration of the Antarctic ice sheets, though no paleo records has been found to date to prove that the abrupt change of sea level in Earth's history is directly linked to a marine ice sheet instability.

The left panel of Figure 1.2 shows the schematic of the marine ice sheet instability mechanism, where the glacier bed deepens inland. If the glacier experiences a small perturbation and the grounding line advances to Profile A, the ice thickness at the grounding line will be smaller than in the initial state I. Theory suggests that the rate of creeping thinning due to advection is roughly proportionate to the 4th power of the ice thickness (*Weertman*, 1957). The reduced creeping thinning will result in further advance of the glacier. Similarly, if the grounding line retreats, an increase in ice thickness will speed up the creep thinning and accelerate the retreat. This process forms a positive feedback, indicating no stable grounding line positions on retrograde bed. Conversely, if the bed slopes upward towards inland as shown in the right panel, at an advanced position of the grounding line one will find a thicker ice column, which leads to a faster creeping thinning and prevents further advance of the grounding line. In this case the feedback is negative and the grounding line is stable. The instability is also reflected in the continental ice sheet mass budget: Grounding line retreat will increase the ice thickness at the grounding line, therefore result in a larger outflow. At the same time, grounding line retreat will shrink the domain of grounded ice, leading to a reduction in snowfall accumulation. The overall imbalance will ultimately thin the ice and the retreat will propagate.

Another aspect of the marine ice sheet instability is the fundamental non-linear relationship between the ice flux and the grounding line thickness (*Schoof*, 2007a). When a glacier
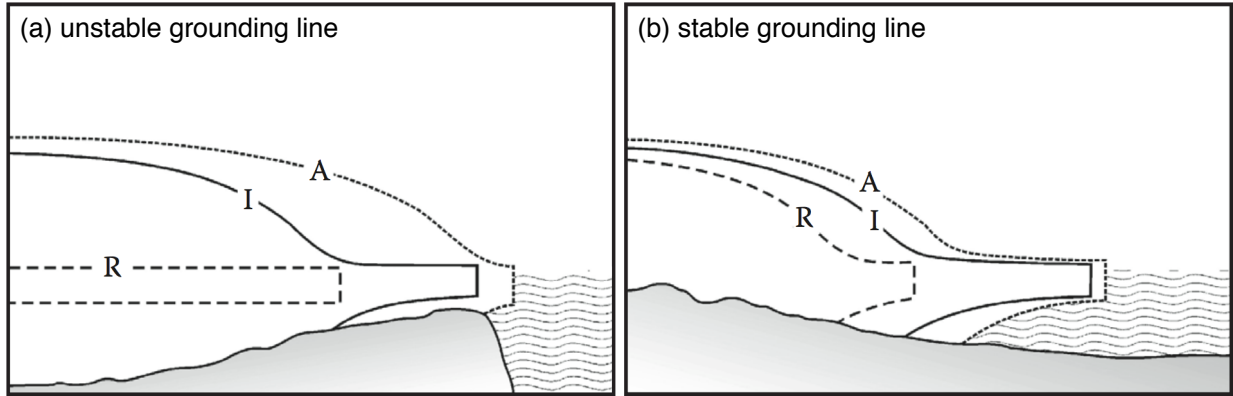
Figure 1.2: Schematic of bed topography configuration for (a) marine ice sheet instability; (b) stable grounding line postions. Ice sheet profiles labeled I denotes the initial geometry, profiles labeled A and R represent the geometry after advance and retreat, respectively. This figure is adapted from *van der Veen* (2013), which is a reprint of *Thomas* (1979).

retreats on a retrograde bed, the ice flux increases about five times faster than the ice thickness does, which makes it difficult to stabilize. This relation is developed on one-dimensional ice flow. The instability could be suppressed by possible stabilizing effects such as ice shelf buttressing, lateral drag from the sidewalls of the ice shelf, sedimentation and bed roughness (*Dupont and Alley*, 2005; *Gudmundsson et al.*, 2012; *Alley et al.*, 2007). Numerical modeling is needed to quantify these effects against the positive feedback in marine ice sheet instability. No studies to date, however, has provided theoretical basis to dismiss the marine ice sheet instability. It is likely that targeted modeling analysis is needed for each specific marine ice sheet configuration to examine its stability.

The recent revolution in satellite remote sensing provides wide coverage of observations on important parameters of ice dynamics. However, the short observational record does not provide sufficient evidence on ice sheet evolution to make definite conclusions about marine ice sheet instability. The collapse of the Larsen B Ice Shelf may provide some insights in this issue. In 2002, a large part of the Larsen B Ice Shelf disintegrated in two months (Figure 1.3) due to increased melt water ponding after a strong regional warming event (*MacAyeal et al.*, 2003). Significant thinning and speed-up has been observed on the glaciers feeding the
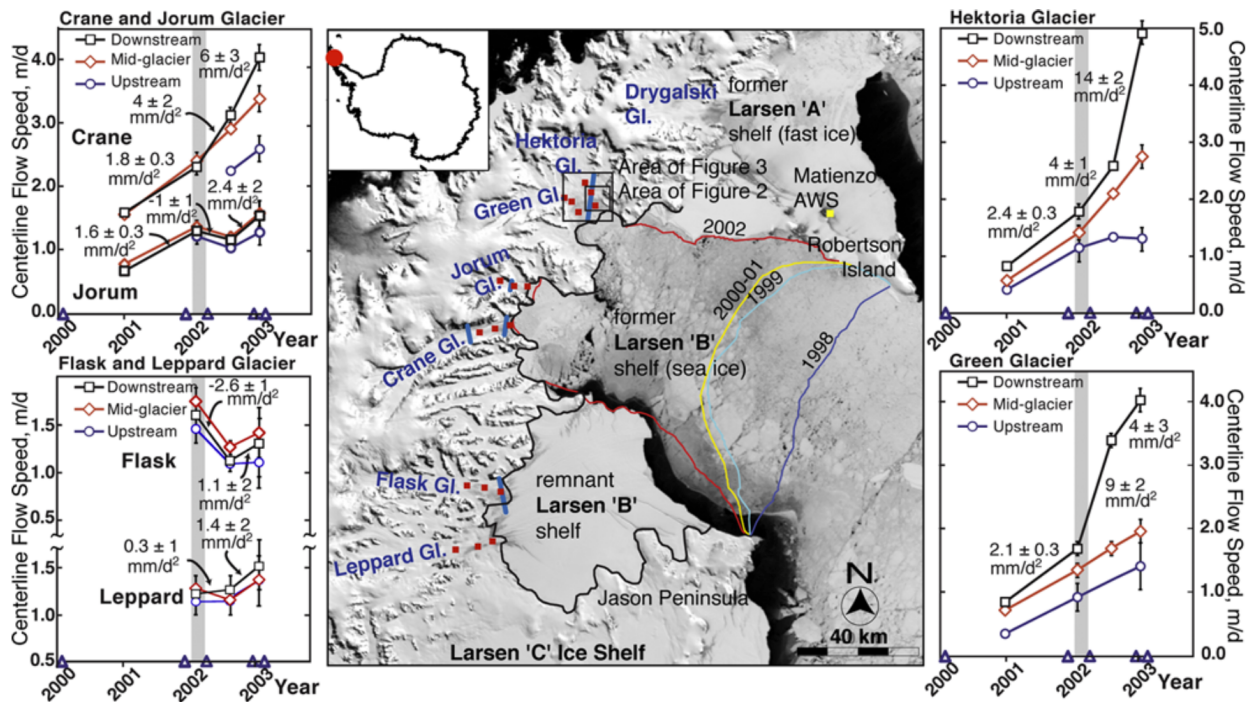
Figure 1.3: Flow acceleration after the collapse of Larsen B Ice Shelf by *Scambos et al.* (2004). Center panel is MODIS image from Nov 1st, 2003 of the Larsen B Ice Shelf with April ice shelf extents and the grounding line (black (*Rack and Rott*, 2004)) between 1998 and 2002. Red boxes are speed measurement site along lower glacier centerlines. Surrounding graphes are centerline ice speeds and downstream site accelerations for six glaciers. Grey bars represent the Feb-Mar 2002 shelf collapse event.

disintegrated part of the ice shelf following the ice shelf failure while little change on other adjacent glaciers has been detected (*Rignot et al.*, 2004; *Scambos et al.*, 2004; *Rott et al.*, 2011). The theory of marine ice sheet instability offers a reasonable explanation for the observed dynamic response: The ice shelf failure leads to a loss of buttressing at the grounding line, which triggers longitudinal stretching, flow acceleration and ice thinning (*Cuffey and Paterson*, 2010). The observational evidence confirms the mechanical link between the ice shelf and grounded ice, but modeling analysis is still needed to explicitly understand the feedback.

1.4 Remote sensing of polar ice sheets

During the 1950s, study of Antarctic ice sheet was illuminated by *in situ* measurements. While precise, these measurements are limited spatially and temporally. The advent of satellite remote sensing fully expanded observations on the characteristics, behavior and evolution of the ice sheets. Grounding breaking discoveries have emerged in this rapidly developing research field since then.

1.4.1 Applications of optical remote sensing

The first generation of the Landsat program, the Earth Resource Technology Satellite, was launched on July 23, 1972. The Landsat program has now become the world's longest running Earth-observing satellite program. The most recent generation, Landsat 8, was launched on Feburary 11, 2013. Landsat provides a 40-year long record of the evolution of polar ice sheets. It is widely used in monitoring ice front positions (*Bindschadler*, 2002) and surface features of the glaciers such as supraglacial lakes and longitudinal structures (*Glasser and Scambos*, 2008; *Pope et al.*, 2015). Ice surface velocity can also be obtained by tracking small scale

surface features such as rifts and crevasses on repeat-pass Landsat imagery (*Scambos et al.*, 1992). This technique will be explained in detail in Chapter 3. Satellite images from other optical sensors have similar applications. These satellites include the widely used Moderate-Resolution Imaging Spectroradiometer (MODIS) and the Advanced Spaceborne Thermal Emission and Reflection Radiometer (ASTER). Some high-resolution optical sensors (e.g. ASTER, SPOT, WorldView, GeoEye) produce stereo images that can be used to generate surface elevation maps (*Cook et al.*, 2012). Optical remote sensing relies on solar illumination, which is available only in summer time over most of the Antarctic ice sheet. In addition, the coastal regions of Antarctica are often covered by clouds, which blocks most of the information from the surface. This major weakness limits the application of optical remote sensing data in ice sheet studies.

1.4.2   Synthetic-aperture radar related techniques

The synthetic-aperture radar (SAR) sensors have great advantages compared to optical sensors because they actively illuminate the ground. SAR sensors emit successive pulses to illuminate ice surface, these pulses are radio waves that can see through the clouds. Therefore, SAR platforms have the capability to survey the Earth's surface day and night in all weather conditions. Fine spatial resolution from submeter to a few tens of meters can be achieved by the synthetic aperture technique. SAR images record both amplitude and phase information of the reflected signal. Most of the applications of optical satellite imagery can be accomplished using SAR amplitude images. Regarding the measurement of ice motion, the speckle tracking algorithm (*Michel and Rignot*, 1999) is much more robust compared to conventional feature tracking which is limited to coastal regions with surface features. This technique will be discussed further in Chapter 3.

A completely different technique, SAR interferometry (InSAR), makes use of the phase infor-

mation in SAR images. InSAR measures the differences in phase between two or more SAR images acquired from slightly different positions. It has been widely used to measure three key parameters of ice sheets: surface elevation (*Madsen et al.*, 1993), ice velocity (*Goldstein et al.*, 1993) and grounding line positions (*Rignot*, 1996). The precision of InSAR measurements is unprecedented. The phase differencing is sensitive to millimeter/centimeter scale displacement and meter scale surface elevation. By detecting vertical motion of ice shelves associated with tides, differential InSAR technique can accurately locate the grounding line, which used to be difficult. Repetitive InSAR coverage enables monitoring of ice sheet evolution, leading to significant advances in ice sheet research. In Chapter 2, 3 and 4, these applications will be reviewed and case studies on Totten Glacier will be presented.

1.4.3   Radar and laser altimetry

Satellite altimeters measure surface elevation of ice sheets and the temporal variability in elevation. Radar altimeters transmit pulses of electromagnetic radiation down to the ground and receive the reflected energy, then derive the distance between the satellite and the ground from the time difference. The first generation of satellite radar altimeters, the Seasat and Geosat missions, was launched in the 1970s. Despite the fact that these missions were designed to measure parameters of open ocean, they provided useful elevation measurements over Antarctica. The accuracy, resolution and coverage of the data were then improved largely in the subsequent European Remote Sensing satellite (ERS) and Environmental Satellite (Envisat) missions. In 2003, the first spaceborne laser altimeter, the Geoscience Laser Altimeter System onboard Ice, Cloud and land Elevation Satellite (ICESat GLAS), was launched. Compared to radar altimeters, the short wave laser instrument has a substantially smaller nadir footprint and takes measurements at a much higher accuracy and along-track resolution.

The large spatial coverage of satellite altimetry since the ERS mission enables the construction of Digital Elevation Models (DEMs) of the entire Antarctic ice sheet (*Bamber and Bindschadler*, 1997; *DiMarzio et al.*, 2007). These continental-scale high-resolution surface elevation maps have revealed numerous surface characteristics and spatial patterns (*Legresy and Remy*, 1997). Time series analysis comparing altimetry data from repeat tracks reveals extensive dynamic thinning along the coast of Antarctic ice sheet (*Pritchard et al.*, 2009; *Flament and Rémy*, 2012; *McMillan et al.*, 2014), indicating significant mass loss. In Chapter 2, observed change in surface elevation on Totten Glacier will be reviewed.

After 7 years of operation, ICESat retired in 2010. A follow-on mission, ICESat 2, is scheduled for launch in 2016. An airborne campaign, Operation IceBridge (OIB), helps bridging the gap between the two campaigns. In addition to altimetry measurements, the OIB aircraft also carries a suite of scientific instruments including radar sounder, gravimeter and magnetometer. The radar sounder measures the ice thickness and images the internal layers of the ice sheet. The gravimeter measures the gravitational field underneath the aircraft, which is used to infer the bathymetry under ice shelves. The magnetometer provides information on the geological properties of the bedrock. Totten Glacier has been extensively surveyed by OIB. These airborne data will be analyzed in Chapter 2.

1.4.4 Satellite gravity

The Gravity Recovery and Climate Experiment (GRACE) mission was launched in 2003. GRACE maps the global gravity field for the first time in the remote sensing history, once every month. The GRACE system consists of a pair of twin spacecrafts. The twin spacecrafts fly one behind the other at the same orbit. When passing over a mass at the Earth's surface (e.g. mountains), the leading spacecraft will experience a slight acceleration due to the strong gravity field, and the distance between the twin satellites therefore increases. Similarly, this

distance will decrease once the leading satellite flies past and the trailing one passes by. The acceleration of the twin spacecrafts and the distance between them is recorded with high accuracy. The gravity field of the Earth's surface is reconstructed from this information. The detailed geoid model from GRACE helps improve other measurements like satellite altimetry. Most importantly, direct measurements of the mass change of the ice sheets on both continental and regional scale largely improve global sea level rise estimates, as well as interpretations of spatial patterns of ice sheet mass balance.

1.5 Totten Glacier

In 1839, a portion of the Antarctic continent "to the west of the Balleny Island" was first sighted by the United States Exploring Expedition commanded by Lieutenant Charles Wilkes (1798-1877). In recognition of this discovery, this part of Antarctica was later named Wilkes Land. The mysterious land remained unexplored until late 1940s, by the time Totten Glacier was delineated from aerial photographs taken by USN Operation Highjump. Located at 114°E, 67.5°S along Wilkes Land (Figure 1.4), Totten Glacier is named after a cartographer George M. Totten, who served as a midshipman on the flag ship USS Vincennes of the United States Exploring Expedition. Mr. George M. Totten also assisted Lt. Charles Wilkes to correct the survey data from the expedition.

Totten Glacier is a major outlet glacier in East Antarctica. It has the largest ice discharge (71±3 Gt/yr) in East Antarctica (*Rignot et al.*, 2013). Its 537,900 km^2 large drainage basin, vastly below sea level, holds an ice volume equivalent to 3.9 m global sea level rise. The bed topography underneath the ice shelf of Totten Glacier may hold pathways for warm water intrusion. At 2,300 m below sea level where the glacier is grounded at its grounding line, the glacier experiences high ice shelf melting rates in comparison with other glaciers in East Antarctica (*Rignot et al.*, 2013). Comparison between the outflow and snowfall accumulation
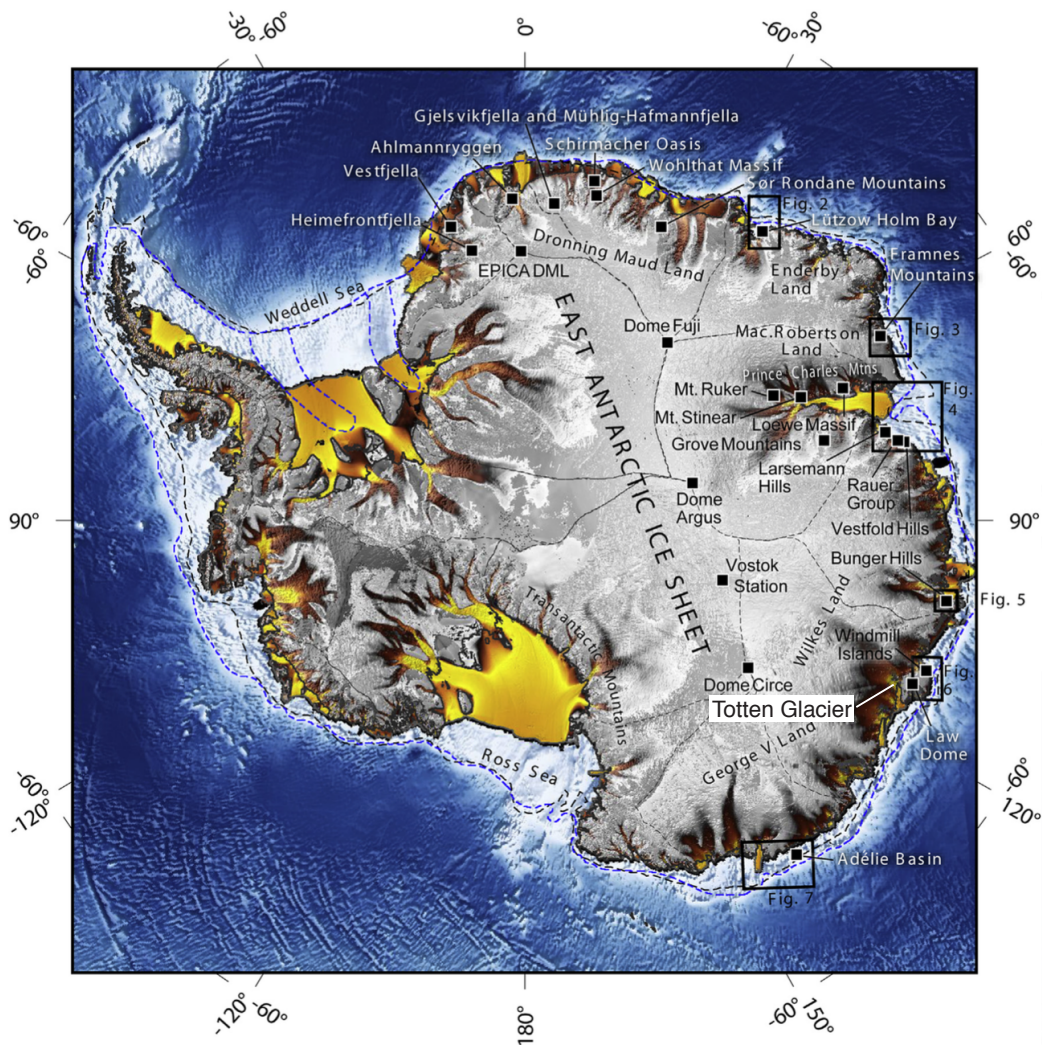
Figure 1.4: Map of Antarctica showing Locations of Wilkes Land and Totten Glacier. The ice sheet is colored in grey scale with fast flowing regions shaded dark. The open ocean is blue and continental shelf is in white hues. Yellow colors denote the floating ice shelves with estimated Last Glacial Maximum grounding line in black (*Anderson et al.*, 2002) and blue (*Livingstone et al.*, 2012). This figure is from *Mackintosh et al.* (2014).

Figure 1.5: A photo of the ice front of Totten Glacier. Credit: Esmee van Wijk/CSIRO. This photo is from a web news (*Australian Broadcasting Corporation*, 2015).

in its drainage basin shows a negative mass balance (*Rignot*, 2002; *Rignot et al.*, 2008), the mass loss is confirmed by independent estimates based on altimetry and GRACE data (*Shepherd and Wingham*, 2007; *McMillan et al.*, 2014; *Chen et al.*, 2009; *Velicogna et al.*, 2014).

Similar to the glaciers in Amundsen Sea Embayment, Totten Glacier has experienced dynamic changes. Mutiple altimetry studies (*Shepherd and Wingham*, 2007; *Zwally et al.*, 2005; *Pritchard et al.*, 2009, 2012; *Flament and Rémy*, 2012; *Horwath et al.*, 2012; *McMillan et al.*, 2014) have shown thinning patterns correlated with the fast flow, which implies a dynamic origin. During 2003 to 2012, gravity measurements from GRACE showed an accelerating mass loss on Totten Glacier and adjacent glaciers. On Wilkes Land including Totten Glacier, Moscow University Ice Shelf and Frost Glacier, the temporal variability of the mass loss of is consistent with time series of surface mass balance (SMB) anomalies (*Williams et al.*, 2014; *Velicogna et al.*, 2014) from the Regional Atmosphere Climate Model (RACMO2) (*Lenaerts et al.*, 2012). However, only 40% of the detected acceleration in mass loss could be explained

by SMB (*Velicogna et al.*, 2014), indicating a significant contribution from ice dynamics.

While most outlet glaciers in West Antarctica have been well documented, the evolution of Totten Glacier remained poorly characterized because major challenges are encountered when exploring this glacier using both *in situ* and remote sensing approaches. The glacier surface is constantly altered by strong surface weathering processes, and experiences high shear when flowing at a high speed along the stagnant Law Dome. These effects make it difficult to correlate radar images acquired at different times, resulting in significant gaps in the International Polar Year Antarctic ice velocity map (*Rignot et al.*, 2011a). The technical challenges are described in detail in Chapter 3. Due to these difficulties, no velocity change or grounding line migration have been reported so far.

A detailed numerical modeling will be necessary to evaluate the sensitivity of Totten Glacier in response to climate change. Such exercises require a detailed records of ice velocity, ice thickness, and the grounding line position of the glacier to help constrain and validate the model. This study aims at compiling a comprehensive dataset of Totten Glacier.

To confirm that the observed mass loss of Totten Glacier is caused by ice dynamics, the elevation change of the glacier is examined and compared with the flow pattern. The thinning pattern is well correlated with the ice flow spatially. An ice velocity record derived from satellite data shows acceleration/deceleration periods, consistent with the observed thinning rates. InSAR-derived grounding line mappings reveal a grounding line retreat along flow associated with the flow acceleration and ice thinning. The glacier is discharging more ice than it gains from snow accumulation in the past 26 years. Hydrostatic analysis of the grounding zone of Totten Glacier provides insights about the future evolution of the glacier.

Chapter 2

Topography and elevation change of Totten Glacier

The mass balance of an ice sheet is the difference between its mass gain and loss. Ice sheets gain mass through snow fall accumulation and lose mass through ablation, melting, or calving processes. The main processes controlling ice sheet mass balance is surface mass balance and ice motion. Change in snowfall accumulation and surface melting, acceleration/deceleration in ice flow and retreat/advance of grounding lines can all cause changes in ice surface elevation. Therefore, observation and interpretation of elevation changes are of great importance. The ice sheet topography itself also provides a number of benefits. For instance, continental-scale surface topography maps of ice sheets could be used to identify drainage basins (*Bamber et al.*, 2000a,b) based on the fact that ice is flowing under gravity. Basal topography has significant control on the grounding line stability of ice sheets (*Sun et al.*, 2014).

In this chapter, I present high resolution surface topography maps of Totten Glacier derived from satellite synthetic aperture radar interferometry (InSAR) data in 2011 and 2013. The

two digital elevation models (DEMs) acquired two years apart are differenced to measure changes in surface elevation. The surface elevation is combined with a basal topography derived from a mass conservation approach to calculate the hydrostatic potential of the glacier. This calculation is repeated on flight tracks of Operation IceBridge (OIB) where high resolution airborne data are available.

2.1 Surface topography

2.1.1 Mapping ice sheet surface topography with InSAR
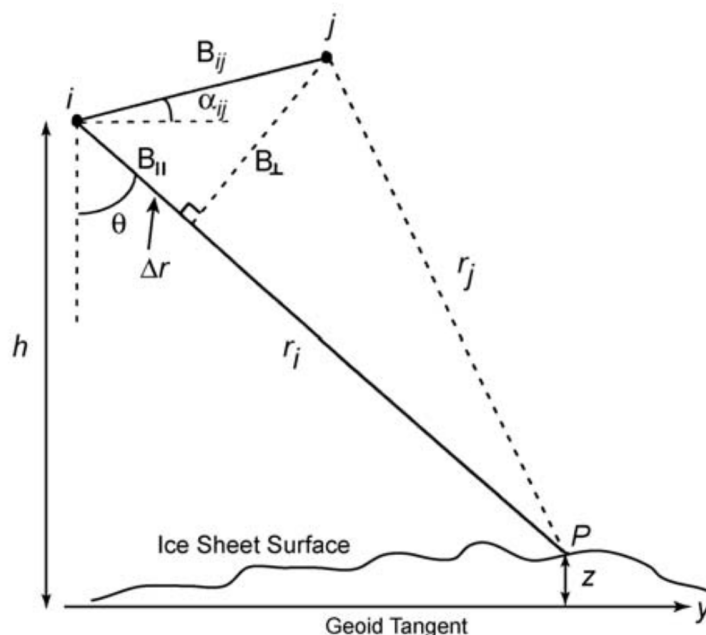
Figure 2.1: Geometry configuration of satellite SAR interferometry (*Massom and Lubin*, 2006). i and j are positions from where the SAR image pairs of surface location P are acquired. B_{ij} is the spatial baseline with the angle α, consisting a parallel component $B_{\parallel}$ and a perpendicular component $B_{\perp}$. θ is the incidence angle, the range of the two SAR observations are denoted as r_i and r_j, yielding a differential range Δr. This figure is from *Massom and Lubin* (2006) and adapted from *McLeod et al.* (1998) and *Joughin et al.* (1996).

Figure 2.1 is a schematic of InSAR geometry. Two SAR sensors i and j fly on parallel orbits and illuminate the ice sheet surface from slight different angles. The separation between

20

the sensors, B_{ij}, is the interferometric baseline, which breaks down to a parallel component $B_{\parallel}$ and a perpendicular component $B_{\perp}$ with respect to the look direction. r_i and r_j are slant ranges, which are vectors denoting the line-of-sight distances from the sensors to the ground. The elevation of surface point P can be derived from the slant range difference Δr and accurate orbit information based on gemetry. A major advantage of InSAR in mapping the topography is its accuracy. As a coherent system, the SAR sensors record not only the amplitude, but also the phase of the received signal. With the information from the phase, Δr can be determined to sub-wavelength precision. In comparison, the precision of conventional stereo-derived DEMs from optical imagery is usually limited by spatial resolution (*Rosen et al.*, 2000).

The SAR images pairs are coregistered and combined to form an interferogram. The phase of the interferogram at each point is given by (*Rosen et al.*, 2010):

$$\Delta\phi_{ij} = \frac{4\pi}{\lambda}\frac{B_{\perp}}{r_i\sin\theta}z + \frac{4\pi}{\lambda}\delta r_g + \frac{4\pi}{\lambda}\delta r_{atm} + \frac{4\pi}{\lambda}\delta r_{ion} \tag{2.1}$$

where λ is the radar wavelength, θ is the incidence angle, z is the elevation of the surface, δr_g is the projection of the ice motion in between the observations i and j onto r_i. The last two terms represent the phase delay introduced by the neutral atmosphere and the ionosphere, respectively.

InSAR systems can be either single-pass or repeat-pass. In single-pass systems, two sensors simultaneously acquire SAR images of the same area on the surface. In this case, the atmospheric and ionospheric delay can be considered equal for both observations, and Equation 2.1 is simplifed as:

$$\frac{\partial\Delta\phi_{ij}}{\partial z} = \frac{4\pi}{\lambda}\frac{B_{\perp}}{r_i\sin\theta} \tag{2.2}$$

Then, according to the geometry, the incidence angle θ can be determined as:

$$\sin(\alpha_{ij} - \theta) = \frac{(r_i + \Delta r)^2 - r_i^2 - B_{ij}^2}{2r_i B_{ij}^2} \tag{2.3}$$

where α_{ij} is the angle of B_{ij} to the horizontal. With information on the nadir distance h to the ellipsoid, the elevation above the same ellipsoid can then be derived by:

$$z = h - r \cos \theta \tag{2.4}$$
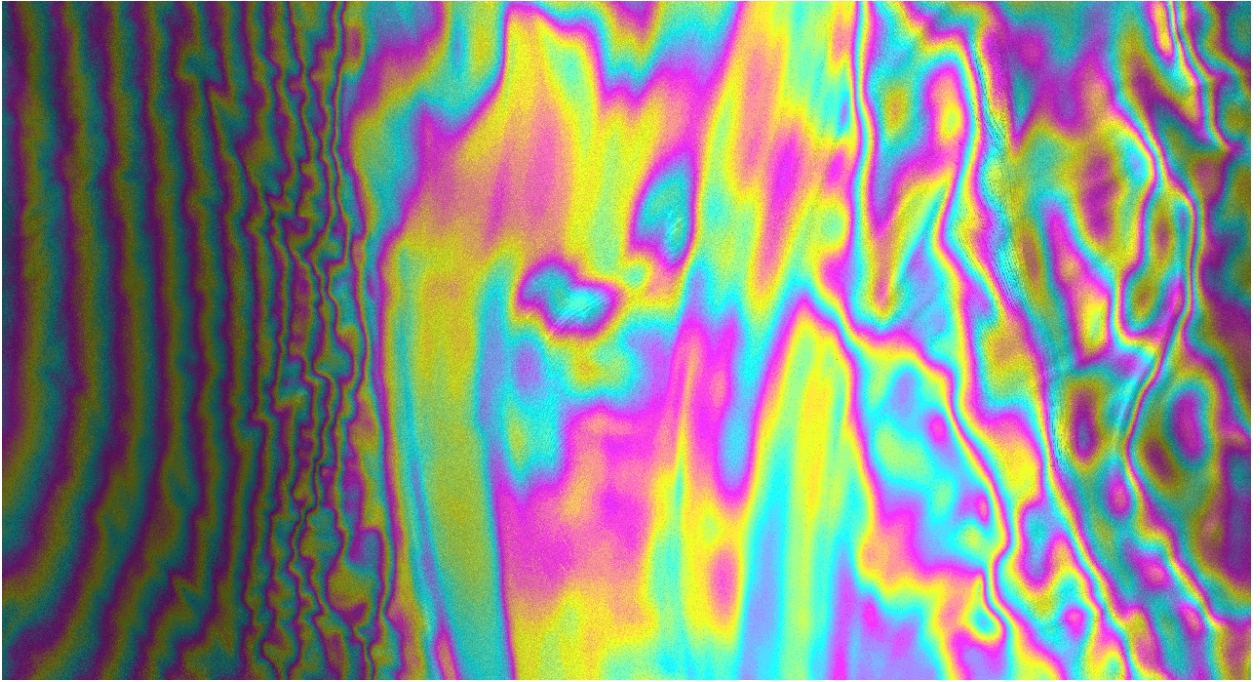
Figure 2.2: Interferogram of Totten Glacier derived from InSAR data from TanDEM-X mission. Each fringe color coded from blue to yellow, purple and blue again is a full cycle in interferometric phase or 360 degrees.

In an single-pass interferogram (e.g. Figure 2.2), the isophase lines termed interferometric fringes represent contours of surface elevation. Each color cycle in Figure 2.2 represent a phase shift of 2π. The corresponding shift of altitude to this phase shift is called the altitude

of ambiguity h_a (*Massonnet and Feigl*, 1998):

$$h_a = \frac{\lambda}{2} \frac{r_i \sin \theta}{B_\perp} \tag{2.5}$$

The altitude of ambiguity is a useful measure of the InSAR pair's sensitivity to topography.
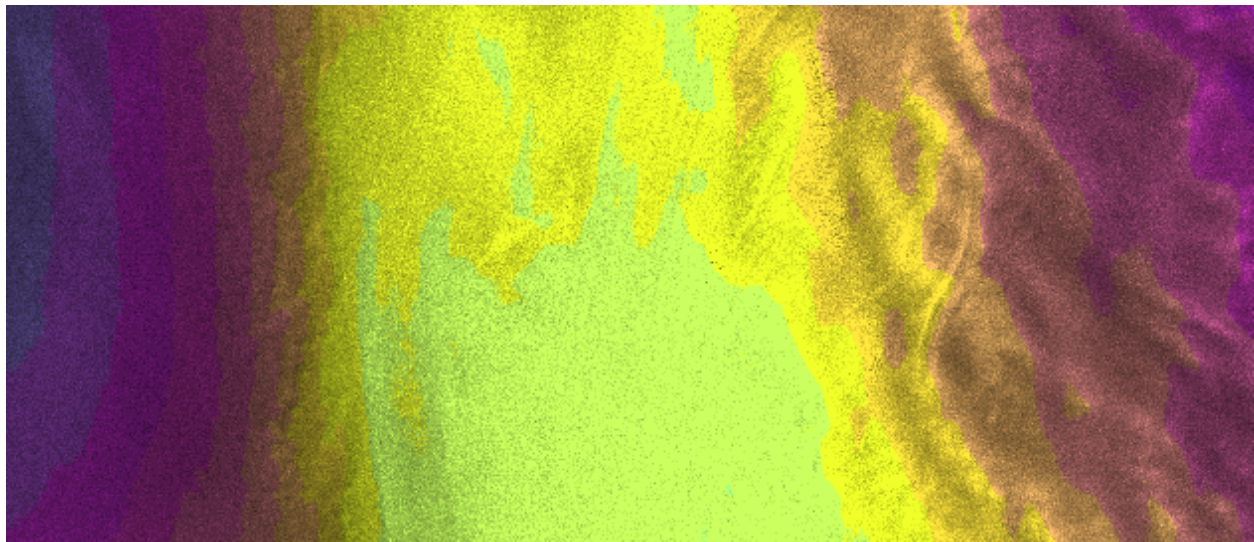
Figure 2.3: Unwrapped interferogram of Totten Glacier derived from InSAR data from TanDEM-X mission.

As shown in Figure 2.2, interferograms only record the principle phase, modulo 2π. In order to obtain a continuous phase map, the two-dimensional map of principle phase must be unwrapped. Figure 2.3 shows an example of unwrapped phase. An absolute phase constant is then determined to derive the true values of $\Delta\phi$.

The situation for repeat-pass systems is more complex. Usually, the phase delay caused by atmosphere is small in polar regions due to the low humidity. The ionosphere noise is strong in regions close to magnetic poles, like Totten Glacier. The ionosphere noise is dispersive, strongly dependent on the frequency of the radar signal. For C-band radars like ERS-1/2, ionospheric noise is minor. In general, Equation 2.2 to 2.4 hold for repeat pass interferometers over regular terrains without apparent ground motion. However, when applied to ice sheets, the ice motion term cannot be neglected. To separate the topographic

phase delay from the part caused by ice motion, at least three repeat InSAR observations are needed. Assuming steady ice motion, the topographic terms can be cancelled out by subtracting two interferograms, with the remaining phase being ice motion only (*Joughin et al.*, 1996).

2.1.2 Surface topography of Totten Glacier from TanDEM-X data

In this study, I use alternating bistatic TanDEM/TerraSAR-X data from the German TanDEM-X mission to derive the surface topography of Totten Glacier. In the alternating bistatic mode of TanDEM-X mission, a pair of twin SAR platforms, TanDEM-X and TerraSAR-X, fly in parallel orbits. One of the sensors transmits radar pulses whereas both sensors receive the reflected radar echoes (*Duque et al.*, 2015). The single-pass acquisition scheme is ideal for DEM mapping because it minimizes temporal decorrelation and atmospheric noise without contamination from ice motion. As an X-band radar with a wavelength of 3.125 cm, TanDEM-X can achieve a vertical accuracy of less than 2 m (*Moreira et al.*, 2008).

The TanDEM-X SAR data are processed from raw format to single look complex images, then TanDEM/TerrSAR-X image pairs are combined to form single-pass interferograms. This process is done using the GAMMA processor (www.gamma-rs.ch). An absolute phase constant is then calculated using the Levenberg-Marquardt algorithm (*Press et al.*, 1992). Airborne laser altimetry surface elevation measurements in 2009-2012 (*Blankenship et al.*, 2012, updated 2013) are used as ground control points in the calculation. The difference between the measured surface elevation and the inferred surface elevation is minimized. Multiple TanDEM-X tracks and orbits are employed to stack the results and reduce errors. The derived digital elevation model (DEM) with 20-m spacing is presented in Figure 2.4b, and consists of 2 ascending tracks and 2 descending tracks.

Comparing the results with Operation IceBridge (OIB) laser elevation data, the root mean
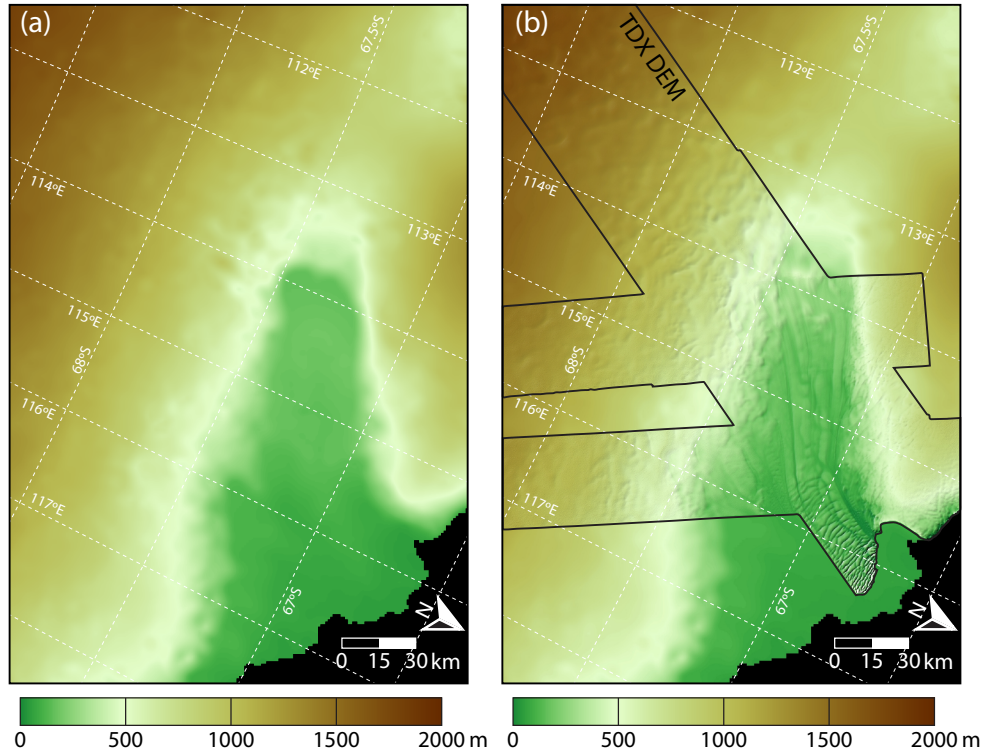
Figure 2.4: Surface elevation maps of Totten Glacier from (a) BEDMAP2 (*Fretwell et al.*, 2013); and (b) TanDEM-X data. Black polygon denotes the boundaries of TDX DEM mapping versus BEDMAP2.

square error of the DEM is estimated as 3 m (Figure 2.5). The residual error is caused by: (1) the uncertainty in OIB laser elevation (10-30 cm in *Young et al.* (2015)); (2) changes in surface elevation between 2009 and 2012 (1-2 m); (3) unknown spatial variations in penetration depth in snow of the radar signals vs laser altimetry; and (4) changes in oceanic tides on the ice shelf.

The high-resolution TanDEM-X DEM (Figure 2.4b) reveals detailed surface characteristics which cannot be seen on standard DEM products like BEDMAP2 (Figure 2.4a) (*Fretwell et al.*, 2013). Totten Glacier is flowing along the eastern flank of Law Dome, generating strong elevation gradient along the shear margins. On the eastern side of the glacier, the elevation drop is more gradual. Large scale undulations in the grounded part of the glacier reflect underlying bedrock structure. Over the ice shelf, longitudinal flow strips appear as 20-30 m deep slots which indicate the flow direction of the glacier. Surface crevasses start to

25
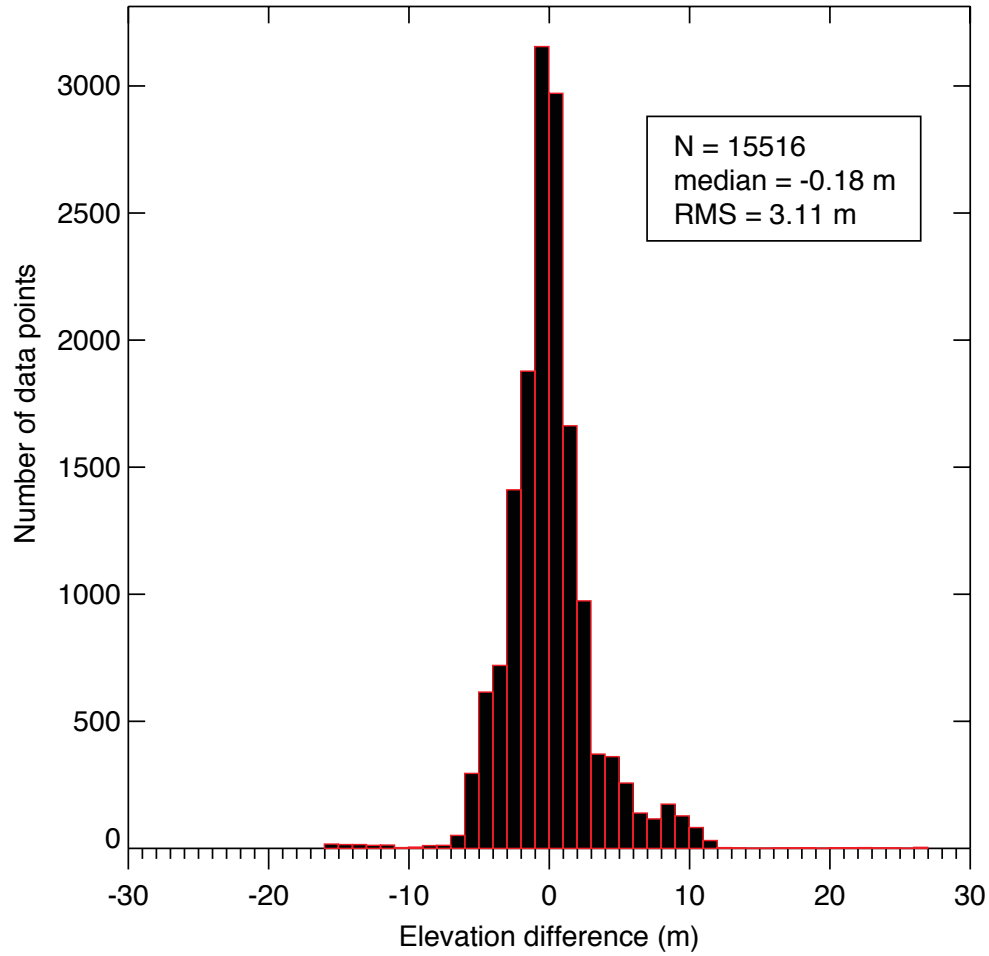
Figure 2.5: Histogram of elevation difference between OIB laser altimetry data (*Blankenship et al.*, 2012, updated 2013) and TanDEM-X DEM. For OIB laser data, only measurements over grounded ice are used.

appear 40 km upstream of the ice front. Near the grounding line (67.4° S, 114° E), there are several 50-m bumps in the surface elevation, which may play a role in the complex grounding line pattern (*Li et al.*, 2015a).
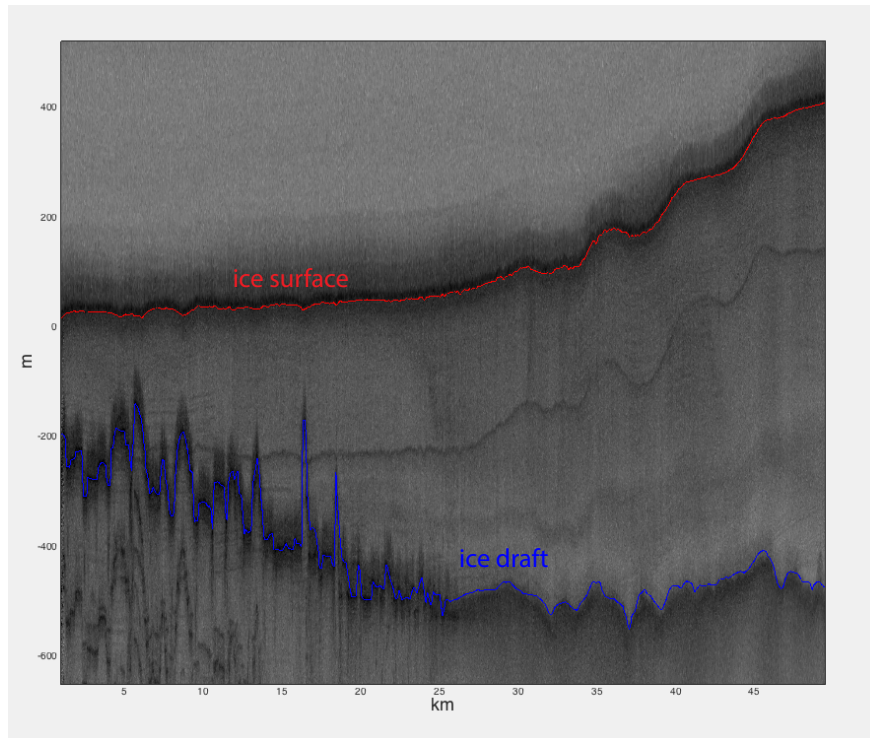
Figure 2.6: A sample radar sounding echgram for Petermann Glacier in Greenland (*Gogineni*, 2012).

2.2 Basal topography

2.2.1 Airborne radar soundings of ice thickness on Totten Glacier

Ice is relatively transparent to radar waves. Radar echoes can penetrate through glacial ice and image the internal structure of the ice sheets. The reflected radar signals are synthesized to echograms (Figure 2.6) from which the upper and lower surfaces of the ice mass can be identified. Since 1960s, the Antarctic ice sheet has been surveyed extensively by airborne radar soundings. In 2001, all available ice thickness measurements have been integrated to compile the first complete subglacial topography map of Antarctica, BEDMAP-1 (*Lythe et al.*, 2001). However, the historical data are sparse in Totten Glacier region (Figure 2.7).

Our knowledge of the basal properties in this sector has been greatly improved by the new
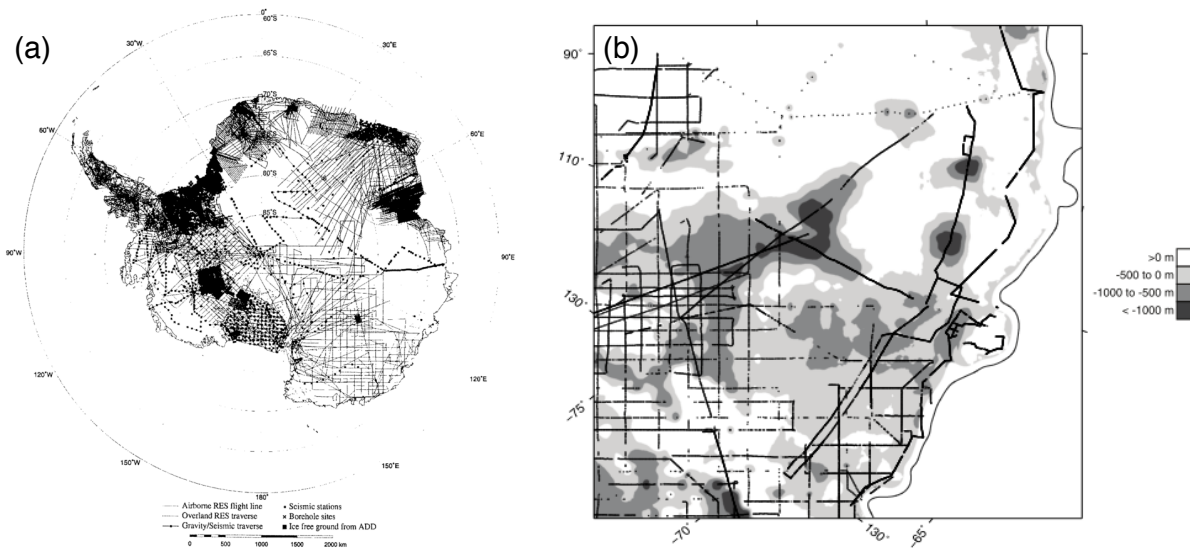
Figure 2.7: (a) Distribution of ice thickness data in the BEDMAP-1 database (*Lythe et al.*, 2001). (b) BEDMAP-1 Antarctic bed elevation with the location of prior datasets in black lines (*Roberts et al.*, 2011).

dataset from the Investigating the Cryospheric Evolution of the Central Antarctic Plate (ICECAP) program as part of the NASA OIB mission. Totten Glacier was extensively surveyed by the HiCARS 60-MHz ice penetrating radar onboard ICECAP aircraft (Figure 2.8a) (*Young et al.*, 2011). A new bed topography map established from this dataset (Figure 2.8b) unveils previously unknown features of the Aurora Subglacial Basin, through which Totten Glacier drains. The Vanderford Subglacial Trench around the flanks of Law Dome has been found to be much deeper than previously thought, with the deepest point 2,426±10 m below sea level. Further inland, the ICECAP data shows the presence of a deep depression oriented orthogonal to the present ice sheet margin, the Aurora Subglacial Basin. The Aurora Subglacial Basin is connected to the drainage basin of Denman Glacier to the west through a deeply dissected mountain region, while bounded by another dissected ridge to the east. These deep transverse channels across the ridges reflect distinct geomorphology which originated from past glacial activities (*Young et al.*, 2011).
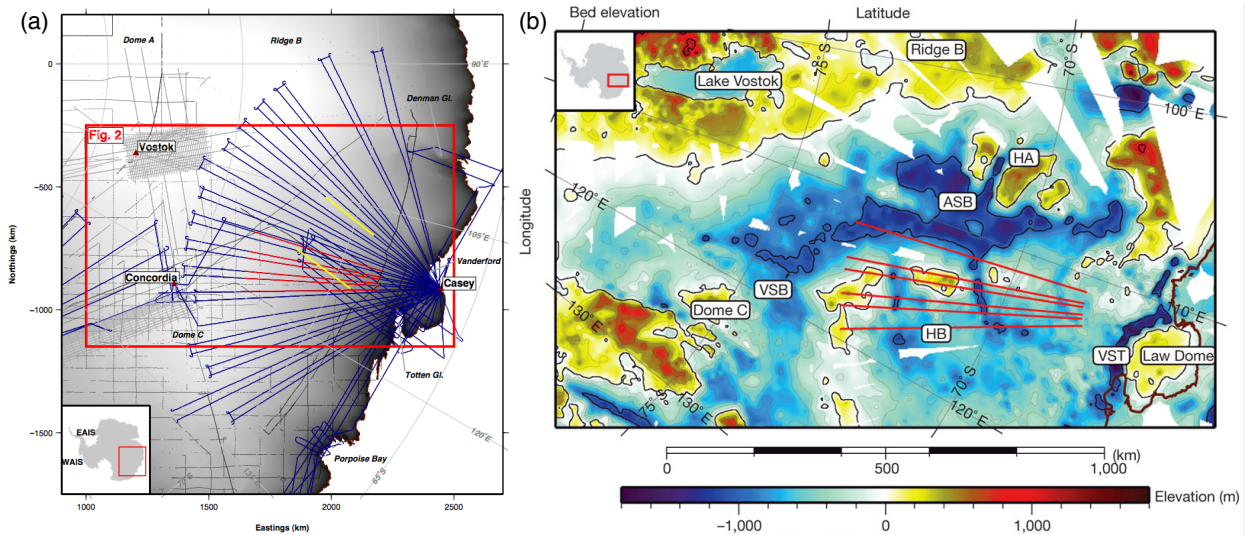
Figure 2.8: (a) Flight lines of the ICECAP project (blue) in the Aurora Subglacial Basin sector during December and January of 2008/9 and 2009/10, overlaid on a map of surface topography. Historical data in grey. The red box denotes the map outline for (b). (b) Bed topography derived from ICECAP radar-echo sounding data shown in (a) using a natural neighbor interpolation method. Both figures are from *Young et al.* (2011).

2.2.2 Basal topography mapping of Totten Glacier using a mass conservation method

The mass conservation (MC) approach

As discussed in the previous section, direct ice thickness measurements from airborne echo-sounding radars provide valuable information about glacier bed. However, a drawback of these measurements is that ice thickness is only measured along flight tracks spaced several to tens of km from each other. To establish a complete ice thickness map, radar data are usually interpolated/extrapolated using geostatistical methods like kriging (*Stein*, 1999), with a grid size much smaller than the track spacing (e.g. 1 km grid size for BEDMAP-2 (*Fretwell et al.*, 2013)). Ice thickness maps, together with independent velocity maps from satellite InSAR, are often used to initialize ice sheet models. When the interpolated ice thickness maps are combined with InSAR velocities, the artifacts from the interpolation results in large spatial

deviations in ice flux which leads to unrealistic ice dynamics and limits the performance of ice sheet models (*Seroussi et al.*, 2011).

Morlighem et al. (2011) proposed a mass conservation (MC) approach to derive spatially consistent ice thickness maps by combining sparse radar sounding ice thickness measurements with high-resolution ice velocity maps. The mass conservation equation of ice flow can be described as:

$$\frac{\partial H}{\partial t} + \nabla \cdot H\overline{\boldsymbol{v}} = \dot{M}_s - \dot{M}_b \tag{2.6}$$

where H is ice thickness, $\overline{\boldsymbol{v}}$ is the depth-averaged horizontal velocity, $\dot{M}_s$ is the surface mass balance in m/yr, and $\dot{M}_b$ is the basal melting rate in m/yr. Solving Equation 2.6, while at the same time minimizing the misfit between airborne radar data and the inferred ice thickness, an ice thickness map physically consistent with observed ice velocity can be derived.

MC topography of Totten Glacier

A new ice thickness map of Totten Glacier is developed using the MC approach combining the most complete velocity map (*Li et al.*, 2015b) with airborne radar sounding ice thickness data from ICECAP (*Blankenship et al.*, 2011, updated 2013). This thickness map is developed by M. Morlighem (UC Irvine) and published in **?**. The calculation includes surface mass balance from the Regional Atmospheric and Climate model (RACMO2) (*Lenaerts et al.*, 2012) and ice shelf melt rates from *Rignot et al.* (2013). The MC ice thickness map has a 600-m spacing and a vertical precision of 60 m (Figure 2.9). This map is a major improvement compared to earlier maps derived from the krigging of OIB ice thickness data at 5 km spacing (e.g. BEDMAP2 (*Fretwell et al.*, 2013)).
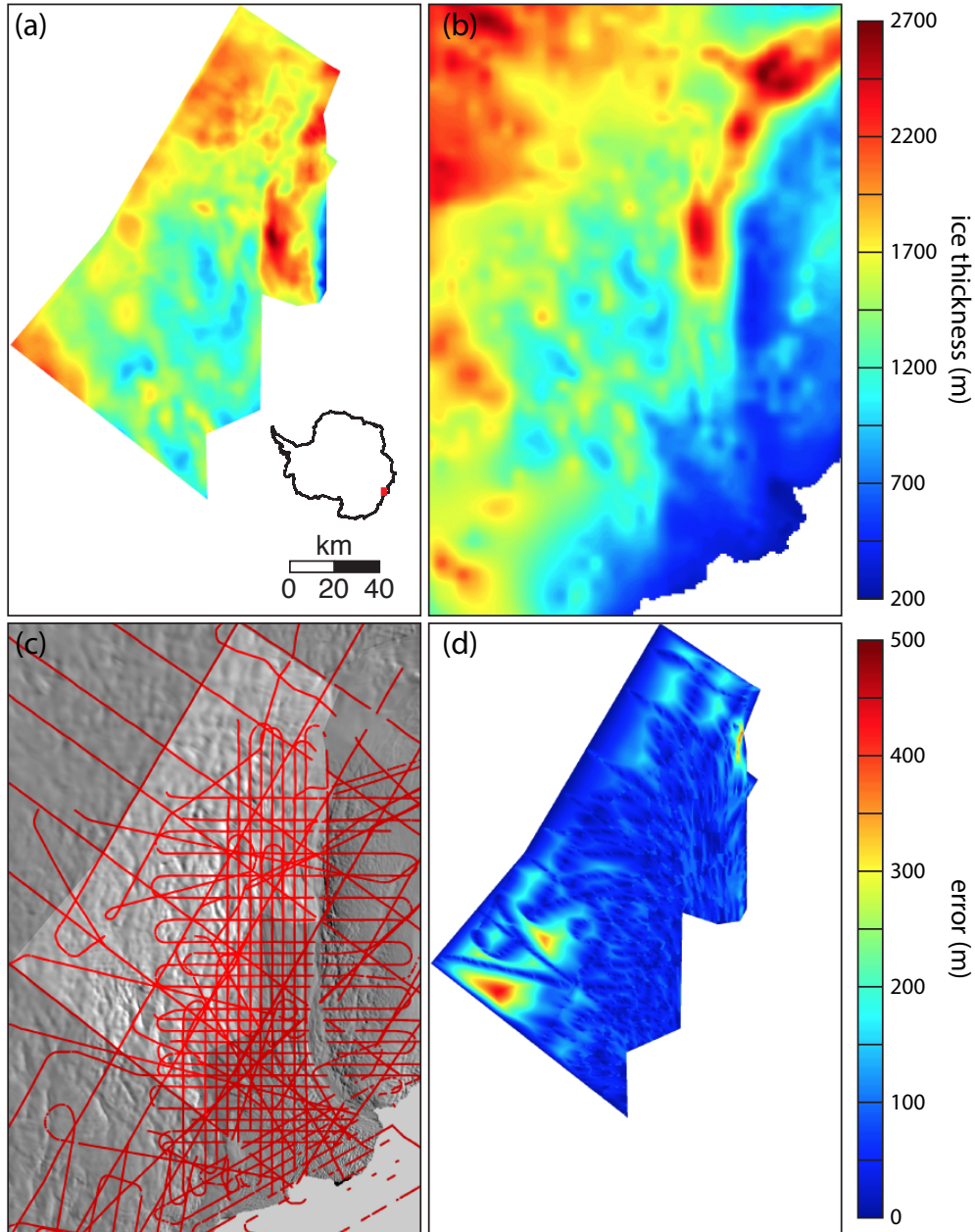
Figure 2.9: Ice thickness derived from mass conservation (MC) method (*Li et al.*, 2015a) (a) and BEDMAP2 (b) (*Fretwell et al.*, 2013). (c) shows the footprints of the ICECAP ice thickness tracks (*Blankenship et al.*, 2011, updated 2013) (in red) overlaid on the MOA map. Regions outside the MC domain are masked in half-transparent grey. (d) shows the error of the MC thickness map. The error ranges from a few meters (along the OIB tracks) to up to 500 m, where the distance between tracks grows to tens of kilometers. The error is about 65 m on average for the entire domain. Near the grounding line, the error decreases to ∼40 m due to the dense OIB ice thickness measurements. See *Morlighem et al.* (2011) for details of the MC mapping. This figure is from *Li et al.* (2015a).
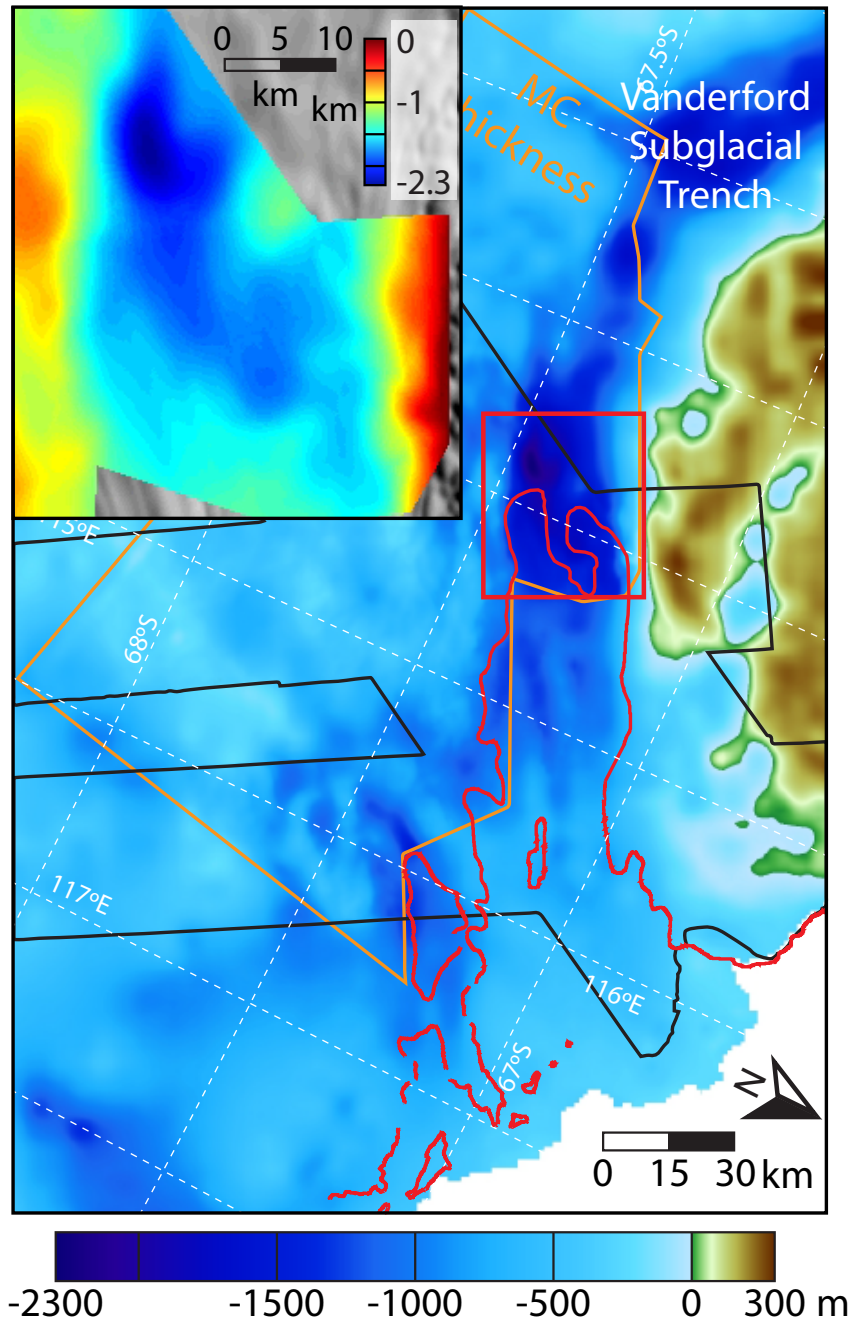
Figure 2.10: Ice draft topography of Totten Glacier. Black polygons denote the boundaries of TDX DEM mapping versus BEDMAP2 (*Fretwell et al.*, 2013). Orange polygons delineate the boundaries of the mass conservation (MC) domain. The redbox is zoomed in the inset on a different color scale. This figure is from *Li et al.* (2015a). The yellow lines are ICECAP flight tracks whose profile is plotted on the right panels. On the profile plots (a) (b) and (c), surface elevation is in blue, bed elevation is in green, and hydrostatic equilibrium ice bottom is in orange. Blue shade is floating ice based on the 2013 grounding line (*Li et al.*, 2015a), Ice floatation in 1996 is delineated by a red line. P and Q mark the intersections of AA' and BB' with CC', respectively. Grey boxes in (a) and (b) delineate the portion over which we calculate surface and bed slopes.

The MC-derived ice thickness is subtracted from the TanDEM-X DEM (Figure 2.4) converted into solid ice equivalent using a firn depth correction from RACMO2 (*Ligtenberg et al.*, 2011) to obtain the ice draft elevation in ice equivalent. The reconstructed MC ice draft reveals a fjord-like landscape with a deep trough spanning the entire 25 km width of the fast portion of TG (Figure 2.10). The trough is 2,000-2,300 m deep and bounded by 2,000 m high walls on both sides. Immediately upstream from the distinct two-lobe pattern of the grounding line, the bed topography is different: the southern lobe is 500 m deeper than the northern lobe. Upstream of the southern lobe, the bed remains nearly level at the center for another 7 km, then rises slowly with a 4% slope. In contrast, the northern lobe sits on a prograde bed, i.e. the bed rises upstream of the grounding line with a 7.5% slope for 3 km, and then flattens out.

2.3   Hydrostatic potential

The TanDEM-X DEM (Figure 2.4) and MC bed (Figure 2.10) are combined to calculate the hydrostatic potential (HP) of ice expressed in meters of elevation above hydrostatic equilibrium (Figure 2.11) following *Shreve* (1972) and *Fricker and Scambos* (2009):

$$\Phi = \rho_{ice}g(z_{surface} - z_{bed}) + \rho_{sw}gz_{bed} \tag{2.7}$$

where ρ_{ice} and ρ_{sw} are density of ice and sea water, respectively; g is the gravity acceleration; $z_{surface}$ and z_{bed} are elevation of glacier surface and bed. Surface elevations are referenced to mean sea level using the EIGEN-6C geoid (*Förste et al.*, 2012). A density of 917 kg/m^3 is assumed for ρ_{ice} and 1028 kg/m^3 for ρ_{sw} since the ice shelf thickness calculated using these values assuming hydrostatic equilibrium best fits the ICECAP ice thickness data. The nominal error in HP is estimated to be 8 m from the 3 m nominal error in the DEM and 60 m error for the ice draft.
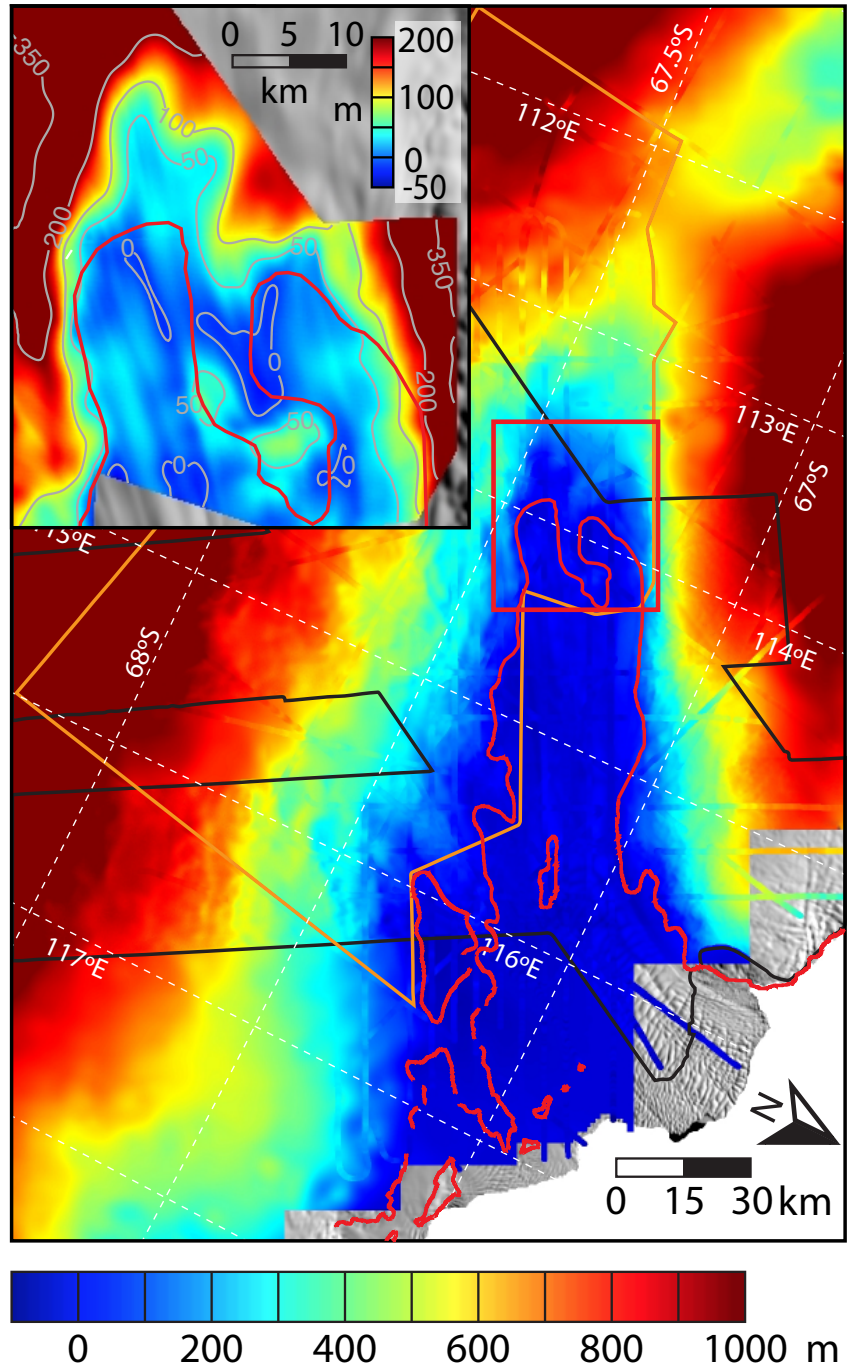
Figure 2.11: Hydrostatic potential of Totten Glacier. Black polygons denote the boundaries of TDX DEM mapping versus BEDMAP2 (*Fretwell et al.*, 2013). Orange polygons delineate the boundaries of the mass conservation (MC) domain versus BEDMAP2. 1996 Grounding line line in red. The redbox is zoomed in the inset on a different color scale. This figure is from *Li et al.* (2015a).

The bed topography is strongly reflected in the HP map. In the proximity of the grounding line, the hydrostatic potential is mostly in the range of 0-20 m. Upstream of the southern lobe, we detect a 7-km long by 8-km wide "ice plain", similar to the one reported for Pine Island Glacier (*Corr et al.*, 2001), i.e. an area with relatively flat surface topography, grounded only a few tens of meters above hydrostatic equilibrium. Beyond the northern lobe, the HP contours are more closely spaced due to the presence of a bump in bed topography. The ice island separating the two lobes is less than 60 m above hydrostatic equilibrium, hence apparent to an ice rumple, i.e. an area where ice overrides a bump in the seafloor but does not decrease its speed to zero.
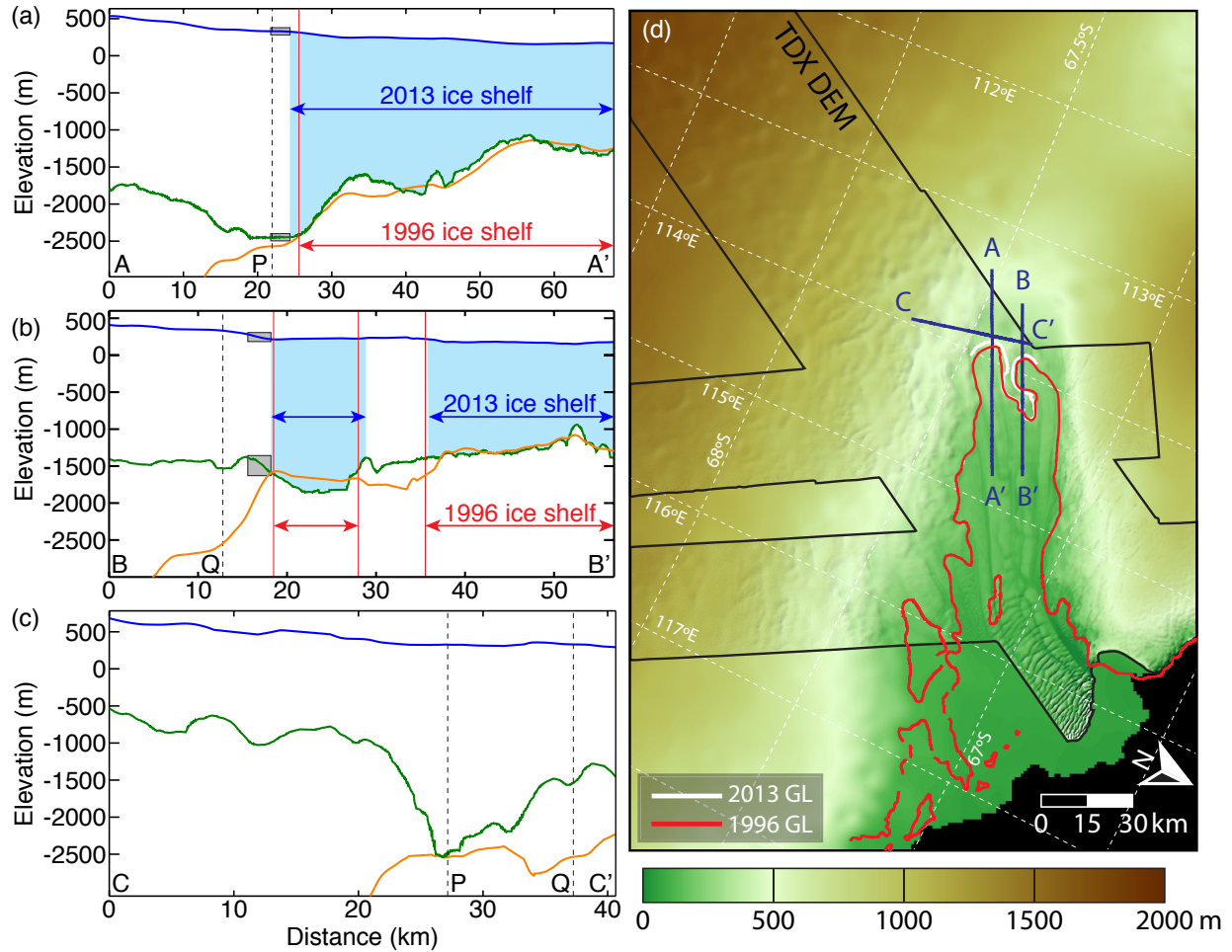
Figure 2.12: ICECAP surface (blue), ice draft (green) and hydrostatic equilibrium ice bottom (orange) of Totten Glacier, East Antarctica, along tracks (a) AA', (b) BB' and (c) CC' in the map on the right. Blue shade is floating ice based on the 2013 grounding line. Ice floatation in 1996 is delineated by a red line. P and Q mark the intersections of AA' and BB' with CC', respectively. Grey boxes in (a) and (b) delineate the portion over which we calculate surface and bed slopes. This figure is adapted from *Li et al.* (2015a).

Three ICECAP profiles AA', BB' and CC' with high resolution, direct observational surface and bed elevation data are examined to provide a closer look at the hydrostatic balance of the grounding line region. Figure 2.12 shows the surface elevation and ice draft elevation, as well as the departure of the ice draft from hydrostatic equilibrium. Along AA' on the southern lobe, the ice draft shows no significant deviation from hydrostatic equilibrium (< 120 m) until 7 km upstream of the grounding line, which marks the virtual limit of the ice plain.

publication	time span	dh/dt (m/yr)	location
Zwally et al. (2005)[*]	1992-2001	-0.448±0.048	grounded ice (fast)
Shepherd and Wingham (2007)[*]	1992-2003	-0.25±0.05	grounded ice (fast)
Pritchard et al. (2009)[†]	2003-2007	-1.9	grounded ice (fast)
Flament and Rémy (2012)[§]	2002-2010	-1.2±0.6	grounded ice (fast)
Horwath et al. (2012)[§]	2002-2009	-0.2	grounded ice (fast)
Pritchard et al. (2012)[†]	2003-2008	-0.41±2.81	ice shelf (inner)
		+0.04±0.5	ice shelf (outer)
		0.00	grounded ice (slow)
		-1.6	grounded ice (fast)
McMillan et al. (2014)[‡]	2010-2013	-0.52±0.012	grounded ice (fast)
Paolo et al. (2015)[*§]	1994-2012	+0.2±0.75	ice shelf

Table 2.1: Summary of previously published altimetry results on Totten Glacier. dh/dt is the rate of change in ice thickness, positive value means the ice is thickening, negative value means the ice is thinning. Superscripts in the left column denote the data source: ERS-1/2[*], ICESat GLAS[†], Envisat[§] and CryoSat-2[‡].

Along BB', the ice draft rises and diverges from the hydrostatic equilibrium immediately upstream of the grounding line: the hydrostatic ice bottom drops by 500 m in 2 km while moving inland. At the location of the ice island separating the two lobes, no bedrock ridge is present. Instead, there is a 50-m bump in surface elevation. CC' is a transverse flight track located 2 km upstream of the 2013 grounding line. CC' intersects AA' and BB' at locations P and Q, respectively, which are upstream of the southern and northern lobes. At P, the ice is close to hydrostatic equilibrium and grounded 2,400 m below sea level. At Q, the ice draft is only 1,400 m deep and the ice is well above hydrostatic equilibrium.

2.4 Elevation change

Satellite altimetry records since 1992 have shown significant surface lowering over the grounded part of Totten Glacier (Table 2.1). Most of the observed thinning is concentrated in regions of low elevation with fast flow (Figure 2.13), with the maximum values found near the grounding line. The reported thinning rates increased from about 0.5 m/yr in the 1990s (*Shepherd*

and *Wingham*, 2007; *Zwally et al.*, 2005) to about 1.5 m/yr in 2003-2009 (*Pritchard et al.*, 2009; *Horwath et al.*, 2012; *Flament and Rémy*, 2012), and may have decreased in recent years (*McMillan et al.*, 2014). The geographic pattern of the thinning is indicative of a dynamic origin. However, on the floating ice shelf, examination of the long-term record of surface elevation is challenging, in part due to the complexity of the surface mass balance regime in this region. Available data on the ice shelf are not conclusive of a significant thinning or thickening trends but rather indicative of fluctuations (*Paolo et al.*, 2015).
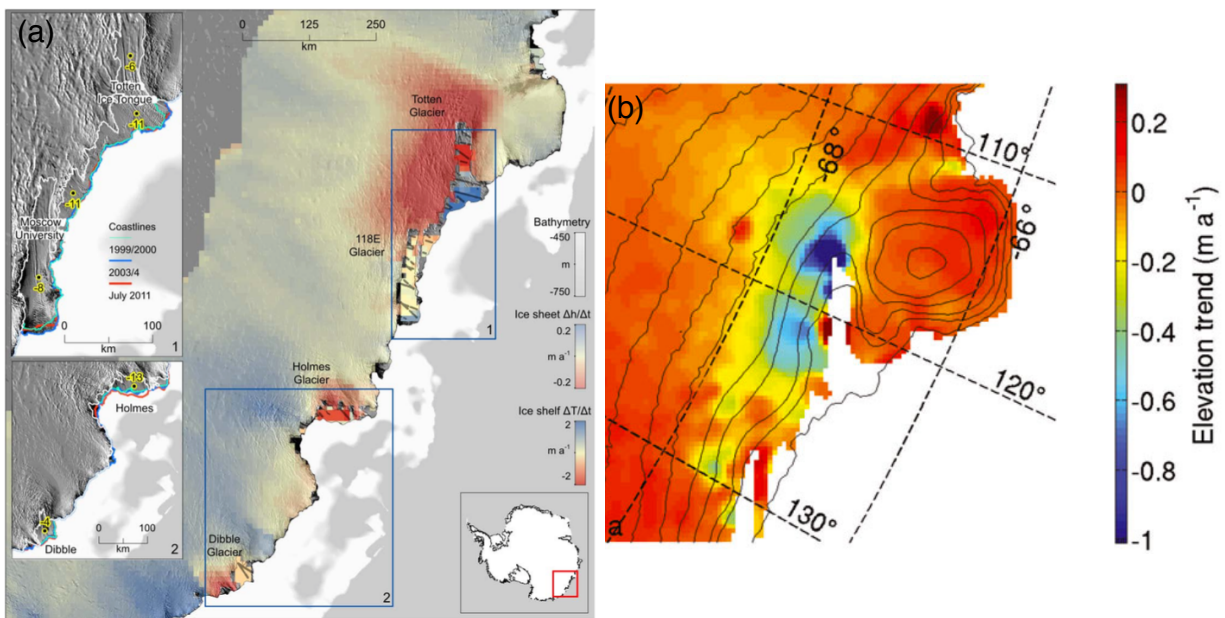
Figure 2.13: dh/dt map on Totten Glacier from (a) *Pritchard et al.* (2012) and (b) *Flament and Rémy* (2012). Grey lines in (a) show locations of ICESat dh/dt measurements. Yellow-edged black labels in insets of (a) are modelled firn dh/dt signal in cm/yr for 2003-2008. Elevation contours in (b) are spaced at 250 m.

2.4.1 Mapping surface elevation change on Totten Glacier using TanDEM-X data

Repeat acquisitions of TanDEM-X data allows for elevation change mapping on Totten Glacier (*Mouginot et al.*, 2014a). Part of the glacier was surveyed on repeat orbits twice

in 2011 and 2013 along two ascending tracks (Figure 2.14a). The DEMs at the two epochs are differenced to derive a map of dh/dt (Figure 2.14b). The map shows a well correlated geographic pattern between dh/dt and velocity. Along profile AA' across the grounding line, dh/dt stays near zero in regions with stagnant flow slower than 200 m/yr. At the center of the ice stream with fastest flow, a clear thinning signal up to 5 m/yr is observed. When it comes to the shear margins with strong velocity gradient, the noise in dh/dt becomes larger due to the high strain rates. Similar correlation between velocity and dh/dt is found along BB' across the ice shelf and the eastern sub tributary. The eastern sub tributary has a much smaller velocity of ∼400 m/yr compared to the main trunk, but a clear thinning signal is present. On the ice shelf, dh/dt profile shows large wiggles due to the motion of the surface crevasses. This problem can be possibly solved by using a Lagrangian analysis (*Moholdt et al.*, 2014). A small ramp in the track seaward produces slight bias on the dh/dt profile up to 3.5 m/yr near end B, most likely due to the residue errors in the absolute phase constant. These results should only be interpreted qualitatively at this stage, corrections in firn densification and tidal effects are necessary to draw any quantatively conclusions out of this dataset.
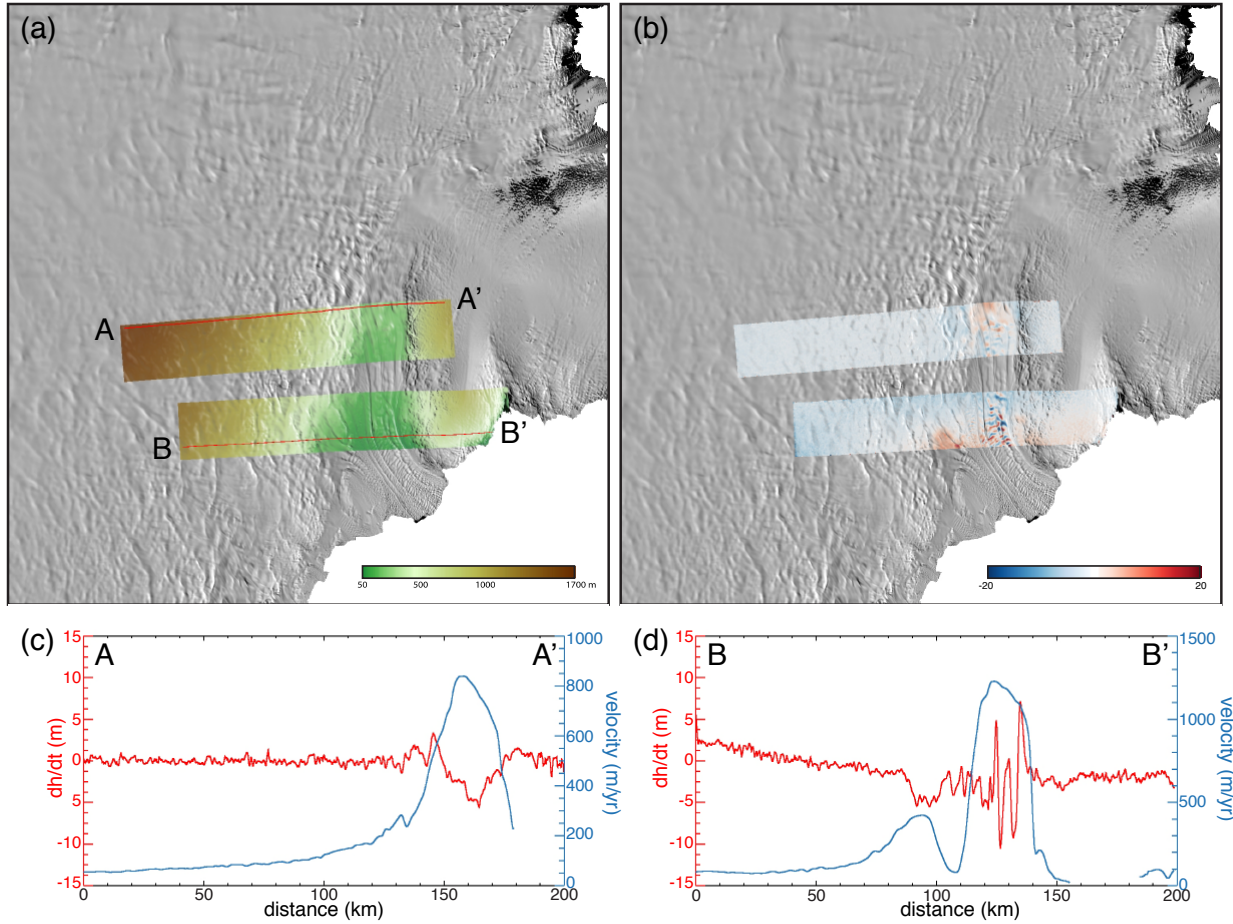
Figure 2.14: (a) Surface DEM of Totten Glacier derived from two TanDEM-X tracks, overlaid on a MOA image. AA' and BB' are along-track profiles plotted in (c) and (d), respectively. (b) is the dh/dt values calculated by differencing TanDEM-X DEM from 2011 and 2013. (c) and (d) plot dh/dt and velocity profiles along AA' and BB'. This figure is partly published in *Mouginot et al.* (2014a).

2.5 Summary

High-resolution DEMs derived from TanDEM-X InSAR data reveals abundant surface characteristics such as flow structures, crevasses and undulations which reflect basal topography. At the grounding zone, Totten Glacier has a bumpy surface topoggraphy with no significant break-in-slope between the grounded and floating portion.

A high-resolution ice thickness map is derived using a mass conservation method, combining InSAR-derived surface velocity and ice thickness measurements from airborne radar echo sounding. This map is subtracted from the TanDEM-X DEM to obtain a basal topography map of Totten Glacier. The reconstructed basal topography shows a deep trough along the ice stream with completely different bed conditions underneath the two-lobe shape grounding line: one lobe sits deeper with flat bed slopes upstream while the other is shallow and rises towards inland. A hydrostatic analysis of the grounding line shows that the deeper lobes is prone to further retreat, with a 7 km long by 8 km wide region right beyond the grounding line grounded only 0-50 m above hydrostatic equilibrium, or an "ice plain". In contrast, the steep bed at the shallow lobe will protect the glacier from fast retreat.

The surface topography of Totten Glacier was mapped twice in 2011 and 2013, allowing for detection of elevation change by DEM differencing. The result shows a significant thinning signal near the grounding line which is well correlated with fast flow. This pattern suggests a dynamic origin of the thinning that is consistent with prior altimetry results.

Chapter 3

Velocity change of Totten Glacier

Understanding the dynamic behavior of Totten Glacier is important because of the large potential sea level rise it could cause. Ground-based measurements in the 1970s (*Young*, 1979) was the first step towards a mass budget estimate of this glacier. Since the 1990s, satellite synthetic aperture radar interferometry (InSAR) largely completed our view at the rate of motion of this glacier (*Rignot*, 2002; *Rignot et al.*, 2008, 2011a). However, significant data gaps still remain upstream of the grounding line of Totten Glacier (Figure 3.1) (*Rignot et al.*, 2011a), which largely affects numerical modeling analysis.

Totten Glacier is particularly difficult to access by satellite SAR surveys. Being far from downlink stations in Antarctica, poor weather limits data quality for optical sensors and reduces coherence of SAR signal, especially for data acquired many weeks apart. Persistent katabatic winds and high accumulation of snowfall constantly rework the ice surface. Figure 3.2 shows two SAR amplitude images of Totten Glacier's grounding line with 1 day separation acquired by COSMO-Skymed in 2013 summer time. The surface looks very different after only 1 day. An additional complication of ice velocity mapping in the area is the absence of reference points of known velocity. While Law Dome is a good reference target, it is also a
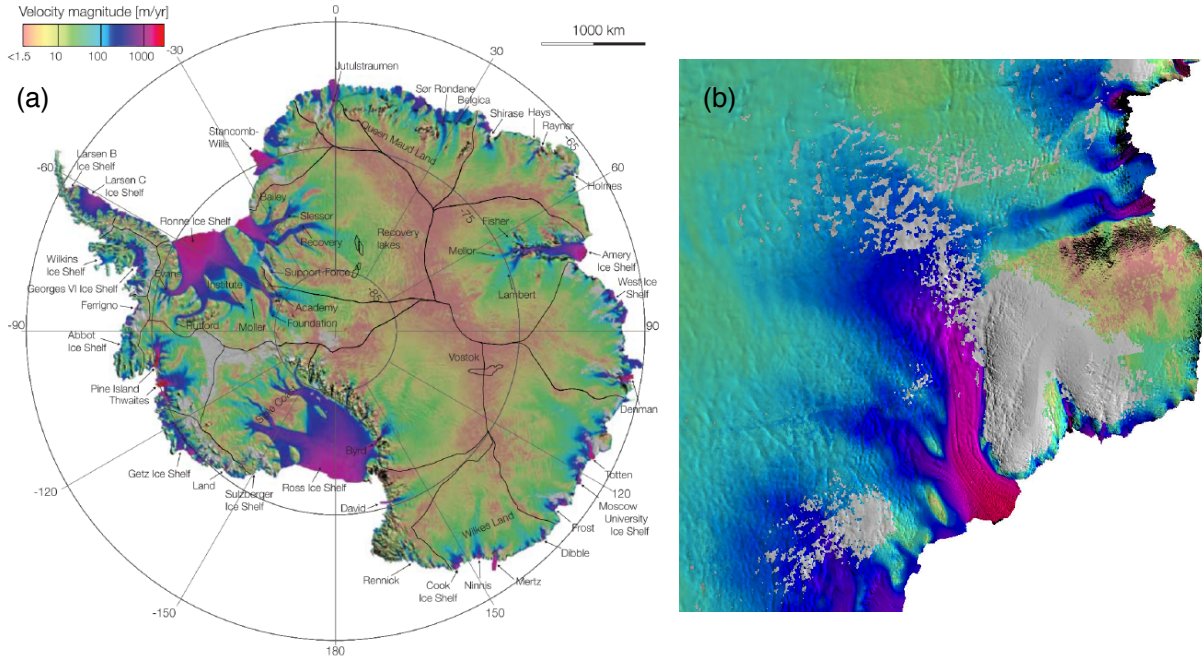
Figure 3.1: Antarctic velocity map (a) for International Polar Year 2007-2009 from *Rignot et al.* (2011a) and a zoom of Totten Glacier (b).

region of high snow accumulation (*Goodwin*, 1990), which limits the signal to noise ratio of SAR data and phase coherence. Few points with zero velocity are present along the coast (*Rignot et al.*, 2011a), which in particular requires the data to be extended to the ice divides, 200 km away from the grounding line, in order to get good control. Finally, there is strong ionospheric noise in the radar data in this sector near the south magnetic pole (*Mouginot et al.*, 2012). All these factors inhibit complete mapping of this glacier and detection of small changes in ice velocity.

This study presents a continuous record of ice velocity of Totten Glacier since 1989, going back to the Landsat-4 era, and extending to present using a suite of international SAR sensors and Landsat-8 in more recent years. The velocity mapping in 2007-2009 is from *Rignot et al.* (2011a), the rest is from this study. The 2013 Landsat-8 was processed by J. Mouginot (UC Irvine). The assembled ice velocity shows a good temporal correlation with the observed thinning rates and reanalysis ocean temperature data, indicating that the glacier is very sensitive to changes in oceanic conditions. This ice velocity record is the
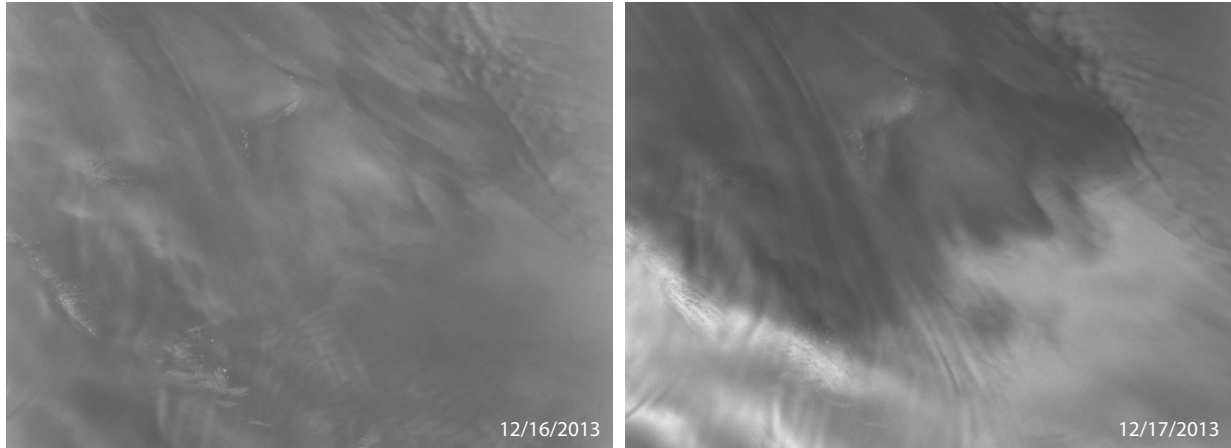
Figure 3.2: COSMO-Skymed SAR amplitude image on Totten Glacier acquired 1 day apart in summer 2013.

longest record developed to date.

3.1 Measurement of ice surface velocity

Advances in satellite remote sensing have greatly improved ice motion measurement and monitoring since 1970s. Three major techniques have been widely used to map large-scale ice motion:

1. Feature tracking using sequential optical images

2. Speckle tracking using SAR amplitude images

3. Satellite synthetic aperture radar interferometry

Each technique has its own strengthes and weeknesses, as well as associated errors. This section provides a brief review of these techniques.

3.1.1 Feature tracking

On fast flowing ice where stress is high, visible features such as crevasses and rifts form at the ice surface and move with the ice. These features can be tracked on sequential high-resolution optical images like Landsat, ASTER and SPOT. Sequential images should first be coregistered using satellite ephemeris information and fixed points like the coastline and bare rocks. Surface features are then located visually and their displacements can be measured manually. This approach requires accurate coregistration of the images and small, sharp surface features. The precision of the velocity measurements is limited by the spatial resolution and temporal separation of the images.

Algorithms for automated extraction of the displacements have been developed as well. The image-to-image cross-correlation algorithm allows for high-density velocity mapping by automatically searching for matching rectangular sub-image chips between the image pairs (*Scambos et al.*, 1992). This algorithm is more robust compared to conventional visual tracking due to the subpixel accuracy. Moreover, the cross-correlation algorithm is able to detect displacements of diffuse, extended features without losing any accuracy. The Landsat program launched in 1972 enables the large scale ice sheet velocity mapping using the cross-correlation algorithm, which significantly extends our observational record back in time. However, the feature tracking algorithm requires that identifiable features must be present at the surface, which is not the case for most of the interior regions of the Antarctic ice sheet. Moreover, the orbit information from early generations of Landsat satellites were not accurate enough for pixel-level co-registration. In areas with wide-spread fast flow like Totten Glacier, a lack of tie points could result in difficuties in velocity calibration. The most recent Landsat-8 Operational Land Imager (OLI) overcomes several of these limitations. The new sensor provides a 12-bit radiometric resolution which translate into 4096 grey levels, compared with 256 in the previous 8-bit sensor onboard Landsat-7. The high signal-to-noise ratio enables the new sensor to detect subtle surface features like un-crevassed sastrugi (*Klinger et al.*,

2014; *Fahnestock et al.*, 2014). Unlike crevasses and rifts which are confined in fast-flowing regions, these features are widely present at the ice sheet surface, from the coast to the interior. Therefore, velocity mapping using Landsat-8 data can be extended far into the interior of the ice sheet. Furthermore, the orbital information of Landsat-8 is accurate to less than a pixel, which benifits the calibration of derived velocities.

The feature tracking technique can be applied to SAR amplitude images as well. SAR images have several advantages against optical images when used for feature tracking. Firstly, the vision of SAR images are not hampered by cloud cover or darkness. Secondly, feature tracking is more efficient with SAR images due to the penetration of radar signals into the firn layer. Finally, the synthetic aperture technique provides meter level spatial resolution for SAR sensors compared to 15-60 m for Landsat sensors. Despite all these advantages, feature tracking on SAR images is rarely used for velocity mapping, because speckle tracing is a much more robust algorithm for velocity mapping using SAR images.

3.1.2 Speckle tracking

In ice sheet velocity mapping, conventional feature-tracking technique relies on the presence of surface features like rifts and crevasses. These features often appear in fast flowing coastal regions. However, in the vast interior of the Antarctic ice sheet, such features rarely exist. This problem is solved with SAR speckle. Speckle is an inherent "noise" in SAR images due to the wave interference in coherent radar echoes. The pattern of the speckle is determined by the scatterer at the surface. Speckle tracking applies cross-correlation to the coherent phase of small sub-image chips, searches for the peak correlation with high signal-to-noise ratio between SAR image pairs and finally obtains an offset map with sub-pixel precision. This method has been described in detail in *Schaum and McHugh* (1991)and *Michel and Rignot* (1999). The nominal precision of the speckle tracking technique is 1/30 of the sub-image

46

(*Rignot*, 2002).

The speckle tracking technique is robust and has been widely used in glaciology studies (e.g. *Rignot et al.* (2011a)). Compared to conventional feature tracking, speckle tracking on SAR images does not depend on solar illumination and clear sky conditions, nor identifable surface features. This technique provides velocity measurements in both range (across-track) and azimuth (along-track) directions, which is a big advantage compared to SAR interferometry (see section 3.1.3). The typical error range for ice velocity mapping from speckle tracking on satellite SAR data is 4-20 m/yr (*Rignot et al.*, 2011a). Although much larger than that of InSAR, it is acceptable for fast-moving glaciers.

3.1.3 Synthetic aperture radar interferometry

As discussed in section 2.1.1, the interferometric phase is sensitive to surface displacement. Expanding the ice motion term of Equation 2.1 (*Joughin et al.*, 1998):

$$\Delta\phi_d = \frac{4\pi}{\lambda}\delta r_g = \frac{4\pi}{\lambda}(\Delta_{d,x}\sin\theta - \Delta_{d,z}\cos\theta) \tag{3.1}$$

where $\Delta_{d,x}$ is the displacement component tangential to the reference ellipsoid in the across-track direction, $\Delta_{d,z}$ is the vertical displacement, λ is the wavelength of the radar, and θ is the incidence angle. If we assume the ice flow is steady between the acquisitions, which is true for most Antarctic glaciers, we can convert the displacements to velocity:

$$\Delta\phi_d = \frac{4\pi}{\lambda}\delta T(v_x\sin\theta - v_z\cos\theta) \tag{3.2}$$

where v_x and v_z are corresponding velocity for the displacements $\Delta_{d,x}$ and $\Delta_{d,z}$, and δT is the time separation between the SAR pairs. Solve for the horizontal across-track velocity

component:

$$v_x = \frac{\phi_d \lambda}{4\pi \delta T \sin \theta} + v_z \cot \theta \qquad (3.3)$$

Note that in all above equations, ϕ_d is the calibrated motion-only unwrapped phase so that zero phase means no surface displacement, this calibration could be done by calculating an absolute phase constant as introduced in section 2.1.1. By assuming the ice is flowing parallel to the ice surface, one can relate v_z with v_x using prior surface elevation information $z(x, y)$:

$$\frac{v_z}{v_x} = \frac{\partial}{\partial x} z(x, y) \qquad (3.4)$$

Combining Equation 3.3 and 3.4, the horizontal across-track velocity component can be derived.

In principle, InSAR can achieve millimeter precision in measuring surface displacements. But external error sources such as weather conditions and ionospheric perturbations can also play a role. *Michel and Rignot* (1999) estimated a statistical error of 1.4 cm/d for ice velocity measurement for an interferogram with 0.4 average phase coherence. This precision makes InSAR a powerful tool in glaciology studies. However, apparent drawbacks do exist. The interferometric phase is only sensitive to surface displacement in the range direction. To obtain 2-dimensional flow vectors, *Joughin et al.* (1998) combines InSAR-derived velocity components from ascending and descending orbits. This method provides accurate velocity measurements. However, it is not always the case that data from both orbits are available. On Totten Glacier, only one orbit direction is available in most cases.

An alternative method named multiple aperture InSAR, or MAI can be used to infer the azimuth ground motion (*Bechor and Zebker*, 2006). The aperture is split and the signal is integrated over a sub-apertures to form a forward-looking and a backward-looking inter-

48

ferograms. The phase difference between the two interferograms is sensitive to the surface motion in the along-track direction. Deciding on the size of the sub-apreture is tricky: The sensitivity of the phase to ground motion increases with the separation between two sub-apertures. Therefore, selecting two small sub-apertures at the both ends of the full aperture would achieve best phase sensitivity. However, the signal-to-noise (SNR) ratio decreases when reducing sub-aperture size. Statistical analysis shows that dividing the full aperture in half is optimum to balance the trade-off effects (*Bechor and Zebker*, 2006). The MAI approach outperforms the speckle tracking technique for InSAR pairs with short temporal separation in terms of precision.

3.2 Velocity mapping of Totten Glacier

3.2.1 Data and methods

In this study, both optical and synthetic aperture radar (SAR) data from a set of satellite platforms are used to derive ice surface velocities. The data includes the US Landsat MultiSpectral Scanner (Landsat-4), Enhanced Thematic Mapper Plus (Landsat-7), and Operational Land Imager (Landsat-8), the European Earth Remote Sensing imaging radar satellite (ERS-1/2), the Canadian RADARSAT-1 and RADARSAT-2 radar, the Japanese Advanced Land Observation System (ALOS) Phased-array L-band Synthetic Aperture Radar (PALSAR), the German TanDEM/TerraSAR-X (TDX/TSX), and the Italian COSMO-Skymed (CSK) constellation satellites. The data span 1989 to 2015 as shown in Table 3.1.

Ice surface velocities in 1989 and 2001 are derived from Landsat-4 band 3 and Landsat-7 band 8 (panchromatic) data to achieve the best contrast and spatial resolution. Sequential images are georeferenced to a Landsat-8 image from the same path/row with ground control points (GCPs) corresponding to near zero velocity in the Antarctic-wide map (*Rignot et al.*, 2011a).

year	sensor	λ (cm)	Δt (d)	time	n	processing
1989	Landsat-4	7×10^{-5}	224	03/28/89-11/08/89	1	feature tracking
1996	ERS-1/2	5.6	1	02/13/96-05/29/96	8	InSAR+MAI
2000	RADARSAT-1	5.6	24	09/07/00-11/13/00	9	speckle tracking
2001	Landsat-7	7×10^{-5}	1056	01/06/00-11/27/02	1	feature tracking
2005	ERS-1/2	5.6	35	09/07/05-10/12/05	1	speckle tracking
2006	ALOS PALSAR	23.6	46	05/20/06-08/13/06	9	speckle tracking
2007	ALOS PALSAR	23.6	46	09/08/07-01/14/08	20	speckle tracking
2008	ALOS PALSAR	23.6	46	09/10/08-01/24/09	23	speckle tracking
2009	ALOS PALSAR	23.6	46	09/13/09-01/19/10	6	speckle tracking
2010	ALOS PALSAR	23.6	46	09/28/10-01/30/11	8	speckle tracking
2011	TDX/TSX	3.1	11/22	06/10/11-08/12/11	3	speckle tracking
	TDX	3.1	11/33	06/13/13-07/28/13	3	speckle tracking
2013	TSX	3.1	11	10/02/13-11/13/13	5	speckle tracking
	CSK	3.1	3	12/07/13-12/20/13	2	speckle tracking
	Landsat-8	6×10^{-5}	48	11/18/13-01/20/14	3	feature tracking
2015	RADARSAT-2	5.5	24	02/22/15-03/18/15	1	speckle tracking

Table 3.1: InSAR satellite data used to map the ice velocity of Totten Glacier, East Antarctica: year, sensor name, radar wavelength λ in centimeters, repeat cycle Δt in days, time of acquisition, number of tracks n, and processing technique.

The registration accuracy is better than 1 pixel (30 m for Landsat-4, 15 m for Landsat-7). Small scale (< 5 pixels) ice surface features like crevasses and rifts are identified and tracked on pairs of registered images. The displacements are then measured and converted into velocity vectors (Figure 3.3). An accuracy of 2 pixels is estimated in the measured displacements, which translates into an error of ±98 m/yr (1σ) for Landsat-4 data in 1989 and ±10 m/yr for Landsat-7 data in 2001.

ERS-1/2 data from 1996 are processed interferometrically and the line-of-sight (across-track) velocity component is derived (*Goldstein et al.*, 1993). The phase coherence is high due to the 1 day repeat cycle. Tidal signals on the ice shelf are removed using tide products from CATS2008a_opt tide model (*Padman et al.*, 2008) and the TPXO6.2 load model (*Egbert and Erofeeva*, 2002) following *Scheuchl et al.* (2012). No ascending passes exist in this area, so it is not possible derive a two-dimensional flow vector (*Joughin et al.*, 1998) using InSAR. Instead, the multiple aperture interferometry (MAI) technique (*Bechor and Zebker*, 2006)
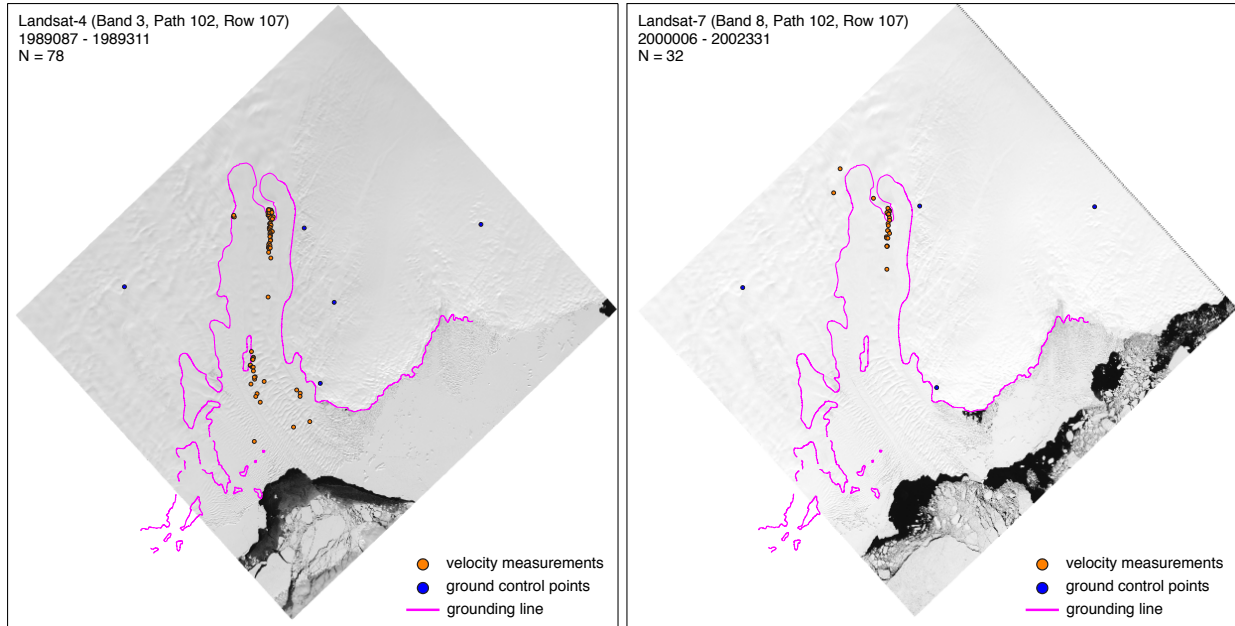
Figure 3.3: Velocity measurements from manual feature tracking on 1989 Landsat-4 and 2000-2002 Landsat-7 data. This figure is from *Li et al.* (2015b).

is applied to derive the along-track velocity component. The error in velocity mapping is mainly from the ionosphere perturbation along track, and estimated to be 49 m/yr.

The remaining SAR data are processed using a speckle tracking algorithm (*Michel and Rignot*, 1999), with 2007-2009 velocities from *Rignot et al.* (2011a), and the remainder from this study. This study uses RADARSAT-1 24-day repeat data for year 2000, ERS-1 35-day repeat data for 2005, ALOS PALSAR 46-day repeat data for five consecutive years during 2006-2010, TDX/TSX 11-day repeat data for 2011, and RADARSAT-2 24-day repeat data for 2015. Multiple datasets in 2013 are employed: 11-day repeat TDX/TSX data, 3-day repeat CSK data, and 48-day repeat Landsat-8 data. For Landsat-8 data, instead of tracking SAR speckles, the cross-correlation algorithm tracks subtle surface features like sastrugi. As these features may move with the wind, analysis of the corresponding displacement vectors must be done with caution. Here, the processing chain of *Mouginot et al.* (2012) is used. Long tracks of SAR images spanning the entire drainage basin are employed whenever they are available to ensure good calibration (*Mouginot et al.*, 2012). The estimated errors range

from 10 m/yr to 17 m/yr depending on data repeat cycle and the operating frequency of the sensor.

3.2.2   Velocity patterns of Totten Glacier

The velocity maps are presented in Figure 3.4. The most complete maps are from ALOS PALSAR L-band data in 2007-2008. The L-band sensor has a longer wavelength compared to the C-band ERS-1/2 and RADARSAT-1/2 and X-band TDX/TSX and CSK sensors which penetrates deeper down into the firn layer. The ALOS PALSAR data has good temporal coherence since it avoids most of the noise due to surface weathering. Although it suffers from stronger ionospheric perturbations due to the longer wavelength, ALOS PALSAR has a good sensitivity to ice motion due to its long 46-day repeat cycle. *Rignot et al.* (2011a) estimated a 17 m/yr precision in velocity measurements from ALOS PALSAR data, which is acceptable for fast moving regions. In 2006, 2009 and 2010, the velocity mapping is limited to Vanderford Glacier in the west due to data availability, but still covers most of the fast flowing portion of Totten Glacier.

In 1996, only ERS-1/2 descending tracks are available. The velocity component in the azimuth direction is derived from MAI. During a short repeat cycle of 1 day, the surface displacement is small compared to noise from ionospheric perturbation. This noise apprears as strong azimuth streaks in the azimuth direction and the statistical error in the velocity mapping is 50 m/yr. In 2000 and 2005, sparse velocity measurements are obtained from C-band data with long repeat cycles due to temporal decorrelation. In 2011, only three short TDX/TSX tracks are available for velocity mapping, the speckle tracking fails on the ice shelf where the fast flow causes large deformations. In 2013, SAR data are only available near the grounding line with widespread fast flow, these data are cross-calibrated with Landsat-8 data, which has a good spatial coverage but lower precision. The most recent measurement
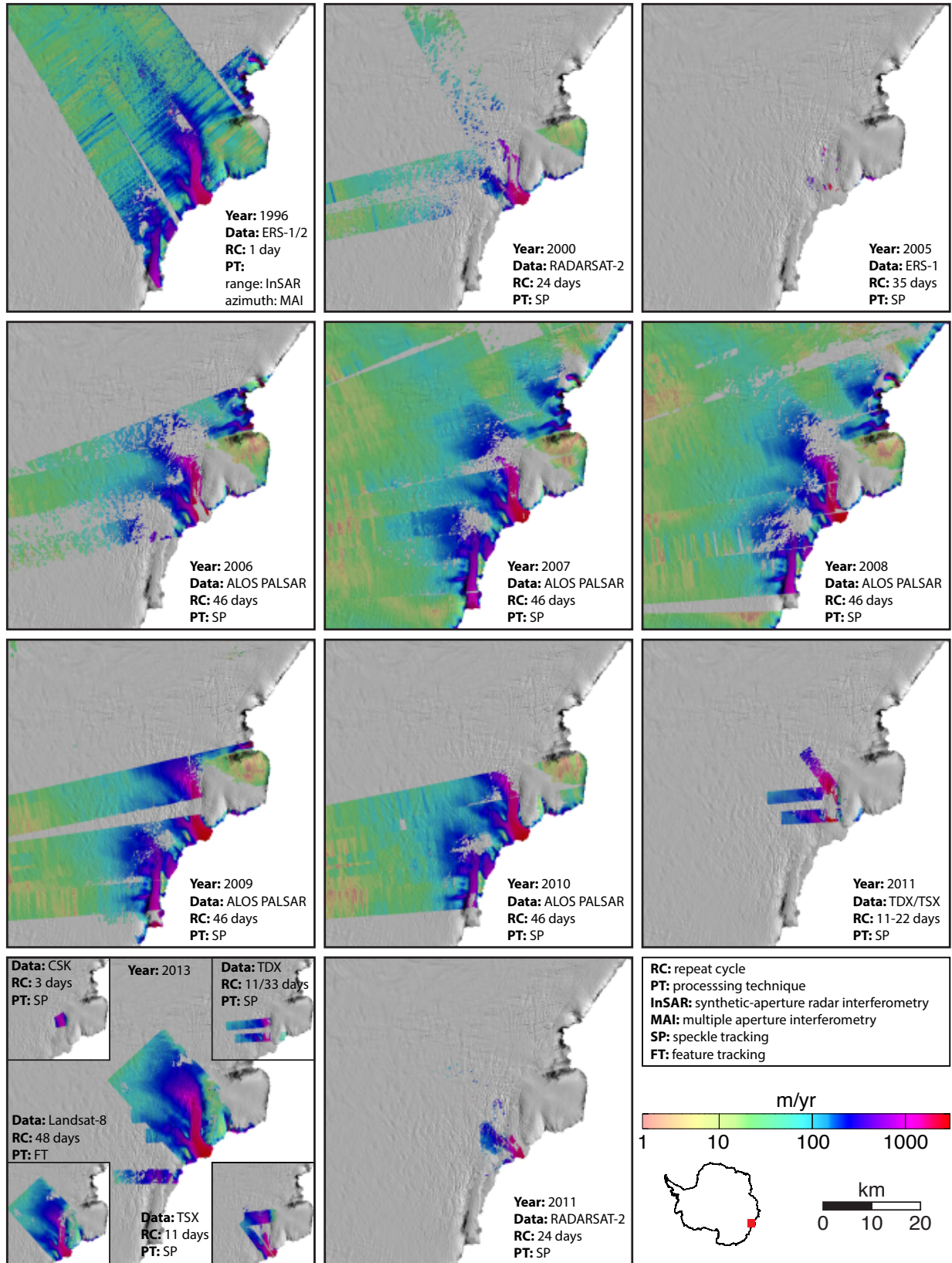
Figure 3.4: Annual velocity maps of Totten Glacier, East Antarctica. This figure excludes velocities from year 1989 and 2001, when velocity is measured by manual feature tracking using Landsat image pairs (see Figure 3.3). See also Table 3.1 for the complete list of velocity measurements. This figure is from *Li et al.* (2015b).
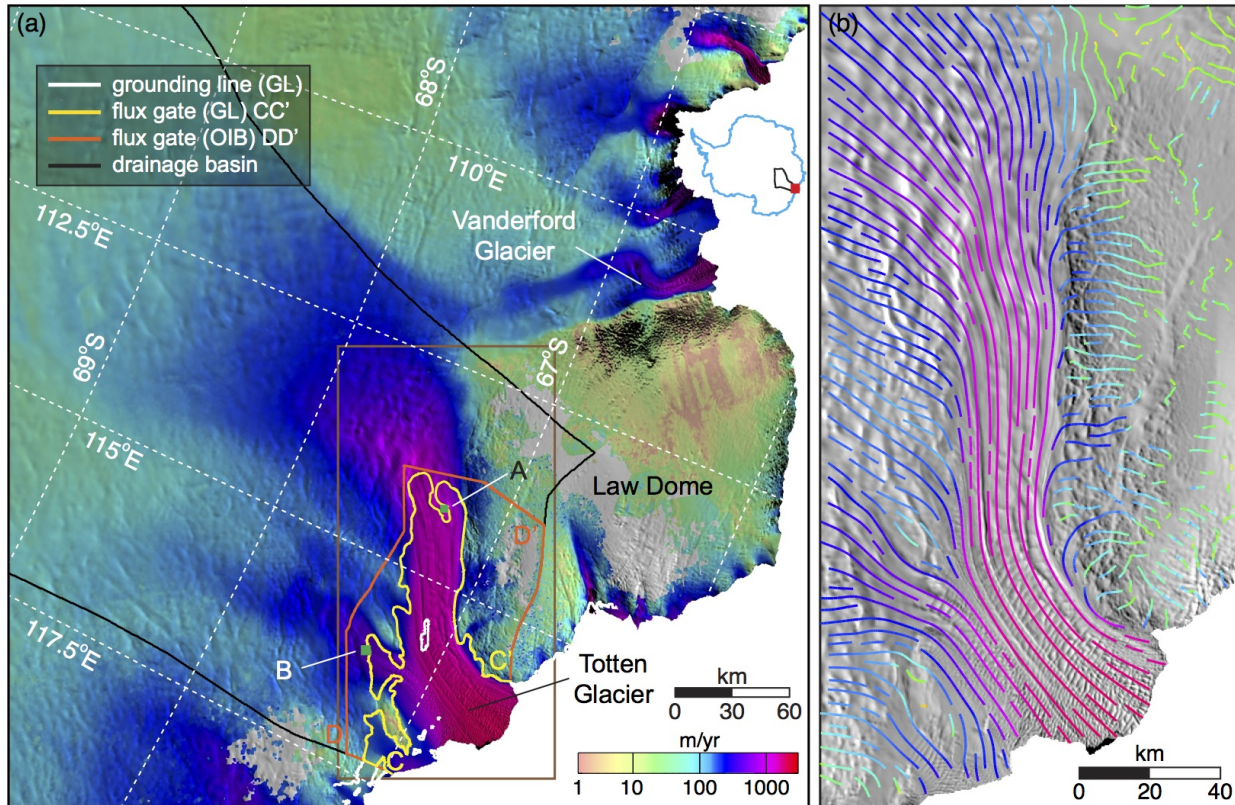
Figure 3.5: (a) Ice velocity magnitude and (b) direction of Totten Glacier, East Antarctica, color coded on a logarithmic scale and overlaid on a Moderate Resolution Imaging Spectroradiometer Mosaic of Antarctica (MOA) (*Scambos et al.*, 2007). The speed is mapped combining ALOS PALSAR data from 2007-2010. A few data gaps are filled with 2006 ALOS PALSAR, 2011 TDX/TSX, 2013 TDX/TSX, CSK and Landsat-8 data. The grounding line (GL) (*Li et al.*, 2015a) is solid white. The flux gates are solid yellow (GL) and orange (along Operation IceBridge (OIB) ground tracks). Green boxes A and B delineate the portion where we develop ice velocity time series (Figure 3a). The brown box is the map outline for (b).

from RADARSAT-2 has good coherence but limited coverage.

From year 2007 to 2010, ice velocity of Totten Glacier is rather stable with a temporal fluctuation less than 4%. The velocity maps from these years are stacked to generate a complete velocity map with best spatial coverage (Figure 3.5), the remaining data gaps are filled with data from the other years. Figure 3.5 shows the surface velocity magnitude and direction of Totten Glacier. This map has no gaps near the grounding line and is more complete than *Rignot et al.* (2011a) (Figure 3.1). The pattern of fast flow (above > 50

m/yr) initiates in the deep Aurora Subglacial Basin, about 350 km from the coast. The ice flow is then diverted into two tributaries along the flanks of Law Dome, one towards Vanderford Glacier to the west and the other to Totten Glacier on the east. Totten carries most of the ice, and flows down a confined, 25 km wide ice shelf at a speed of about ∼800 m/yr. This is a typical value in East Antarctica (*Rignot et al.*, 2011a), but a low value compared to ice shelves in the Amundsen Sea sector of West Antarctica (*Mouginot et al.*, 2014b). On the broad eastern side of the grounding line, an independent tributary that initiates 190 km inland merges into the main ice stream at about 430 m/yr. At the ice front, the ice shelf flows at about 1,800 m/yr and calves off with an iceberg production of about 28±2 Gt/yr (*Rignot et al.*, 2013). Comparison of the grounding line flux with the ice front calving with correction for SMB in between indicated an area-average melt rate of the ice shelf of 10.5±0.7 m/yr (*Rignot et al.*, 2013).

3.3   Velocity change of Totten Glacier

Two velocity time series have been extracted at boxes A and B on Figure 3.5, representing the velocity temporal variability at the grounding line in the main trunk and in the eastern tributary, respectively. Figure 3.6a shows the velocity time series. At the grounding line of Totten (box A in Figure 3.5), the ice speed decreased by 86 m/yr, or 12% during the time period 1989-2000. The glacier speed then increased by 120 m/yr, or 18%, to peak around 2007. Since 2007, the glacier has remained rather stable, with a slight decrease in speed of 30 m/yr, or 4% in 7 years. These changes in ice speed are also reflected on the ice shelf, with larger absolute magnitude change but similar or smaller percentage change (Figure 3.7). In a region about 15 km from the ice front, we detect strong fluctuations in speed between year 2009 and 2010 (Figure 3.7c), however, no associated calving events have been observed in the time period. From 2000 to 2007, the acceleration in ice flow has extended about 33 km
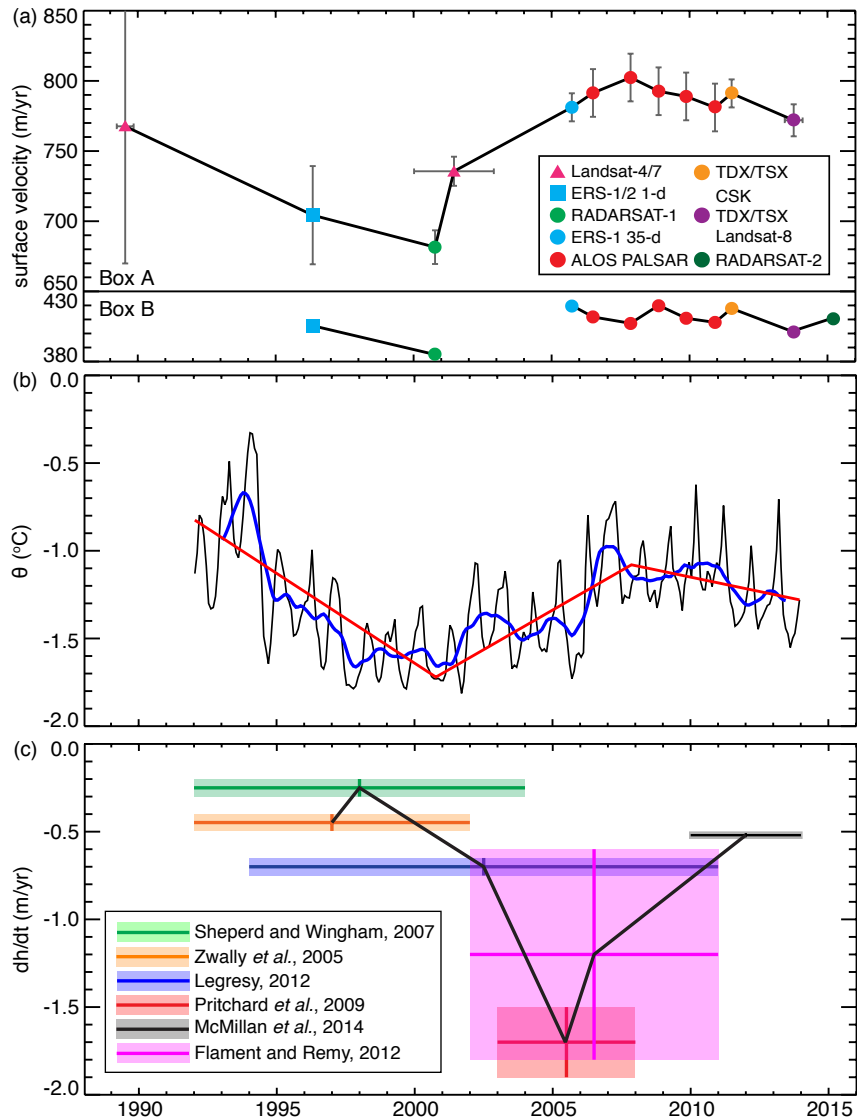
Figure 3.6: Times series of ice velocity (a), sub-surface ocean potential temperature (b), and dh/dt of Totten Glacier. (a) shows velocity change at the grounding line (box A on Figure 3.5) on top, and at the east sub-tributary (box B on Figure 3.5) at the bottom grey region. The error bars for the bottom time series are the same as the top panel. Potential temperature in (c) is from ECCO2 solution (*Menemenlis et al.*, 2008) and averaged over a box bounded by 115º E to 118º E and 65.5º S to 67º S. The blue line is the moving average with a 12-month window. The red lines are fitted using a piecewise linear regression with fixed breakpoints inline with 2000 and 2007 velocity measurements. The values in (c) are from previous studies on satellite radar/laser altimetry, see Table 2.1 for details. The blue bar is from personal communication with B. Legresy (LEGOS). This figure is adapted from *Li et al.* (2015b).

upstream the grounding line. In the deceleration period from 2007 to 2013, the inland limit of the speed change was only about 8 km upstream of the grounding line. Most changes in speed are localized in the immediate vicinity of the grounding line, both on grounded ice and on the ice shelf. The inland portion of the drainage system has for the most part remained relatively stable. At the eastern tributary (box B in Figure 3.5), a similar pattern of velocity change is detected, but at a much smaller magnitude (Figure 3a). At this location, the variability in flow speed is within 50 m, close to the measurement error. Overall, there is no clear trend of velocity change along the eastern tributary, most of the detected changes are concentrated on the main trunk of the glacier (Figure 3.7a, b).

Figure 3.6b presents a time series of continental shelf ocean temperature in front of Totten Glacier. In order to compare with the velocity time series, a piecewise linear regression is applied with breakpoints fixed at 2000 and 2007 to extract trends for the observed acceleration/deceleration periods. The fitting yields a statistically significant trend. Before 2000, when the ice flow slows down, the sub-surface ocean water on continental shelf experiences a strong cooling. Between 2000 and 2007, the glacier experiences an acceleration while the ocean warms up. Since 2007, the seawater cools down with a decrease in speed of the ice flow. It is worth noting that the fitted trends are possibly underestimated due to the piecewise linear fitting with fixed breakpoints, these results should only be interpreted qualitatively.

The pattern of ice speed change is consistent with the altimetry observations in terms of both spatial and temporal patterns. Most of the observed thinning takes place in areas of fast flow. The temporal fluctuations in ice velocity are well correlated with the previously reported thinning rates (Figure 3.6c, Table 2.1). In the 1990s during the ERS-1 Radar Altimeter mission, a surface lowering rate less than 0.5 m/yr is detected over Totten Glacier (*Shepherd and Wingham*, 2007; *Zwally et al.*, 2005). This time period corresponds to the period of slow flow (before 2003) in the velocity records. The Ice, Cloud and Land Elevation Satellite (ICESat) laser altimeter detects a much larger thinning rates of more than 1 m/yr

(*Flament and Rémy*, 2012; *Pritchard et al.*, 2009; *Horwath et al.*, 2012) in 2003-2009 when Totten is flowing at a high speed. After 2010, the velocity decreases, and the new Cryosat-2 data shows a reduction in thinning rate to 0.52 m/yr (*McMillan et al.*, 2014).

A recent study suggested the presence of a channel beneath the eastern tributary which could provide a pathway for warm modified Circumpolar Deep Water (mCDW) into the ice-shelf cavity and induce high melt rates (*Greenbaum et al.*, 2015). This part of the glacier flows over a shallow part of the ice shelf cavity (*Greenbaum et al.*, 2015). Prior observations of grounding lines (*Rignot*, 2002) are not consistent with the existence of this channel, and the observations of ice velocity change in this study, together with altimetry data, do not suggest that this sector corresponds to the area of most significant dynamic change. We posit that mCDW most likely accesses the cavity directly over the main sill in front of the ice shelf, floods the deepest part of the cavity, and induces ice shelf melting. This part of the cavity coincides with the main trunk of Totten with the highest melting rates in the cavity (*Rignot et al.*, 2013). Ice shelf melt rates are higher in this deep region partly due to the pressure dependence of the melting point of ice.

3.4   Summary

13 years of ice velocity in the past 26 years are assembled using optical and InSAR data from a suite of satellites. The velocity map of Totten Glacier is completed on the basis of *Rignot et al.* (2011a), with no gaps in the fast flowing trunk of the glacier. Minor gaps still remain on the stagnant Law Dome and on the coast to the east, which are not part of the drainage system. The complete velocity map shows the entire drainage system of Totten Glacier and Vanderford Glacier sharing the same origin and separated by Law Dome near the coast. Totten Glacier flows down a confined ice shelf bounded by Law Dome to the west, with an independent sub-tributary merging into the main stream to the east. The grounding
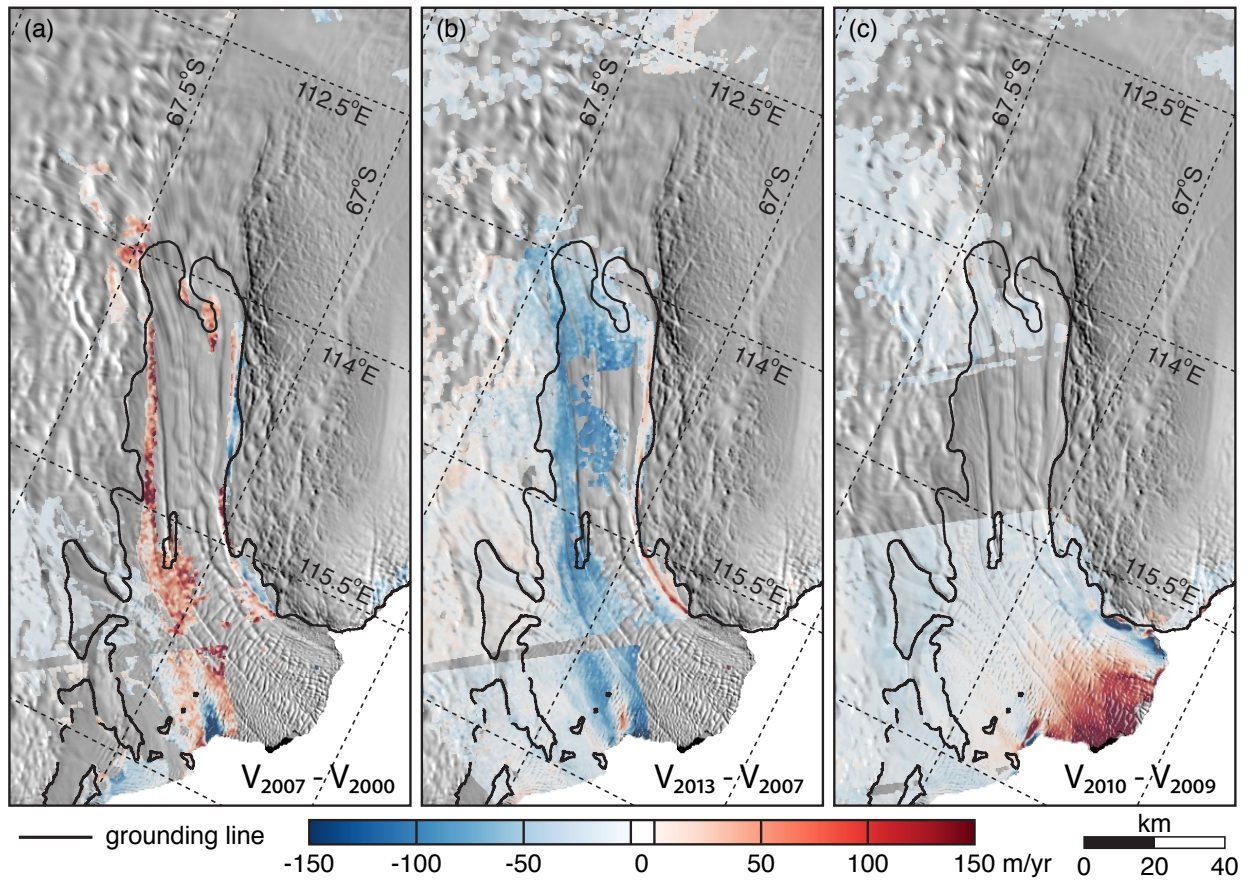
Figure 3.7: Change in flow speed from year (a) 2000 to 2007; (b) 2007 to 2013; and (c) 2009 to 2010 on Totten Glacier. Grounding line is plotted in black. This figure is from *Li et al.* (2015b).

line speed of 800 m/yr is typical for an East Antarctic glacier, but much slower than glaciers in the rapid changing Amundsen Sea Sector in West Antarctica.

The time series analysis of the annual velocity maps show strong fluctuations of up to 18% in flow speed at the grounding line, consisting of two deceleration periods 1989-2000 and 2007-2015, and an acceleration period from 2000 to 2007. This temporal variation is in phase with changes in dh/dt rates reported by satellite altimeters, confirming the conclusion of dynamic change. Moreover, the velocity change is well correlated with sub-surface ocean temperatures from reanalysis data, indicating that Totten Glacier is very sensitive to oceanic perturbations.

Most of the observed speed change occurs in the fast flowing portion of the glacier, on the ice shelf and near the grounding line, consistent with areas of strong ice thinning according to altimetry observations. The speed change does not spread far inland, and most of the drainage system stayed unaffected. The speed change pattern is different from that of glaciers in West Antarctica such as Pine Island Glacier and Thwaites Glacier. This is possibly due to the prograde bed topography, which protects the glaicer from marine ice sheet instability.

Chapter 4

Grounding line retreat of Totten Glacier

The transition boundary between the grounded part of the ice sheet and its floating extension is termed the grounding line. As the ice flows across the grounding line and enters the ocean, basal friction disappears and the oceanic heat transport induces bottom melting. Basal melt rate reaches its maximum near the grounding line with high sensitivity to local ocean temperatures (*Rignot and Jacobs*, 2002), especially for deep grounding lines like the one of Totten Glacier. Changes in bottom melting modify the ice thickness and migrate the grounding line, eventually resulting in changes in ice velocity and mass balance. Grounding line dynamics governs the evolution of marine-terminated glaciers, monitoring the position of the grounding line is therefore crucial.

While *in situ* measurements from GPS and tiltmeters have proved successful in detecting the grounding zone (*Smith*, 1991; *Vaughan*, 1995), they are costy and impractical for large-scale mapping. To map the grounding line using remote sensing techniques, a detailed understanding of the grounding line characteristics is necessary. Figure 4.1 is a schematic
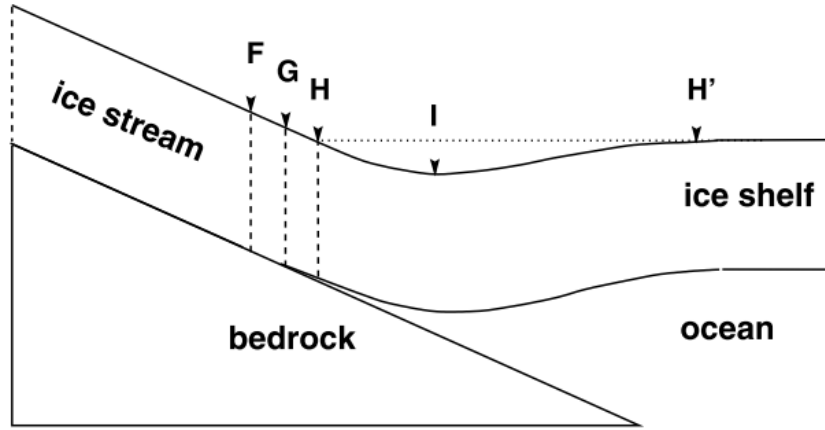
Figure 4.1: Schematic of the grounding zone. F is the inland limitation of the tidal flexure, G is the grounding line, I_b is the point of slope break, H and H' are points at hydrostatic balance (HB). Inland of H, ice is beyond HB; Between H and H', ice is below HB; Seaward of H', the free ice shelf is at HB. The vertical scale in this diagram is exaggerated for display. The grounding zone between F and H' is usually several kilometers long. This figure is from *Fricker et al.* (2002), as an adaption of *Vaughan* (1994).

diagram of the grounding zone structure (*Fricker et al.*, 2002). The ice shelf experiences cyclic flexure due to the vertical tidal motion, the flexure extends upstream of the grounding line G by a small distance at point F. Upstream of the grounding line G, the ice is grounded above hydrostatic balance. Once the ice passes the G and enters the ocean, it dives below hydrostatic equilibrium at H and comes back to become free ice shelf at H'. The flexure zone usually has a local elevation minimum between H and H', which corresponds to sharp changes in surface slope at point I.

Early studies took advantage of the slope break in ice sheet surface to infer the grounding line position (*Bamber and Bentley*, 1994; *Bohlander and Scambos*, 2007). This method works well in areas with stagnant flow. On fast flowing ice streams, however, the change in surface slope is gradual, leading to mislocation of the grounding line (*Fricker et al.*, 2009; *Rignot et al.*, 2011b). *Rose* (1979) and *Fricker et al.* (2002) used ice surface and thickness profiles from radar sounding to locate the grounding line based on buoyancy calculations. While providing a good initial determination, the hydrostatic point does not coincide with the

grounding line perfectly. The length of the grounding zone (F to H') is typically around 9 kilometers (*Rignot*, 2001), varying with ice thickness, local density of ice and sea water, and ice rheology (*Vaughan*, 1995). Precise knowledge of the grounding line location is important as it is often used as the flux gate in the mass budget calculation. Since the ice shelf experiences largest melt rates near the grounding line, ice fluxes calculated using a flux gate seaward of the actual grounding line will result in significant biases in ice discharge, possibly leading to misguided conclusions on the glacier mass balance (*Fricker et al.*, 2009).

By sensing tidal flexure, satellite repeat pass InSAR is able to map the grounding line at a precision of 20-50 m (*Rignot*, 1996, 1998), about 2 orders of magnitude better than other techniques. InSAR is now widely used to derive snapshot maps of the grounding line location, and to monitor its migration (*Gray et al.*, 2002; *Rignot et al.*, 2011b; *Park et al.*, 2013; *Rignot et al.*, 2014). In this chapter, I present the grounding line migration of Totten Glacier from year 1996 to 2013, derived by satellite repeat pass InSAR.

4.1   Principles of grounding line detection by InSAR

The ice moves up and down with oceanic tides on the floating ice shelf. This vertical motion complicates the motion signal observed by repeat-pass InSAR. A revised form of Equation 3.2 considering the tidal displacements is presented below:

$$\Delta\phi_d = \frac{4\pi}{\lambda}\delta T(v_x \sin\theta - v_z \cos\theta) + \frac{4\pi}{\lambda}(z_1 - z_2)\cos\theta \tag{4.1}$$

where z_1 and z_2 are tidal heights of the two acquisitions. Note that Equation 4.1 corresponds to flattened and topography-removed interferograms where the only signal in the interferometric phase is the ice motion. Consider two interferograms $i1$ and $i2$ from the same orbit:

$$\begin{cases} \Delta\phi_{i1} = \dfrac{4\pi}{\lambda}\delta T_{i1}(v_x\sin\theta - v_z\cos\theta) + \dfrac{4\pi}{\lambda}(z_{i1,1} - z_{i1,2})\cos\theta \\[2mm] \Delta\phi_{i2} = \dfrac{4\pi}{\lambda}\delta T_{i2}(v_x\sin\theta - v_z\cos\theta) + \dfrac{4\pi}{\lambda}(z_{i2,1} - z_{i2,2})\cos\theta \end{cases} \tag{4.2}$$

The tidal motion can be isolated by assuming v_x and v_z do not change during the two time periods δT_{i1} and δT_{i2}, i.e., the ice flow is steady. This assumption is true for most Antarctic glaciers where basal hydrology does not play a major role in the ice dynamics. Combining the two equations in 4.2 by differencing the two interferograms:

$$\Delta\phi_{i1}\delta T_{i2} - \Delta\phi_{i2}\delta T_{i1} = \frac{4\pi}{\lambda}[\delta T_{i2}(z_{i1,1} - z_{i1,2}) - \delta T_{i1}(z_{i2,1} - z_{i2,2})]\cos\theta \tag{4.3}$$

The differential interferometric phase is now solely dependent on the tidal motion. Figure 4.2 is a sample differential interferogram showing the grounding zone of Petermann Glacier in Greenland (*Rignot et al.*, 2011b). Each fringe, represented by a cycle of colors from blue to yellow, red and back to blue, denotes a phase shift of 2π. Therefore, the differential interferogram can be interpreted as a contour map of tidal displacements, with the dense fringe pattern at the flexure zone. Ideally, there would be no fringe on grounded ice given that the ice motion is perfectly canceled out and the topography is fully removed. However, the steady motion assumption would break down if the glacier speed is changing and the temporal separation between the interferograms is too large. In addition, the surface elevation map of the Antarctic ice sheet is not perfect everywhere, and many coastal areas are experiencing elevation change. All these factors will contribute to residual phase shift on grouded ice in practice, which complicates grounding line mapping. Another potential issue is interferogram scaling. As described in Equation 4.3, the two interferograms need to be scaled if δT_{i1} and δT_{i2} are different. The unwrapped nature of the interferograms requires the scaling factor to be integers, meaning the number of fringes will increase by n-fold for a scaling factor of n. The scaling could result in very narrow or even unresolvable fringe patterns. One common
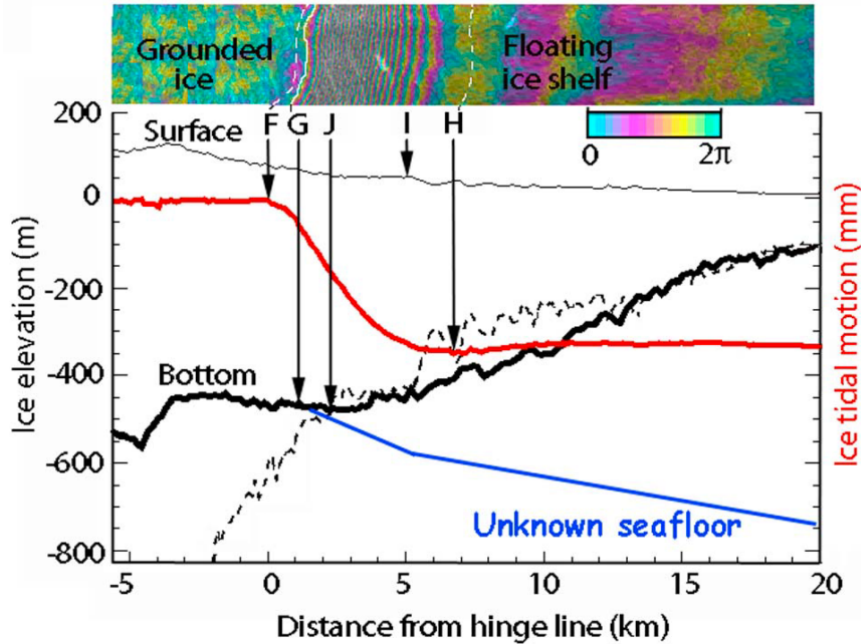
al

Figure 4.2: Grounding zone of Peretermann Glacier, Greenland. Ice flows from left to right. F is the landward limit of tidal flexure, G is the grounding line, J is most landward hydrostatic point, I is the surface slope break point, H is the seaward limit of the flexure zone. Surface elevation (thin blank line) is from laser altimetry, bed elevation (thick black line) is from radio echo sounding, hydrostatic ice bottom elevation (dashed black line) is calculated from the surface profile. Tidal flexure (thick red line) is derived from ERS-1 DInSAR, with the corresponding differential interferogram on top. This figure is from *Rignot et al.* (2011b).

way to avoid such high fringe rates is to unwrap one of the interferograms before the scaling. Unwrapped phases are continuous so that fractional scaling factors can be applied. However, phase unwrapping is not always easy to perform, especially across regions with high strain rates and low coherence such as shear margins.

According to Equation 4.3, the tidal displacements can be calculated to millimeter to centimeter precision. These measurements help constrain and validate the global tide models near the ice sheets where *in situ* observations are sparse.

	sensor	λ (cm)	orbit	date	$B_\perp$ (m)	h_{tide} (cm)
GL	ERS-1/2	5.6	24868	Apr 17 1996	-53.5	10.8
			5195	Apr 18 1996		2.2
			24367	Mar 13 1996	-185.8	-41.0
			4694	Mar 14 1996		-36.2
	CSK	3.125	27683	Dec 07 2013	334.6	-43.2
			16737	Dec 10 2013		0.753
			32660	Dec 22 2013	58.8	-37.2
			16974	Dec 26 2013		-13.5
DEM	TDX	3.1	21	Jun 02 2013	94.4	
			112	Jun 30 2013	69.4	
			163a	Jun 22 2013	235.1	
			163b	Aug 05 2013	195.2	

Table 4.1: InSAR satellite data used to map the grounding line of Totten Glacier: sensor name, radar wavelength λ in centimeters, satellite orbit number, time of acquisition, perpendicular baseline $B_\perp$, and ocean tidal amplitude h_{tide} from the FES 2012 tidal model (*Carrère et al.*, 2012).

4.2 Grounding line mapping of Totten Glacier

4.2.1 Data and methods

To detect the grounding line of Totten Glacier, differential interferograms are constructed using ERS-1/2 data in 1996 and the Agenzia Spaziale Italiana (ASI) COSMO-SkyMed (CSK) constellation in 2013 following the approach in *Rignot et al.* (2011a). Surface topography is removed from the interferograms using the 20-m spacing TanDEM-X surface elevation map (see section 2.1.2). The two CSK interferograms are separated by 3 and 4 days, respectively. The 4-day interferogram is unwrapped and scaled to 3 days to be combined with the 3-day second interferogram. Good signal coherence is challenging to obtain on Totten Glacier due to katabatic winds and large snow accumulation (*Goodwin*, 1990). CSK radar signals at X-band (3.1 cm wavelength) are affected by this surface weathering. In addition, the shear margins of Totten Glacier along Law Dome experience high strain rates, which generates phase aliasing and makes it difficult to unwrap the interferometric phase across the margins.

The perpendicular baseline of the CSK differential interferogram is 333 m, which corresponds to an altitude of ambiguity (or change in elevation causing a full phase cycle, Equation 2.5) of 26 m. In order to retrieve the ice vertical motion associated with tides, it is therefore critical to remove the surface topography signal from a high-quality, high-resolution digital elevation map (DEM). The BEDMAP-2 topography (*Fretwell et al.*, 2013) is not of sufficient quality for this exercise (Figure S6), while the TanDEM-X DEM yields only small residual motion signals (Figure 4.3).

Due to limited CSK data acquisitions in this sector, the mapping of grounding line is limited to 20% of the entire grounding zone of Totten (Figure 2b). This portion of the grounding line however carries 70% of the total ice discharge into the ocean and coincides with the area of most rapid thinning reported by altimeters (Figure 2.13). This area is therefore key to monitor glacier changes.

A second differential interferogram is formed using ERS-1/2 1996 data (*Rignot*, 2002) re-processed using a longer track with the following improvements: (1) the precision baseline is calculated using OIB laser altimetry data (*Blankenship et al.*, 2012, updated 2013) instead of BEDMAP-1 (*Bamber and Bindschadler*, 1997); (2) surface topography is removed using the TanDEM-X DEM, and (3) we apply a small correction (0.5% of the line-of-sight ice velocity) to remove phase residuals caused by subtle changes in ice motion during the 35-day period between consecutive ERS-1/2 pairs. Accurate baseline information and ice motion correction improve the quality of the differential interferogram, i.e. data noise is reduced, and the transition boundary between floating and grounded ice is more easily detected. To map the grounding line, we multiply the phase signal by a factor of 4 to enhance the transition boundary, follow iso-contours of tidal-induced displacements, and quantify the error in grounding line position across the glacier width. On average, the mapping precision is 1-2 pixels in the CSK differential interferogram and 2-3 pixels in the ERS-1/2 differential interferogram, which translates into a grounding line mapping error of less than 120 m.
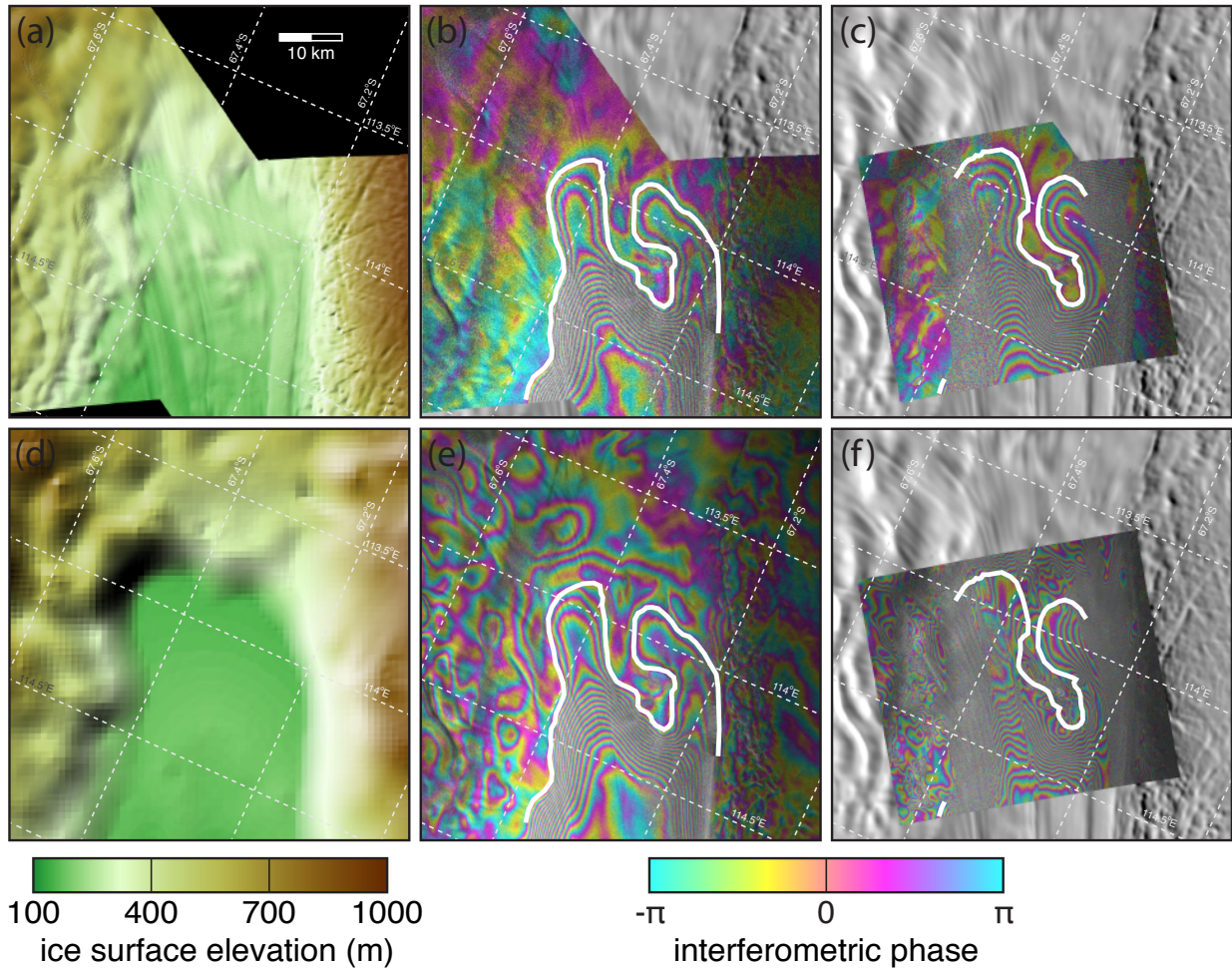
Figure 4.3: Totten Glacier, East Antarctica surface topography from (a) TanDEM-X DEM (20 m spacing) and (d) BEDMAP2 (1 km spacing) (*Fretwell et al.*, 2013), and differential SAR interferograms (DSIs) of (b, e) 1996 ERS-1/2 data using (a, d) and (c, f) 2013 COSMO-Skymed (CSK) data using (a, d) for topography correction. The white solid lines are the grounding line mapped from DSI. The comparison shows that the topography correction is critical to clean up the DSI and to map the grounding line precisely. With a 1 km resolution, BEDMAP2 is not of sufficient quality to remove the topographic signal, especially for the X-band CSK DSI with a long baseline.

To compare the grounding line position with tidal forcing, we use the FES 2012 global tidal model (*Carrère et al.*, 2012) to simulate the geocentric tidal heights at the time of acquisition of each SAR scene (Table 1). The model simulation is carried out at 66.5°S, 117°E. The calculated tidal amplitudes vary from -64 cm to 82 cm. We adopt a hydrostatic balance relationship from *Park et al.* (2013) and *Tsai and Gudmundsson* (2015) to quantify the grounding line migration associated with both oceanic tides and ice thinning:

$$
\dot{h} - \left(\frac{\rho_{sw}}{\rho_i}\right)\dot{z} =
\begin{cases}
\left[\alpha - \beta\left(1 - \frac{\rho_{sw}}{\rho_i}\right)\right]\dot{x}, & \text{if } \dot{x} < 0 \\[2em]
\left[\left(\frac{\rho_i}{\rho_{sw} - \rho_i}\right)\alpha - \beta\right]\dot{x}, & \text{if } \dot{x} > 0
\end{cases}
\tag{4.4}
$$

where $\dot{z}$ is the change in tidal amplitude, $\dot{x}$ is the grounding line migration rate, $\dot{h}$ is the change in ice thickness, α and β are the slopes of the ice surface and glacier bed, measured positive when elevation decreases down glacier. During the time interval of the ERS-1/2 and CSK data, we calculate a maximum grounding line migration of 200 m along the southern lobe and 50 m along the northern lobe, which is 4 to 12 times less than the grounding line migration measured between 1996 and 2013. Ice thinning over one tidal cycle is negligible.

4.2.2 The grounding line pattern of Totten Glacier

The grounding line of TG exhibits a complex and unusual pattern with two lobes extending more than 15 km inland across the 25 km glacier width of the fast-flowing core of TG (Figure 4.4). The tidal flexure zone along these two lobes is extraordinarily long with only a few fringes reaching far upstream. This unique pattern suggests that the tidal flexing does not reach full amplitude on these two lobes so that this region is grounded at low tides. Therefore, the bedrock must be of flat slopes with ocean water intrusion beneath the lobes at high tides. The mapping from this study is limited by the coverage of TanDEM-X DEM.
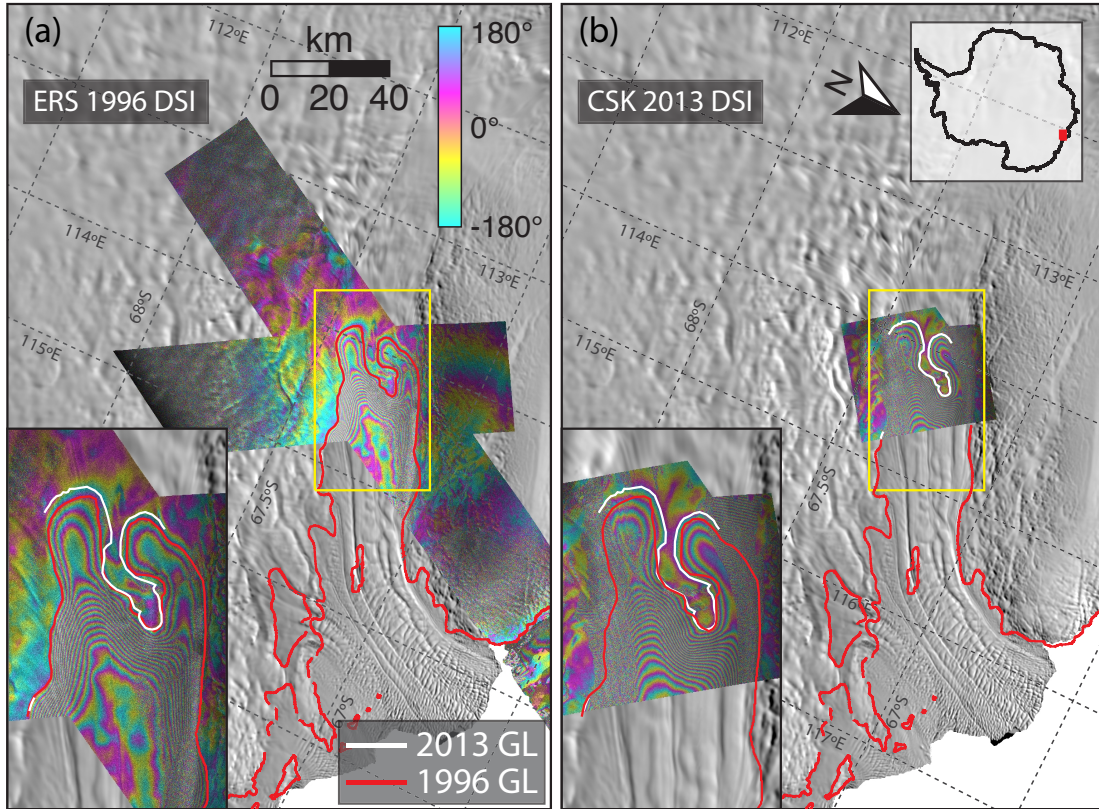
Figure 4.4: Differential SAR interferograms (DSIs) of Totten Glacier from (a) 1996 ERS-1/2 and (b) 2013 COSMO-Skymed (CSK) data overlaid on a MODIS mosaic of Antarctica (*Scambos et al.*, 2007). The fringe pattern is caused by vertical tidal motion between data acquisitions. Grounding line in 1996 is red, and 2013 is white. Each fringe color coded from blue to yellow, purple and blue again is a full cycle in interferometric phase or 360 degrees.

Rignot (2002) presented a more complete mapping of the grounding line extending all the way to the ice front. According to his mapping, there is an ice rumple fully grounded in the middle of the ice shelf, 40 km downstream the grounding line. Airborne altimetry data (*Blankenship et al.*, 2012, updated 2013) show the ice rumple is grounded more than 100 m above buoyancy. Unlike an ice rise, no apparent speed decrease has been observed on the ice rumple.

4.3   Grounding line retreat of Totten Glacier

The comparison between 1996 and 2013 grounding line positions (Figure 4.4) reveals a widespread retreat of the grounding line of up to 3 km. The retreat is not uniform. The southern lobe retreated 1.1-2.6±0.1 km, while the northern lobe retreated 0.4-1.3±0.1 km. These values are significantly larger than those expected from changes in oceanic tides mentioned earlier. The shape of the grounding line also changed. The two lobes are wider and more closely spaced in 2013 than in 1996. The grounded region or ice island between the two lobes decreased in area between 1996 and 2013. This indicates thinning and ungrounding of the island.

The tidal displacement measured from the DSIs is +0.46 m for ERS-1/2 1996 differential interferogram and -0.40 m for CSK in 2013. FES 2012 tidal model correctly predicts the sign of the tidal motion but underestimates its amplitude by a factor of two (see Table 4.1). This may be due to uncertainties in the shape of the sub-ice-shelf cavity in the tidal model. If we assume that both the phase and magnitude of the FES 2012 are correct, we can calculate using Equation 4.4 that the grounding line retreat is underestimated by 30 m due to higher tidal uplift in the 1996 interferogram compared to the one in 2013. The maximum grounding line migration due to tides is 60 m if we multiply the FES 2012 tidal magnitudes by a factor of two to match the observations.

Applying Equation 4.4 to TanDEM-X DEM (see section 2.1.2) and MC bed topography (see section 2.2.2), we calculate the thinning rate along each lobe that would explain the observed grounding line retreat in 1996-2013. We find that the ice thinning must average 0.7 m/yr in order to match the observed retreat. 1% error in the slope calculation using OIB data and ~10% error in the grounding line retreat together contribute to up to 12.5% error, or 0.09 m/yr, in the thinning result. This 0.7±0.09 m thinning magnitude is consistent with the values reported in Table 2.1 for the same time period.

Equation 4.4 is also applied to estimate future grounding line retreat of Totten Glacier. With knowledge of local surface and bed slopes (α and β), one can associate the rate of retreat ($\dot{x}$) to the rate of ice thickness change ($\dot{h}$) for any grounded point. Here the surface and bed slopes are calculated from the TanDEM-X DEM (Figure 2.4) and the MC topography (Figure 2.10) to calculate the surface and bed slopes, respectively.

The grounding line is firstly smoothed to a 190 km long curve with a 90 m along-track resolution. We assume the grounding line retreats along the smallest gradient of hydrostatic potential and use the hydrostatic potential map (Figure 2.11) to determine the direction of the retreat at each point. The local surface and bed slopes (α and β)are then calculated in these directions over a 2.6 km scale. The 2.6 km scale is chosen because it approximately equals to one ice thickness so that the impact of high frequency noise in the data is reduced. We then calculate $\dot{x}/\dot{h}$ at each point using Equation 4.4. Then we derive the new grounding line position after 1 m ice thinning by $\Delta x =$ -1 m $\times \dot{x}/\dot{h}$. This process is iterated 10 times to get the projected grounding line position of 10 m thinning (the dark curve in Figure)

In between the two lobes, there is an narrow ice island. At the junction between floating ice and grounded ice, we only use points on grounded ice to calculate surface slopes and bed slopes. Closest to the grounding line, our slopes are calculated with a 1.6 km scale instead of 2.6 km scale.

Equation 4.4 only applies to cases in which hydrostatic potential increases inland, i.e. $\alpha \geq \beta \cdot (\rho_i - \rho_{sw})/\rho_i$. In that case, we increase our length scale until compatible with Equation 4.4.

The retreat rate is largest (480-720 m per 1 m ice thinning) along the southern lobe due to its low hydrostatic potential gradient, and decreases to 20-70 m per 1 m thinning along the northern lobe due to its steeper topography. The retreat rate decreases to less than 1 m per 1 m ice thinning towards the sides. As the grounding line retreats, the southern lobe starts

to float first. The grounded region in between the two lobes shrinks dramatically to become an isolated pinning point.

For verification, we repeat the same calculation along OIB profiles AA' and BB' (grey boxes in Figure 3) where high resolution, direct observational data are available. The retreat rates along AA' and BB' are 680 m and 27 m per 1 m ice thinning, respectively, which falls in the range of those calculated using the MC and TDX topographies. We note that this retreat rate is larger than that observed between 1996 and 2013, i.e. the region upstream of the 2013 grounding line is more prone to un-grounding than the region that ungrounded in 1996-2013. If thinning persists, we therefore project a faster retreat of the grounding line in years to come.

4.4 Summary

An InSAR-derived grounding line map of Totten Glacier shows an unusual pattern with two prominent lobes occupying the entire 25 km wide trough of the main ice stream, extending more than 15 km from the free ice shelf. Differential interferograms show that tidal motion on the lobes is less than that on the free ice shelf, which means that they are grounded at low tides.

Comparing the grounding line positions mapped in 1996 and 2013 suggests Totten Glacier had retreated 1-3±0.2 km during the 17 intervening years. The retreat is assymetric along the two lobes but both suggesting an average thinning of 0.7 m/yr. This is consistent with altimetry results. The shape of the grounding line also changed during this time period. The two lobes become wide and tends to connect to each other in 2013 compared to 1996. Hydrostatic analysis shows that if the thinning persists, the retreat will propagate fast beyond the southern lobe and unground the ice plain with a flat basal topography, while the northern

lobe will slowly climb up a steep bed, yielding a more stable grounding line.

Chapter 5

Mass balance of Totten Glacier

In this chapter, the three major methods to estimate glacier mass balance are reviewed. All the observational records for Totten Glacier are then synthesized to estimate the mass budget of the glacier and to examine its evolution over time.

5.1 Methods of estimating ice sheet mass balance

5.1.1 Mass budget method

The mass budget method (*Rignot and Thomas*, 2002), also referred to as the flux component method (*Allison et al.*, 2009) or the flux-gate method (*Cuffey and Paterson*, 2010), estimates the ice sheet mass balance by comparing the sum of mass inputs and the sum of output fluxes. This method can be applied to either individual drainage basins or the entire ice sheet.

The major mass input for the Antarctic ice sheet is snowfall accumulation at the surface. While direct measurements of accumulation can be obtained from *in situ* observations, available data are sparse and only provide short temporal records. Past meteorological informa-

tion for longer time scales can be retrieved from ice core stratigraphy, but the spatial coverage is limited. Recently, numerical models of regional atmospheric circulation have provided simulated surface mass balance (SMB) of ice sheets including solid precipitation, sublimation, snowmelt, firn densification and runoff (*van de Berg et al.*, 2006; *Ligtenberg et al.*, 2011; *Lenaerts et al.*, 2012). These simulations are driven by atmospheric dynamics and ice sheet surface processes and forced by weather forcasting reanalysis data (*van de Berg et al.*, 2006). The model outputs are found in good agreement with observations and considered a reliable estimate for input flux in mass budget calculations of Antarctica, especially in coastal regions (*van Wessem et al.*, 2014).

In most areas of coastal Antarctica, surface temperature stays below freezing point all year round. Therefore, the dominant flux of mass output for the grounded part of the ice sheet is ice discharge. Grounding line is often used as the flux gate to calculate the discharge for three reasons. First, all the ice flowing across the grounding line ends up in the ocean. The grounding line mass flux can be directly used to estimate sea level contribution. Second, all the ice shelf processes are excluded from the grounding line flux, which significantly simplifies the calculation. Lastly, the ice is close to hydrostatic equilibrium at the grounding line (see Figure 4.1), which allows for ice thickness estimation from the surface elevation. In practice, the inferred ice thickness is easier to use in mass flux calculation compared to measured ice thickness because no firn correction is needed. Ice discharge is the path integral of the ice flux normal to the grounding line. Caution should be taken when calculating the grounding line flux, inaccurate grounding line positions could lead to large error in the flux calculation (*Fricker et al.*, 2009).

The difference between the input and output mass flux is the mass balance of the ice sheet. Since the imbalance is usually just a small fraction of the input and output fluxes, it is difficult to achieve accurate mass balance estimate for a big ice sheet using the mass budget method. However, the mass budget methods estimate SMB and ice discharge independently. The

partitioning between SMB and ice discharge shows whether the change in mass is caused by SMB or ice dynamics. This information is therefore of particular importance to understand the evolution of glacier mass balance.

5.1.2 Altimetric method

Satellite altimetry monitors the elevation change of the ice sheets over time. The volume variations of the ice sheets can be inferred from the elevation change if the effects of firn compaction and post-glacial rebound are small enough. This method cannot distinguish between different processes driving the mass change, but is capable of providing continuous time series of the mass balance. Over decadal time scales, problems arise when applying the altimetric method. Firstly, the penetration depth of radar altimeters is a function of density of the firn layer, which is also a major source of surface elevation change in short time scales. An independent assessment of snowfall accumulation and firn densification is therefore necessary to convert the altimetry signals into mass change. Secondly, the accumulated vertical motion due to post-glacial rebound over decades complicates the elevation change measurements. This glacial isostatic adjustment can be estimated by numerical models based on ice and lithosphere dynamics (*Peltier*, 2004), or extracted from altimetry and satellite gravity (*Riva et al.*, 2009). However, the glacial isostatic adjustment is large in Antarctica and still remains poorly constrained.

5.1.3 Gravitational method

As introduced in section 1.3.4, the GRACE mission is capable of measuring mass change of the ice sheets by detecting changes in the Earth's gravity field. GRACE provides the mass change time series of polar ice sheets on a monthly basis since 2002. It is a useful tool to calibrate and verify other estimates. Similar to the altimetric method, GRACE

measurements need to be corrected for glacial isostatic adjustments. One major limitation of the gravitational method is its low spatial resolution. The global gravity field delivered by GRACE is expressed as the sum of a spherical harmonic expansion, or Stokes coefficients, with high noise in the spatial domain. Strong smoothing with more than 600 km spatial wavelength is required to filter out the noise (*Chen*, 2005). *Jacob et al.* (2012) proposed a mascon approach to achieve a higher spatial resolution for GRACE data. The spatial domain is first divided into small mascons, for each mascon, the Stokes coefficients are calculated and temporal trends are extracted. The mascon approach allows for regional analysis of the mass change since the mascons can be distributed with prior ground cover knowledge. However, the spatial resolution is still very poor compared to the other two methods.

5.2 Mass balance of Totten Glacier

5.2.1 Surface mass balance

In this study, surface mass balance (SMB) of Totten Glacier is estimated using the most recent compilation of RACMO2.3 (*van Wessem et al.*, 2014) (Figure 5.1). The SMB values are integrated over the drainage basin (*Rignot et al.*, 2013) to compare with ice discharge. The uncertainty in SMB in East Antarctica has been estimated to be 4-10% depending on elevation (*van Wessem et al.*, 2014). We calculate an elevation-weighted average error of 5.3% over the entire drainage basin of Totten Glacier. Surface mass balance on Totten Glacier shows large temporal variations up to 100% from year to year with an average of 65 Gt/yr between 1979-2015 (Figure 5.1). We calculate a reference SMB which is the long-term average SMB for the time period 1979-2014. The reference SMB is used to represent the balance flow because ice core records from Law Dome show no trends in the snowfall accumulation in this region during the past 2000 years (*van Ommen and Morgan*, 2010;
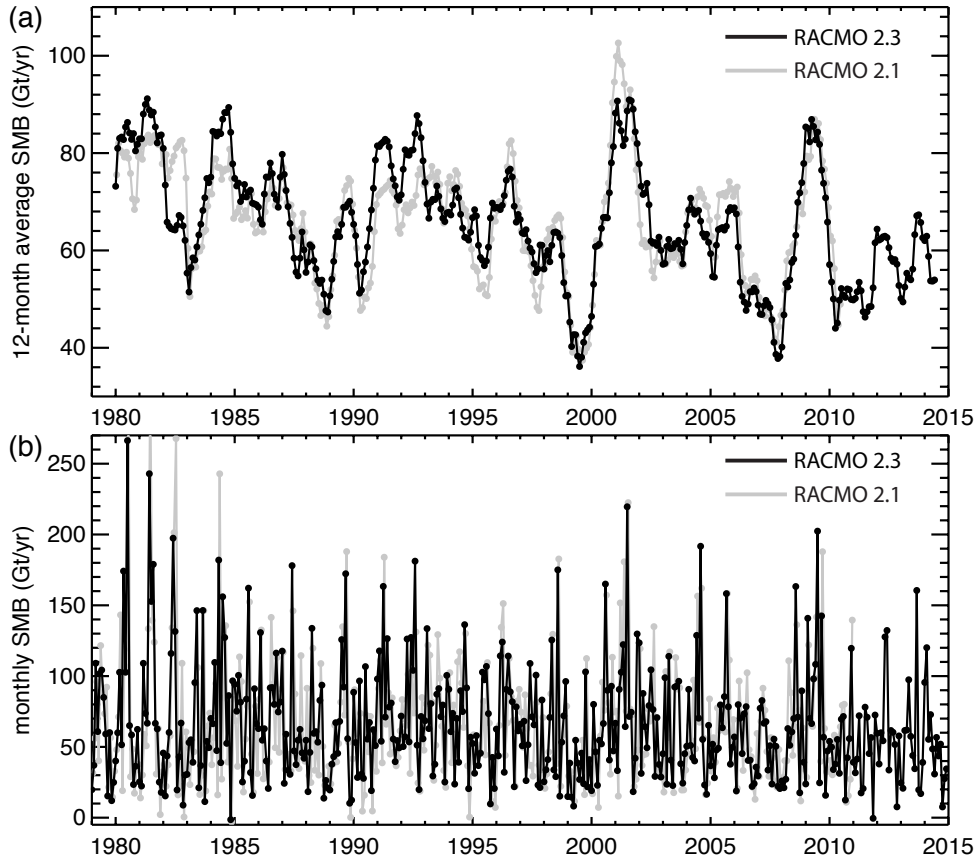
Figure 5.1: Surface mass balance of Totten Glacier from RACMO2. (a) is the smoothed annual values using a 12-month running filter on the original monthly data (b). The latest solution RACMO2.3 (*van Wessem et al.*, 2014) is plotted in black and the most widely used version RACMO2.1 (*Lenaerts et al.*, 2012) is plotted in grey.

Roberts et al., 2015). The surface temperature is also stable during the observational period at Casey Station near Totten Glacier (Figure 5.2) (*Turner et al.*, 2004). We compare the calculated ice discharge (section 5.2.2) with the reference SMB to obtain the mass balance of the glacier.

5.2.2 Ice discharge

Ice velocities (Figure 3.4) are combined with ice thickness from BEDMAP-2 (*Fretwell et al.*, 2013), with strong constraints from Operation IceBridge (OIB) data collected in 2009-2012
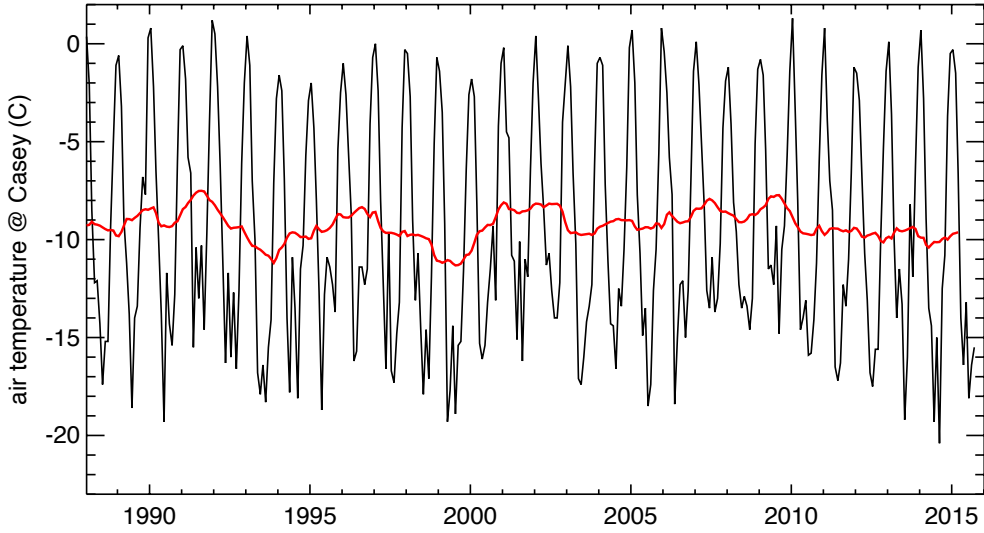
Figure 5.2: Air temperature in degree Cesius at Casey Station, Law Dome, East Antarctica. The monthly data (in black) is smoothed (in red) using a 12-month running filter. Data is from *Turner et al.* (2004).

year	time span	$D_{CC'}$	$F_{DD'}$	ΔSMB	$D_{DD'}$
1989	03/28/1989-11/08/1989	69.3±5.6*	64.3±5.0*	6.7	71.0±5.0*
1996	02/13/1996-05/29/1996	70.5±5.0	64.0±7.4	6.7	70.7±7.4
2000	09/07/2000-11/13/2000	64.6±3.6	58.3±2.4	6.7	65.0±2.4
2001	01/06/2000-11/27/2002	66.4±5.5*	61.6±4.9*	6.7	68.3±4.9*
2005	09/07/2005-10/12/2005	70.6±5.5*	63.4±5.0*	6.7	70.1±5.0*
2006	05/20/2006-08/13/2006	73.3±3.2	67.3±3.8	6.7	74.0±3.8
2007	09/08/2007-01/14/2008	74.5±3.1	65.7±3.8	6.7	72.4±3.8
2008	09/10/2008-01/24/2009	72.5±3.0	66.7±3.8	6.7	73.4±3.8
2009	09/13/2009-01/19/2010	70.5±3.0	65.4±3.8	6.7	72.1±3.8
2010	09/28/2010-01/30/2011	72.5±3.1	65.9±3.9	6.7	72.6±3.9
2011	06/10/2011-08/12/2011	69.2±2.7	65.1±2.0	6.7	71.8±2.0
2013	06/13/2013-01/20/2014	71.9±3.0	65.3±2.3	6.7	72.0±2.3
2015	02/22/2015-03/18/2015	72.0±5.5*	65.6±5.0*	6.7	72.3±5.0*

Table 5.1: Ice discharge in Gt/yr at the flux gate CC' ($D_{CC'}$) and DD' ($D_{DD'}$) of Totten Glacier, East Antarctica, from 1989 to 2015. See Figure 1 for locations of CC' and DD'. CC' is the grouding line (Figure 3.5, yellow line), DD' is OIB ground tracks (*Blankenship et al.*, 2011, updated 2013) (Figure 3.5, orange line). $D_{DD'}$ is corrected for suface mass balance (SMB) in between CC' and DD' as $D_{DD'} = F_{DD'} + \Delta$SMB, where $F_{DD'}$ is the ice flux across DD' and ΔSMB is the area integral of SMB between CC' and DD'. SMB values are from RACMO2.3 (*van Wessem et al.*, 2014). Flux value with a star superscript indicates that this value is estimated by scaling the flux refereced to year 2007.

(*Blankenship et al.*, 2011, updated 2013), to calculate the ice flux following *Mouginot et al.* (2014b). The ice flux is estimated along the OIB ice thickness profiles (Figure 3.5, orange line) and also along the interferometrically-derived grounding line (Figure 3.5 , yellow line). We convert the fluxes across the OIB flux gate to equivalent grounding line fluxes by adding the average SMB between the two gates, 6.3 Gt/yr. When velocity measurements are patchy, e.g. in 1989, 2001, 2005 and 2015, we calculate a scaling factor by comparing the grounding line ice velocity to the most complete year (2007), then use it to estimate the ice flux. We quantify the errors in ice discharge using multiple flux gates following *Mouginot et al.* (2014b). Temporal changes in ice thickness are not included in the calculation because they are very small (1 m/yr) compared to the glacier thickness (2 km) and also not well quantified (Table 2.1, Figure 3.6). SMB and ice discharge are integrated over time to calculate the cumulative fluxes. The cumulative fluxes are then subtracted from one another to derive the cumulative mass anomaly. The mean mass balance and change in mass balance are computed using a weighted least squares regression on the cumulative mass anomaly following *Sutterley et al.* (2014), we then use the Akaike Information Criterion for finite sample sizes (AIC$_c$) (*Burnham and Anderson*, 2002) to select the regression model that best fits the cumulative mass anomaly.

5.2.3   Mass balance

The ice discharge time series (Figure 5.3) is consistent with the velocity change at the grounding line at the main trunk (Figure 3.6). The discharge is higher than the reference SMB for most of the time during 1989 to 2015, indicating that the glacier has been flowing above equilibrium conditions for the past 26 years. The only exception is year 2000, when the glacier was flowing at the minimum speed in our time series. The interannual mass balance of the glacier is significantly modulated by large variations of SMB. On average, we estimate a mass loss of 6.8±2.2 Gt/yr (1σ). The cumulative mass anomaly shows a
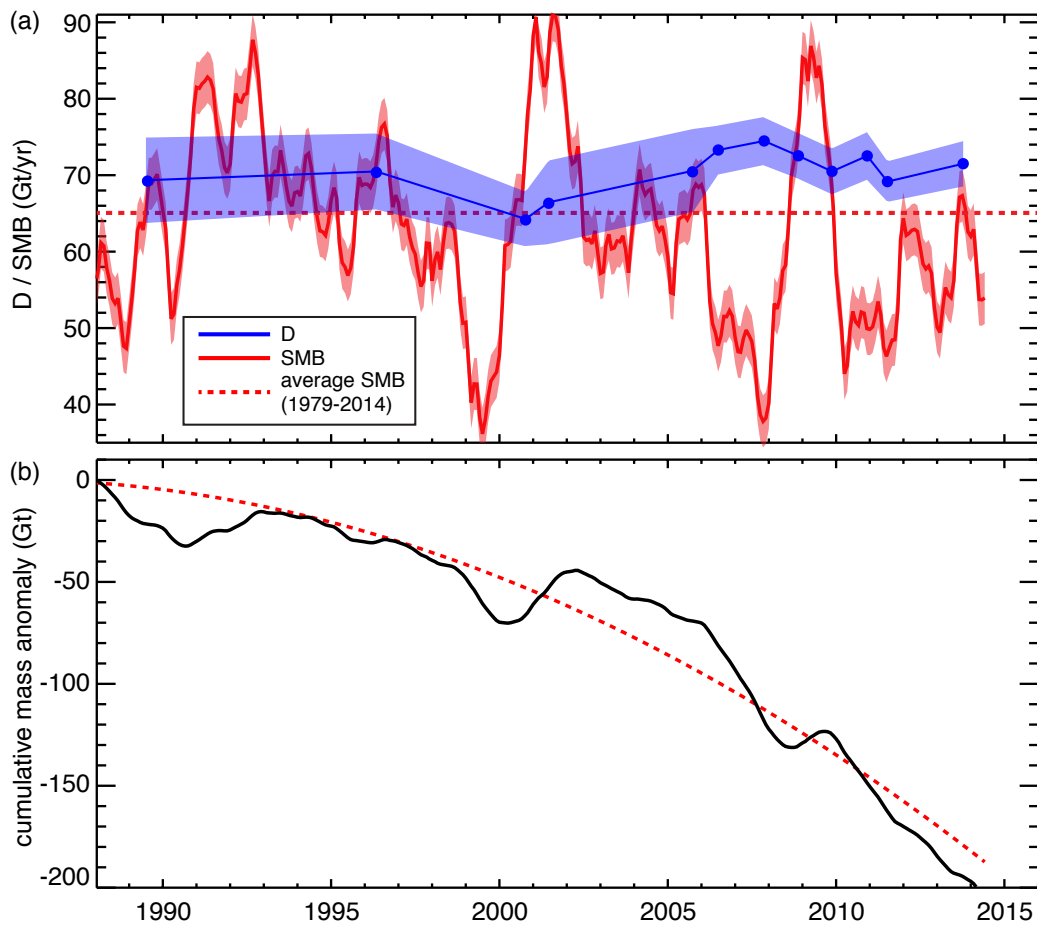
Figure 5.3: Time series of (a) surface mass balance (SMB) and ice discharge (D), and (b) cumulative mass anomaly on Totten Glacier. The SMB in (a) is the moving average of monthly data over a 12-month window (Figure 5.1a). The red dashed line in (b) is a quadratic fitting. The quadratic model is selected based on the AIC_c criterion.

quadratic decreasing trend (Figure 3d) with an acceleraion of -0.55±0.27 Gt/yr^2. 80% of the acceleration signal comes from the decrease of SMB in the recent years, therefore may not be indicative of a long term trend.

When comparing with the reference SMB, we find the glacier was already flowing beyond equilibrium conditions in 1989. Although annual mass balance is strongly affected by the large fluctuations in SMB, the overall glacier mass balance is negative with high confidence. This conclusion is supported by multiple lines of evidence from GRACE (*Velicogna and Wahr*, 2013; *Velicogna et al.*, 2014), mass budget estimates (*Rignot et al.*, 2008) and many satellite altimetry studies mentioned earlier. The estimated mass loss of 6.8±2.2 Gt/yr, or 10% of the total ice discharge, is broadly consistent with previous studies (e.g. 4.6±0.5 Gt/yr (*Shepherd and Wingham*, 2007), 10±3 Gt/yr (*McMillan et al.*, 2014)). This imbalance is small compared to glaciers in the Amundsen Sea sector in West Antarctica where the mass loss ranges from 30% to 40% (*Sutterley et al.*, 2014; *Mouginot et al.*, 2014b). But future monitoring of the dynamic changes on Totten Glacier is necessary and critical considering its large sea level rise equivalent and potential vulnerability.

The dynamic change most likely has an oceanic origin, similar to other fast changing sectors in Antarctica like Amundsen Sea Embayment. Field oceanographic data revealed the presence of modified Circumpolar Deep Water (mCDW) on the continental shelf near TG (*Bindoff et al.*, 2000; *Williams et al.*, 2011). However, due to persistent sea ice cover, there is no observational records of the temporal variations of mCDW intrusion. The reanalysis temperature record from ECCO2 solution (Figure 3.6c) shows three periods of warming/cooling of the sub-surface water (150-450 m depth) on the continental shelf, corresponding to the acceleration/deceleration periods in our velocity record. However, it is not clear how well the ECCO2 solution replicates the ocean state in this remote sector with few observational data. Observational data about sea floor bathymetry, ocean thermal forcing and ocean circulation in front of Totten Glacier could help improve ocean modeling to confirm the sensitivity of

Totten Glacier to ocean thermal forcing.

To the east of the ice front of TG, grounded icebergs and offshore winds induce persistent coastal polynya formation (*Massom et al.*, 1998; *Tamura et al.*, 2008). Previous ocean modeling studies have proposed that advection of cold, saline polynya water into the ice-shelf cavity could lower the melting rates (*Khazendar et al.*, 2013; *Gwyther et al.*, 2014), possibly slow down the ice flow in a further step. The simulated melt rates from *Gwyther et al.* (2014) show a strong increase in 2004-2007, which could possibly explain the major speed up. During other periods, we do not find any relationship between anomalous melt rates and velocity change. It is not clear if all the observed change is induced by the polynya mechanism. The uncertainty in the model results due to the unknown shape of the sub-ice-shelf cavity also remains a concern when interpreting the results. Many questions still remain on the change in ocean circulation in this region. Further numerical modeling studies are needed to investigate the role of mCDW in the dynamic change of Totten Glacier.

5.3 Summary

Ice discharge of Totten Glacier is calculated using the velocities measured in each year, then compared with a reference surface mass balance (SMB) to assess the mass balance. The result shows that Totten Glacier was already flowing beyond equilibrium conditions in 1989, then slowed down to reach equilibrium in 2000, when ice speed reached a minimum. Its mass balance became more negative after 2000 and stayed stable since then. An acceleration trend has been found in the accumulative mass balance anomaly, with most of the signal coming from the mass balance fluctuation in recent years. On average, Totten Glacier is losing 6.8±2.2 Gt of mass every year during our observation time period, which is consistent with previously reported estimates from altimetry studies.

Chapter 6

Conclusions

6.1 Summary of major results

Totten Glacier in East Antarctica has enormous potential for sea level rise. It has shown signs of dynamic change and potential instability over the past decade. Its remoteness, vastness and harsh surface conditions prohibit systematic monitoring of this glacier using both *in situ* and remote sensing techniques. This dissertation focuses on the evolution of Totten Glacier in the past three decades using a comprehensive observational record derived from a suite of satellites. This study reports changes of Totten Glacier in four different aspects: surface elevation, ice velocity, grounding line position and mass balance.

Surface elevation Comparison of high resolution surface elevation maps from 2011 and 2013 reveals significant surface lowering on Totten Glacier, consistent with altimetry results from previous studies. The spatial pattern of the surface lowering rates is well correlated with ice flow speed. Surface lowering is only observed in regions of fast flow. The higher the flow speed is, the more negative the dh/dt rates are.

Ice velocity Thirteen velocity maps spanning through 1989-2015 show a significant temporal variation of surface velocity on Totten Glacier. The glacier has been flowing above equilibrium in 1989, slowed down by 86 m/yr, or 12% in 2000 to reach balance, and accelerated by 18% in 2007 to remain stable since then. The change in speed is localized in the main ice stream near the grounding line on both grounded and floating ice, but not reflected in the inland portion of the glacier system. The observed acceleration/deceleration periods of ice velocity is consistent with thinning rates reported by satellite altimetry, as well as sub-surface ocean temperatures off the coast from reanalysis data. This correlation is illustrative of high sensitivity of Totten Glacier to oceanic perturbations.

Grounding line position The grounding line postion of Totten Glacier has been mapped using InSAR in 1996 and 2013. The 2013 grounding line has retreated up to 3 km from 1996 position. The retreat is asymetrical along the two-lobe pattern of the grounding line, indicative of an average thinning rate of 0.7 m/yr. The 0.7 m/yr average thinning rate is consistent with altimetry observations.

Mass balance Change in ice discharge is dominated by the velocity change at the grounding line. Comparing to the long term mass balance, Totten Glacier was already flowing above equilibrium in 1989. The discharge decreased during the deceleration period 1989-2000 until the glacier reaches balance in 2000, then increased with the speeding up from 2000 to 2007. While year-to-year mass balance is dominated by large variations in surface mass balance, the mass balance of Totten Glacier is negative with high confidence due to the excessive outflow. The average rate of mass loss is 6.8±2.2 Gt/yr, or 10%, broadly consistent with previous estimates (4.6±0.5 Gt/yr (*Shepherd and Wingham*, 2007), 10±3 Gt/yr (*McMillan et al.*, 2014)).

A concrete picture of dynamic changes of Totten Glacier is emerging from multiple consistent lines of evidence. The reconstructed surface and basal topography provide insights on future evolution of this glacier. A 7 km long by 8 km wide ice plain has been detected immediately

upstream of the southern lobe of Totten's grounding line, where the ice is slightly grounded with a flat surface. The retreat can easily propagate throughout this region with only a modest amount of ice thinning. Hydrostatic analysis shows that the ice plain will be fully ungrounded with the current thinning rate (0.7 m/yr) in 14 years. However, beyond the ice plain, the bed elevation rises for 40 km until it finds retrograde slope again. We conclude that sustained thinning will cause further grounding line retreat, but may not be conducive to a marine ice sheet instability.

6.2   Technical limitations

Totten Glacier sits close to the South Magnetic Pole, therefore experiences strong ionospheric perturbations when detected by SAR. Due to the dispersive nature of the ionosphere, this effect becomes discernible at L band (e.g. ALOS PALSAR) and lower frequencies, as well as C band (e.g. ERS-1/2, RADARSAT-1/2) when the temporal separation is short and displacement signal is small. In this study, strong ionospheric noise appears in the 1996 velocity mapping using ERS-1/2 1-day separation data. In principle, the ionospheric phase delay can be isolated by spliting the radar spectrum and cancelling out the non-dispersive terms (*Rosen et al.*, 2010). This split-spectrum method has proven successful for L-band data. However, ERS-1/2 has a narrow bandwidth and the ionospheric signal is much weaker compared to L band data. It is very difficult to achieve good coherence for the sub-band interferograms. Unfortunately we were not able to correct for the ionospheric pertubation in this study.

A recent study (*Greenbaum et al.*, 2015) indicated possible ocean access to TG on the broad eastern side of its grounding line. It would be of interest to map grounding line retreat in that sector, as well as the ice rumple in the middle of the ice shelf. In practice, the grounding line mapping requires at least two interferometric pairs from the same orbit and appreciable

tidal displacements. Data availability is the biggest limitation. In this study, while the ERS-1/2 1996 data cover the entire ice shelf with a wide swath, the spatial coverage of the final grounding line mapping is limited by TanDEM-X DEM. In 2013, we only have a single frame of COSMO-Skymed data available, covering ∼20% of the grounding line. To the best of our knowledge, there have been no other data acquired so far to complement our mapping. In the future, the mapping may be extended using ALOS PALSAR-2 14-day repeat data or European Sentinel 1a's data on a 12-day repeat cycle.

The statistical error in our TanDEM-X surface elevation mapping is about 3 meters, while the internal error in the TanDEM-X data is only 0.5 m. The major error source in our DEM mapping is the absolute phase. We fit a constant absolute phase using a least square algorithm. However, the absolute phase may vary along the track. This effect is negligible for single frames, but needs to be taken into account for long tracks. We also used the initial baseline information from the satellite's ephemeris data, which may not be accurate enough. Ideally, the precision baseline parameters and the absolute phase should be fitted simultaneously using ground control points using a multi-variate linear fitting. In this study, we did not employ this method because of the lack of ground control points and the bistatic acquisition mode of the TanDEM-X mission. Our dh/dt mapping shows unrealisticly large values on the floating ice shelf due to the crevasses moving with the ice flow. This problem maybe solved by using a lagrangian method to trace the ice motion downstream, and measure the dh/dt on corresponding surface points.

6.3   Future perspectives

The observational record built in this study is far from complete. Significant spatial and temporal gaps still remain in the velocity time series. The record only spans 26 years, which is just a blink on the time scale of ice sheets. The grounding line is only mapped in 1996

and 2013, with no data in between. In 2013, the mapping is limited to only $\sim 20\%$ of the entire grounding line. Considering the high sensitivity of the glacier to oceanic forcings, it would be of great interest to keep monitoring changes in flow speed, grounding line position and elevation of Totten glacier. The observational record can be extended in the future with many ongoing and projected satellite missions including ALOS2 PALSAR2, RADARSAT-2, Sentinel-1a, Landsat-8, NISAR and so on.

Although further confirmation is needed, the observed dynamic change of Totten Glacier is believed to have an oceanic origin. To better understand the link between the glacier and the ocean, detailed knowledge of sea floor bathymetry is critical, both in front of the glacier and underneath the ice shelf. *Greenbaum et al.* (2015) presented a bathymetry map of Totten Glacier inferred from aerogravity data, which shows a transverse ridge located 40 km seaward of the ice front. Due to the presence of the sea floor ridge, *Greenbaum et al.* (2015) argued that the warm ocean water at depth must access the sub-ice-shelf cavity through a subglacial trough connecting the eastern tributary of the glacier. This hypothesis is not compatible with the InSAR grounding line mapping in 1996 (*Rignot*, 2002), nor with our observations in this study: Changes in ice velocity and surface elevation are most pronounced near the grounding line of the main ice stream, not on the eastern tributary. While providing a general picture of the bathymetry, gravity inversion is not able to resolve small-scale details of the topograhy. Our understanding of the sea floor bathymetry in this critical region will be updated and improved by direct observations from research cruises.

The good correlation between ice velocity and sub-surface ocean temperatures provides preliminary insights into the ice-ocean interaction at Totten Glacier. It is still not clear how well the ECCO2 solution replicates the state of the ocean on the continental shelf, especially at such a remote location where sea floor bathymetry is poorly known and few observational data are available. Oceanographic observations are challenging in this region due to dark winters and persistent sea ice cover. Two independent water column sampling near Totten

Glacier have shown intrusion of modified Circumpolar Deep Water (mCDW) onto the continental shelf. There is an urgent need for more complete and comprehensive oceanographic measurements to examine the access and the volume of mCDW to the cavity of Totten Glacier. Detailed modeling analysis is also required to understand local ocean circulation and heat transport. A scientific cruise on the Australian icebreaker Aurora Australis for the first time reached the ice front of Totten and reported the presence of warm water. This discovery may provide further evidence on how ocean melting drives the dynamic change of the glacier. However, no results have been published at the time of writing.

Previous ocean modeling studies (*Khazendar et al.*, 2013; *Gwyther et al.*, 2014) show that the melting rate of Totten Glacier is modulated by local polynya activities. Persistent katabatic winds and the grounded icebergs near the ice front of Totten Glacier cause formation of polynyas with recurring sea ice production. Consistent brine ejection and heat loss due to the sea ice formation generates cold, saline polynya water, which sinks down and mixes with the warm mCDW coming onto the continental shelf. As a result, the water ending up in the sub-ice-shelf cavity is a mixture of the mCDW and the polynya water. In years with active polynyas, more polynya water is advected into the cavity which lowers the ice shelf melting rates, and vice versa. We compared our velocity time series with the simulated melt rates from *Gwyther et al.* (2014). The melt rates show a strong increase in 2004-2007, which could possibly explain the major speed up in our time series. However, we do not find any other relationship between periods of anomalous melt rates and velocity change. Key questions still remain in the mechanism. Firstly, this polynya hypothesis is based on the assumption that there is a persistent supply of mCDW into the ice shelf cavity, which still needs to be confirmed. Secondly, the variability of mCDW is unknown and presumed to be zero in the modeling studies. The uncertainty in the model results due to the unknown shape of the sub-ice-shelf cavity also remains a concern when interpreting the results. It is still unclear whether the observed change is induced by the polynya modulation or the variability of mCDW itself, or a mixture of both. Observed water column profiles show that the thermocline near Totten

Glacier is deeper than normal ($\sim$ 500 m depth) (*Bindoff et al.*, 2000; *Williams et al.*, 2011), which is not well replicated in ocean models. Therefore, it is questionable whether or not the polynya water formed at the surface can influence mCDW 500 m down in the water column. Comprehensive observational records and targeted modeling efforts are necessary to answer these questions.

Just as important as observations, process-based numerical modeling of the ice dynamics are required to assess the sensitivity of Totten Glacier to different types of forcings, and to predict its future evolution under a changing climate. The observational records developed in this study can be used to prescribe and test models. In the other way around, a sensitivity assessment of the glacier can guide future observations.

Bibliography

Alley, R. B., S. Anandakrishnan, T. K. Dupont, B. R. Parizek, and D. Pollard (2007), Effect of Sedimentation on Ice-Sheet Grounding-Line Stability, *Science*, *315*, 1838–1841.

Allison, I., R. B. Alley, H. A. Fricker, R. H. Thomas, and R. C. Warner (2009), Ice sheet mass balance and sea level, *Antarctic Science*, *21*(05), 413.

Anderson, J. B., S. S. Shipp, A. L. Lowe, J. S. Wellner, and A. B. Mosola (2002), The Antarctic Ice Sheet during the Last Glacial Maximum and its subsequent retreat history: A review, *Quaternary Science Reviews*, *21*, 49–70.

Australian Broadcasting Corporation (2015), Antarctica's totten glacier 'melting from below', australian scientists find.

Bamber, J. L., and C. Bentley (1994), A comparison of satellite-altimetry and ice-thickness measurements of the Ross Ice Shelf, Antarctica, *Ann. Glaciol.*, *20*, 357–364.

Bamber, J. L., and R. A. Bindschadler (1997), An improved elevation dataset for climate and ice-sheet modeling: Validation with satellite imagery., *Ann. Glaciol.*, *25*, 439–444.

Bamber, J. L., R. J. Hardy, and I. Joughin (2000a), An analysis of balance velocities over the Greenland ice sheet and comparison with synthetic aperture radar interferometry, *J. Glaciol.*, *46*(152), 67–74.

Bamber, J. L., D. G. Vaughan, and I. Joughin (2000b), Widespread Complex Flow in the Interior of the Antarctic Ice Sheet, *Science*, *287*(5456), 1248–1250.

Bechor, N. B. D., and H. A. Zebker (2006), Measuring two-dimensional movements using a single InSAR pair, *Geophysical Research Letters*, *33*(16).

Bindoff, N. L., M. A. Rosenberg, and M. J. Warner (2000), On the circulation and water masses over the Antarctic continental slope and rise between 80 and 150°E, *Deep-Sea Res. Pt II*, *47*(12-13), 2299–2326.

Bindschadler, R. A. (2002), History of lower Pine Island Glacier, West Antarctica, from Landsat imagery, *J. Glaciol.*, *48*(163), 536–544.

Blankenship, D. D., S. D. Kempf, and D. A. Young (2011, updated 2013), IceBridge HiCARS 1/2 L2 Geolocated Ice Thickness 2009-2012, *NASA DAAC at the NSIDC*.

Blankenship, D. D., S. D. Kempf, and D. A. Young (2012, updated 2013), IceBridge Riegl Laser Altimeter L2 Geolocated Surface Elevation Triplets 2009-2012, *NASA DAAC at the NSIDC.*

Bohlander, J. L., and T. Scambos (2007), Antarctic coastlines and grounding line derived from MODIS Mosaic of Antarctica (MOA), digital media, *NASA DAAC at the NSIDC.*

Burnham, K. P., and D. R. Anderson (2002), *Model Selection and Multimodel Inference*, 2nd ed. ed., Springer, New York.

Carrère, L., F. Lyard, M. Cancet, A. Guillot, and L. Roblou (2012), FES 2012: a new global tidal model taking advantage of nearly 20 years of altimetry, in *Proceedings of 20 years of Altimetry, Venice 2012.*

Chen, J. L. (2005), Spatial sensitivity of the Gravity Recovery and Climate Experiment (GRACE) time-variable gravity observations, *J. Geophys. Res., 110*(B8).

Chen, J. L., C. R. Wilson, D. D. Blankenship, and B. D. Tapley (2009), Accelerated Antarctic ice loss from satellite gravity measurements, *Nature Geosci., 2*(12), 859–862.

Church, J., P. Clark, A. Cazenave, J. Gregory, S. Jevrejeva, A. Levermann, M. Merrifield, G. Milne, R. Nerem, P. Nunn, A. Payne, W. Pfeffer, D. Stammer, and A. Unnikrishnan (2013), *Sea Level Change*, book section 13, p. 11371216, Cambridge University Press, Cambridge, United Kingdom and New York, NY, USA, doi:10.1017/CBO9781107415324. 026.

Clark, P. U., a. M. McCabe, A. C. Mix, and A. J. Weaver (2004), Rapid rise of sea level 19,000 years ago and its global implications, *Science, 304*, 1141–1144.

Cook, A. J., T. Murray, A. Luckman, D. G. Vaughan, and N. E. Barrand (2012), A new 100-m Digital Elevation Model of the Antarctic Peninsula derived from ASTER Global DEM: methods and accuracy assessment, *Earth System Science Data Discussions, 5*(1), 365–403.

Corr, H. F. J., C. S. M. Doake, A. Jenkins, and D. G. Vaughan (2001), Investigations of an "ice plain" in the mouth of Pine Island Glacier, Antarctica, *J. Glaciol., 47*(156), 51–57.

Cuffey, K. M., and W. S. B. Paterson (2010), *The Physics of Glaciers*, 4th ed., Elsevier, Inc., 30 Corporate Drive, Suite 400, Burlington, Maine.

Davis, C. H., Y. Li, J. R. McConnell, M. M. Frey, and E. Hanna (2005), Snowfall-driven growth in East Antarctic ice sheet mitigates recent sea-level rise., *Science (New York, N.Y.), 308*(5730), 1898–1901.

Deschamps, P., N. Durand, E. Bard, B. Hamelin, G. Camoin, A. L. Thomas, G. M. Henderson, J. Okuno, and Y. Yokoyama (2012), Ice-sheet collapse and sea-level rise at the Bølling warming 14,600years ago, *Nature, 483*(7391), 559–564.

DiMarzio, J., A. Brenner, R. Schutz, C. A. Shuman, and H. J. Zwally (2007), GLAS/ICESat 500 m laser altimetry digital elevation model of Antarctica, National Snow and Ice Data Center.

Dupont, T. K., and R. B. Alley (2005), Assessment of the importance of ice-shelf buttressing to ice-sheet flow, *Geophys. Res. Lett.*, *32*(4).

Duque, S., C. Rossi, and T. Fritz (2015), Single-Pass Tomography With Alternating Bistatic TanDEM-X Data, *IEEE Geosci. Remote Sens. Lett.*, *12*(2), 1–5.

Dutton, A., and K. Lambeck (2012), Ice Volume and Sea Level During the Last Interglacial, *Science*, *337*(6091), 216–219.

Egbert, G. D., and S. Y. Erofeeva (2002), Efficient inverse modeling of barotropic ocean tides, *J. Atmos. Ocean. Tech.*, *19*(2), 183–204.

Fahnestock, M. A., T. A. Scambos, and M. J. Klinger (2014), The next step in ice flow measurement from optical imagery: comprehensive mapping of ice sheet flow in Landsat 8 Imagery using spatial frequency filtering, enabled by high radiometric sensitivity, in *AGU Fall Meeting Abstracts*.

Flament, T., and F. Rémy (2012), Dynamic thinning of Antarctic glaciers from along-track repeat radar altimetry, *J. Glaciol.*, *58*(211), 830–840.

Förste, C., S. Bruinsma, F. Flechtner, J. Marty, J. Lemoine, C. Dahle, O. Abrikosov, H. Neumayer, R. Biancale, F. Barthelmes, et al. (2012), A preliminary update of the Direct approach GOCE Processing and a new release of EIGEN-6C, in *AGU Fall Meeting Abstracts*.

Fretwell, P., H. D. Pritchard, D. G. Vaughan, J. L. Bamber, N. E. Barrand, R. Bell, C. Bianchi, R. G. Bingham, D. D. Blankenship, G. Casassa, G. Catania, D. Callens, H. Conway, a. J. Cook, H. F. Corr, D. Damaske, V. Damm, F. Ferraccioli, R. Forsberg, S. Fujita, Y. Gim, P. Gogineni, J. a. Griggs, R. C. Hindmarsh, P. Holmlund, J. W. Holt, R. W. Jacobel, A. Jenkins, W. Jokat, T. Jordan, E. C. King, J. Kohler, W. Krabill, M. Riger-Kusk, K. A. Langley, G. Leitchenkov, C. Leuschen, B. P. Luyendyk, K. Matsuoka, J. Mouginot, F. O. Nitsche, Y. Nogi, O. a. Nost, S. V. Popov, E. Rignot, D. M. Rippin, A. Rivera, J. Roberts, N. Ross, M. J. Siegert, A. M. Smith, D. Steinhage, M. Studinger, B. Sun, B. K. Tinto, B. C. Welch, D. Wilson, D. A. Young, C. Xiangbin, and A. Zirizzotti (2013), Bedmap2: Improved ice bed, surface and thickness datasets for Antarctica, *The Cryosphere*, *7*, 375–393.

Fricker, H. A., and T. Scambos (2009), Connected subglacial lake activity on lower Mercer and Whillans Ice Streams, West Antarctica, 2003-2008, *J. Glaciol.*, *55*(190), 303–315.

Fricker, H. A., I. Allison, M. Craven, G. Hyland, A. Ruddell, N. Young, R. Coleman, M. King, K. Krebs, and S. Popov (2002), Redefinition of the Amery Ice Shelf, East Antarctica, grounding zone, *J. Geophys. Res.*, *107*.

Fricker, H. A., R. Coleman, L. Padman, T. Scambos, J. Bohlander, and K. M. Brunt (2009), Mapping the grounding zone of the Amery Ice Shelf, East Antarctica using InSAR, MODIS and ICESat, *Antarctic Science, 21*.

Glasser, N. F., and T. A. Scambos (2008), A structural glaciological analysis of the 2002 Larsen B ice-shelf collapse, *J. Glaciol., 54*(184), 3–16.

Gogineni, P. (2012), CReSIS:Airborne radar depth sounder data, Greenland, *Center for Remote Sensing of Ice Sheets, The University of Kansas.*

Goldstein, R. M., H. Engelhardt, B. Kamb, and R. M. Frolich (1993), Satellite Radar Interferometry for Monitoring Ice Sheet Motion: Application to an Antarctic Ice Stream, *Science, 262*(5139), 1525–1530.

Goodwin, I. D. (1990), Snow accumulation and surface topography in the katabatic zone of Eastern Wilkes Land, Antarctica, *Antarct. Sci., 2*(3), 235–242.

Gray, L., N. Short, R. Bindschadler, I. Joughin, L. Padman, P. Vornberger, and A. Khananian (2002), RADARSAT interferometry for Antarctic grounding-zone mapping, *Ann. Glaciol., 34*, 269–276.

Greenbaum, J. S., D. D. Blankenship, D. A. Young, T. G. Richter, J. L. Roberts, A. R. A. Aitken, B. Legresy, D. M. Schroeder, R. C. Warner, T. D. van Ommen, and M. J. Siegert (2015), Ocean access to a cavity beneath Totten Glacier in East Antarctica, *Nat. Geosci.*, pp. 294–298.

Gudmundsson, G. H., J. Krug, G. Durand, L. Favier, and O. Gagliardini (2012), The stability of grounding lines on retrograde slopes, *The Cryosphere, 6*(6), 1497–1505.

Gwyther, D. E., B. K. Galton-Fenzi, J. R. Hunter, and J. L. Roberts (2014), Simulated melt rates for the Totten and Dalton ice shelves, *Ocean Sci., 10*, 267–279.

Horwath, M., B. Legrésy, F. Rémy, F. Blarel, and J.-M. Lemoine (2012), Consistent patterns of Antarctic ice sheet interannual variations from ENVISAT radar altimetry and GRACE satellite gravimetry, *Geophys. J. Int., 189*, 863,876.

IPCC (2013), *Climate Change 2013: The Physical Science Basis. Contribution of Working Group I to the Fifth Assessment Report of the Intergovernmental Panel on Climate Change*, 1535 pp., Cambridge University Press, Cambridge, United Kingdom and New York, NY, USA, doi:10.1017/CBO9781107415324.

Jacob, T., J. Wahr, W. T. Pfeffer, and S. Swenson (2012), Recent contributions of glaciers and ice caps to sea level rise, *Nature, 482*(7386), 514–518.

Jacobs, S. S., A. Jenkins, C. F. Giulivi, and P. Dutrieux (2011), Stronger ocean circulation and increased melting under Pine Island Glacier ice shelf, *Nature Geosci., 4*(8), 519–523.

Joughin, I., R. Kwok, and M. Fahnestock (1996), Estimation of ice-sheet motion using satellite radar interferometry: method and error analysis with application to Humboldt Glacier, Greenland, *J. Glaciol., 42*(142), 564–575.

Joughin, I. R., R. Kwok, and M. A. Fahnestock (1998), Interferometric estimation of three-dimensional ice-flow using ascending and descending passes, *IEEE T. Geosci. Remote*, *36*(1), 25–37.

Khazendar, A., M. P. Schodlok, I. Fenty, S. R. M. Ligtenberg, E. Rignot, and M. R. van den Broeke (2013), Observed thinning of Totten Glacier is linked to coastal polynya variability, *Nat. Commun.*, *4*, 2857.

Klinger, M. J., T. A. Scambos, M. A. Fahnestock, and T. M. Haran (2014), Advanced Ice Velocity Mapping Using Landsat 8, in *AGU Fall Meeting Abstracts*.

Kopp, R. E., F. J. Simons, J. X. Mitrovica, A. C. Maloof, and M. Oppenheimer (2009), Probabilistic Assessment of Sea Level During the Last Interglacial Stage, *Nature*, *462*, 863–867.

Kuipers Munneke, P., G. Picard, M. R. Van Den Broeke, J. T. M. Lenaerts, and E. Van Meijgaard (2012), Insignificant change in Antarctic snowmelt volume since 1979, *Geophys. Res. Lett.*, *39*(1), 6–10.

Legresy, B., and F. Remy (1997), Altimetric observations of surface characteristics of the Antarctic ice sheet, *J. Glaciol.*, *43*(144), 1–11.

Lenaerts, J. T. M., M. van den Broeke, W. J. van de Berg, E. van Meijgaard, and P. K. Munneke (2012), A new, high-resolution surface mass balance map of Antarctica (1979-2010) based on regional atmospheric climate modeling, *Geophys. Res. Lett.*, *39*, 1–5.

Li, X., E. Rignot, M. Morlighem, J. Mouginot, and B. Scheuchl (2015a), Grounding line retreat of Totten Glacier, East Antarctica, 1996 to 2013, *Geophys. Res. Lett.*, *42*.

Li, X., E. Rignot, J. Mouginot, and B. Scheuchl (2015b), Mass loss of Totten Glacier, East Antarctica during the time period 1989-2015, *in preparation.*

Ligtenberg, S. R. M., M. M. Helsen, and M. R. van den Broeke (2011), An improved semi-empirical model for the densification of Antarctic firn, *The Cryosphere*, *5*(2005), 809–819.

Livingstone, S. J., C. Ó Cofaigh, C. R. Stokes, C. D. Hillenbrand, A. Vieli, and S. S. R. Jamieson (2012), Antarctic palaeo-ice streams, *Earth-Science Reviews*, *111*, 90–128.

Lythe, M. B., D. G. Vaughan, and t. B. Consortium (2001), BEDMAP: A new ice thickness and subglacial topographic model of Antarctica, *J. Geophys. Res.*, *106*(B6), 11,335–11,351.

MacAyeal, D. R. M., T. A. Scambos, C. L. Hulbe, and M. A. Fahnestock (2003), Catastrophic ice-shelf break-up by an ice-shelf-fragment-capsize mechanism, *J. Glaciol.*, *49*(164), 22–36.

Mackintosh, A. N., E. Verleyen, P. E. O'Brien, D. A. White, R. S. Jones, R. McKay, R. Dunbar, D. B. Gore, D. Fink, A. L. Post, H. Miura, A. Leventer, I. Goodwin, D. A. Hodgson, K. Lilly, X. Crosta, N. R. Golledge, B. Wagner, S. Berg, T. van Ommen, D. Zwartz, S. J. Roberts, W. Vyverman, and G. Masse (2014), Retreat history of the East Antarctic Ice Sheet since the Last Glacial Maximum, *Quaternary Science Reviews*, *100*, 10–30.

Madsen, N., H. A. Zebker, and J. Martin (1993), Topographic Mapping Using Radar Interferometry : Processing Techniques, *IEEE Trans. Geosci. Remote Sens.*, *31*(1), 246–256.

Marshall, S. (2012), *The Cryosphere*, Princeton University Press, 41 William Street, Princeton, New Jersey.

Massom, R., and D. Lubin (2006), *Polar Remote Sensing, Volume II: Ice Sheets*, Springer-Praxis, 233 Spring Street, New York City, New York.

Massom, R. a., P. T. Harris, K. J. Michael, and M. J. Potter (1998), The distribution and formative processes of latent-heat polynyas in East Antarctica, *Ann. Glaciol.*, *27*, 420–426.

Massonnet, D., and K. L. Feigl (1998), Radar interferometry and its application to changes in the Earth's surface, *Rev. Geophys.*, *36*(4), 441.

McLeod, I. H., I. G. Cumming, and M. S. Seymour (1998), ENVISAT ASAR data reduction: Impact on SAR interferometry, *IEEE Trans. Geosci. Remote Sens.*, *36*(2), 589–602.

McMillan, M., A. Shepherd, A. Sundal, K. Briggs, A. Muir, A. Ridout, A. Hogg, and D. Wingham (2014), Increased ice losses from Antarctica detected by CryoSat-2, *Geophys. Res. Lett.*, *41*, 3899–3905.

Menemenlis, D., J-M. Campin, P. Heimbach, C. Hill, T. Lee, A. Nguyen, M. Schodlok, and H. Zhang (2008), ECCO2: High resolution global ocean and sea ice data synthesis, *Mercator Ocean Quarterly Newsletter*, *31*, 13–21.

Michel, R., and E. Rignot (1999), Flow of Glaciar Moreno, Argentina, from repeat-pass Shuttle Imaging Radar images: comparison of the phase correlation method with radar interferometry, *J. Glaciol.*, *45*(149), 93–100.

Moholdt, G., L. Padman, and H. A. Fricker (2014), Basal mass budget of Ross and Filchner-Ronne ice shelves, Antarctica, derived from Lagrangian analysis of ICESat altimetry, *J. Geophys. Res.*, *119*, 2361–2380.

Moreira, A., G. Krieger, H. Fiedler, I. Hajnsek, M. Younis, M. Zink, and M. Werner (2008), Advanced interferometric SAR techniques with TanDEM-X, *2008 IEEE Radar Conf.*

Morlighem, M., E. Rignot, H. Seroussi, E. Larour, H. Ben Dhia, and D. Aubry (2011), A mass conservation approach for mapping glacier ice thickness, *Geophys. Res. Lett.*, *38*(19).

Mouginot, J., B. Scheuchl, E. Rignot, and R. Data (2012), Mapping of Ice Motion in Antarctica Using Synthetic-Aperture Radar Data, *Remote Sens.*, *4*(9), 2753–2767.

Mouginot, J., B. Scheuchl, E. Rignot, and X. Li (2014a), Monitoring Polar Ice Sheets using TanDEM-X, in *10th European Conference on Synthetic Aperture Radar (EUSAR)*, pp. 858–861.

Mouginot, J., E. Rignot, and B. Scheuchl (2014b), Sustained increase in ice discharge from the Amundsen Sea Embayment, West Antarctica, from 1973 to 2013, *Geophys. Res. Lett.*, *41*, 1576–1584.

Padman, L., S. Y. Erofeeva, and H. A. Fricker (2008), Improving Antarctic tide models by assimilation of ICESat laser altimetry over ice shelves, *Geophys. Res. Lett.*, *35*(22), L22,504.

Paolo, F. S., H. A. Fricker, and L. Padman (2015), Volume loss from Antarctic ice shelves is accelerating, *Science*, *348*(6232), 327–332.

Park, J. W., N. Gourmelen, a. Shepherd, S. W. Kim, D. G. Vaughan, and D. J. Wingham (2013), Sustained retreat of the Pine Island Glacier, *Geophys. Res. Lett.*, *40*(10), 2137–2142.

Peltier, W. (2004), Global glacial isostacy and the surface of the ice-age earth: the ICE-5G (VM2) model and GRACE, *Annual Review of Earth and Planetary Sciences*, *32*(1), 111–149.

Pope, A., T. A. Scambos, M. Moussavi, M. Tedesco, M. Willis, D. Shean, and S. Grigsby (2015), Estimating supraglacial lake depth in western Greenland using Landsat 8 and comparison with other multispectral methods, *The Cryosphere Discussions*, *9*(3), 3257–3292.

Press, W. H., S. A. Teukolsky, W. T. Vetterling, and B. P. Flannery (1992), *Numerical Recipes in C: The Art of Scientific Computing*, 2nd ed., Cambridge University Press, Cambridge, United Kingdom and New York, NY, USA.

Pritchard, H. D., R. J. Arthern, D. G. Vaughan, and L. A. Edwards (2009), Extensive dynamic thinning on the margins of the Greenland and Antarctic ice sheets, *Nature*, *461*(7266), 971–5.

Pritchard, H. D., S. R. M. Ligtenberg, H. A. Fricker, D. G. Vaughan, M. R. van den Broeke, and L. Padman (2012), Antarctic ice-sheet loss driven by basal melting of ice shelves, *Nature*, *484*(7395), 502–505.

Rack, W., and H. Rott (2004), Pattern of retreat and disintegretaion of the Larsen B Ice Shelf, *Ann. Glaciol.*, *39*, 505–510.

Ramillien, G., A. Lombard, A. Cazenave, E. Ivins, M. Llubes, F. Remy, and R. Biancale (2006), Interannual variations of the mass balance of the Antarctica and Greenland ice sheets from GRACE, *Global and Planetary Change*, *53*(3), 198–208.

Rignot, E. (1996), Tidal motion, ice velocity and melt rate of Petermann Gletscher, Greenland, measured from radar interferometry, *J. Glaciol.*, *42*(142), 476–485.

Rignot, E. (1998), Hinge-line migration of Petermann Gletscher , north Greenland , detected using satellite-radar interferometry, *J. Glaciol.*, *44*(148), 469–476.

Rignot, E. (2001), Evidence for rapid retreat and mass loss of Thwaites Glacier, West Antarctica, *J. Glaciol.*, *47*(157), 213–222.

Rignot, E. (2002), Mass balance of East Antarctic glaciers and ice shelves from satellite data, *Ann. Glaciol.*, *34*, 217–227.

Rignot, E. (2008), Changes in West Antarctic ice stream dynamics observed with ALOS PALSAR data, *Geophys. Res. Lett.*, *35*(12), 1–5.

Rignot, E., and S. S. Jacobs (2002), Rapid bottom melting widespread near Antarctic Ice Sheet grounding lines., *Science*, *296*(5575).

Rignot, E., and R. H. Thomas (2002), Mass balance of polar ice sheets, *Science*, *297*(5586), 1502–6.

Rignot, E., G. Casassa, P. Gogineni, W. Krabill, A. Rivera, and R. H. Thomas (2004), Accelerated ice discharge from the Antarctic Peninsula following the collapse of Larsen B ice shelf, *Geophys. Res. Lett.*, *31*.

Rignot, E., J. L. Bamber, M. van den Broeke, C. Davis, Y. Li, W. J. van de Berg, and E. van Meijgaard (2008), Recent Antarctic ice mass loss from radarinterferometry and regional climatemodelling, *Nat. Geosci.*, *1*(2), 106–110.

Rignot, E., J. Mouginot, and B. Scheuchl (2011a), Ice flow of the Antarctic ice sheet, *Science*, *333*, 1427–1430.

Rignot, E., J. Mouginot, and B. Scheuchl (2011b), Antarctic grounding line mapping from differential satellite radar interferometry, *Geophys. Res. Lett.*, *38*(10), 1–6.

Rignot, E., S. Jacobs, J. Mouginot, and B. Scheuchl (2013), Ice Shelf Melting Around Antarctica, *Science*, (June).

Rignot, E., J. Mouginot, M. Morlighem, H. Seroussi, and B. Scheuchl (2014), Widespread, rapid grounding line retreat of Pine Island, Thwaites, Smith, and Kohler glaciers, West Antarctica, *Geophys. Res. Lett.*, *41*, 3502–3509.

Riva, R. E. M., B. C. Gunter, T. J. Urban, B. L. a. Vermeersen, R. C. Lindenbergh, M. M. Helsen, J. L. Bamber, R. S. W. van de Wal, M. R. van den Broeke, and B. E. Schutz (2009), Glacial Isostatic Adjustment over Antarctica from combined ICESat and GRACE satellite data, *Earth Planet. Sci. Lett.*, *288*(3-4), 516–523.

Roberts, J., C. Plummer, T. Vance, T. van Ommen, A. Moy, S. Poynter, A. Treverrow, M. Curran, and S. George (2015), A two thousand year annual record of snow accumulation rates for Law Dome, East Antarctica, *Clim. Past*, *11*, 697–707.

Roberts, J. L., R. C. Warner, D. A. Young, a. Wright, T. van Ommen, D. D. Blankenship, M. Siegert, N. Young, I. E. Tabacco, A. Forieri, a. Passerini, A. Zirizzotti, and M. Frezzotti (2011), Refined broad-scale sub-glacial morphology of Aurora Subglacial Basin, East Antarctica derived by an ice-dynamics-based interpolation scheme, *The Cryosphere*, *5*(1), 655–684.

Rose, K. E. (1979), Characteristics of Ice Flow in Marie Byrd Land , Antarctica, *J. Glaciol.*, *24*(90), 63–75.

Rosen, P. A., S. Hensley, I. R. Joughin, F. K. Li, S. N. Madsen, E. Rodriguez, and R. M. Goldstein (2000), Synthetic aperture radar interferometry, *P. IEEE*, *88*(3), 333–382.

Rosen, P. A., S. Hensley, and C. Chen (2010), Measurement and mitigation of the ionosphere in L-band Interferometric SAR data, *P. IEEE Radar Conf.*, pp. 1459–1463.

Rott, H., F. Müller, T. Nagler, and D. Floricioiu (2011), The imbalance of glaciers after disintegration of Larsen-B ice shelf, Antarctic Peninsula, *Cryosphere*, *5*, 125–134.

Scambos, T., M. J. Dutkiewicz, J. C. Wilson, and R. A. Bindschadler (1992), Application of image cross-correlation to the measurement of glacier velocity using satellite image data, *Remote Sensing of Environment*, *42*, 177–186.

Scambos, T., T. M. Haran, M. Fahnestock, T. H. Painter, and J. Bohlander (2007), MODIS-based Mosaic of Antarctica (MOA) data sets: Continent-wide surface morphology and snow grain size, *Remote Sens. Environ.*, *111*(2-3), 242–257.

Scambos, T. a., J. a. Bohlander, C. a. Shuman, and P. Skvarca (2004), Glacier acceleration and thinning after ice shelf collapse in the Larsen B embayment, Antarctica, *Geophys. Res. Lett.*, *31*(18).

Schaum, A., and M. McHugh (1991), Analytic methods of image registration: Displacement estimation and resampling, *Naval Research Laboratory Report*.

Scheuchl, B., J. Mouginot, and E. Rignot (2012), Ice velocity changes in the Ross and Ronne sectors observed using satellite radar data from 1997 and 2009, *The Cryosphere*, *6*(5), 1019–1030.

Schoof, C. (2007a), Ice sheet grounding line dynamics: Steady states, stability, and hysteresis, *J. Geophys. Res.*, *112*.

Schoof, C. (2007b), Marine ice-sheet dynamics. Part 1. The case of rapid sliding, *J. Fluid Mech.*, *573*, 27.

Seroussi, H., M. Morlighem, E. Rignot, E. Larour, D. Aubry, H. Ben Dhia, and S. S. Kristensen (2011), Ice flux divergence anomalies on 79north Glacier, Greenland, *Geophys. Res. Lett.*, *38*(9).

Shepherd, A., and D. Wingham (2007), Recent sea-level contributions of the Antarctic and Greenland ice sheets, *Science*, *315*(5818), 1529–32.

Shepherd, A., D. Wingham, and E. Rignot (2004), Warm ocean is eroding West Antarctic Ice Sheet, *Geophys. Res. Lett.*, *31*(23), 4–7.

Shreve, R. L. (1972), Movement of water in glaciers, *J. Glaciol.*, *11*, 205–214.

Smith, A. M. (1991), The Use of Tiltmeters to Study the Dynamics of Antarctic Ice-Shelf Grounding Lines, *J. Glaciol.*, *37*(125), 51–58.

Stein, M. L. (1999), *Interpolation of Spatial Data: Some Theory for Kriging*, Springer, 233 Spring Street, New York City, New York.

Sun, S., S. L. Cornford, Y. Liu, and J. C. Moore (2014), Dynamic response of Antarctic ice shelves to bedrock uncertainty, *The Cryosphere*, *8*, 1561–1576.

Sutterley, T. C., I. Velicogna, E. Rignot, J. Mouginot, T. Flament, M. R. van den Broeke, J. M. van Wessem, and C. H. Reijmer (2014), Mass loss of the Amundsen Sea Embayment of West Antarctica from four independent techniques, *Geophys. Res. Lett.*, *41*(23), 8421–8428.

Tamura, T., K. I. Ohshima, and S. Nihashi (2008), Mapping of sea ice production for Antarctic coastal polynyas, *Geophys. Res. Lett.*, *35*(7).

Thomas, R. H. (1979), The Dynamics of Marine Ice Sheets, *J. Glaciol.*, *24*(90).

Thomas, R. H., E. Rignot, G. Casassa, P. Kanagaratnam, C. Acuna, T. Akins, H. Brecher, E. Frederick, P. Gogineni, W. Krabill, S. Manizade, H. Ramamoorthy, A. Rivera, R. Russell, J. Sonntag, R. Swift, J. Yungel, and J. Zwally (2004), Accelerated sea-level rise from West Antarctica, *Science*, *306*(5694), 255–258.

Tsai, V. C., and G. H. Gudmundsson (2015), An improved model for tidally-modulated grounding-line migration, *J. Glaciol.*, *61*(226), 216–222.

Turner, J., S. R. Colwell, G. J. Marshall, T. a. Lachlan-Cope, A. M. Carleton, P. D. Jones, V. Lagun, P. a. Reid, and S. Iagovkina (2004), The SCAR READER project: Toward a high-quality database of mean Antarctic meteorological observations, *J. Clim.*, *17*(14), 2890–2898.

van de Berg, W. J., M. van den Broeke, C. H. Reijmer, and E. van Meijgaard (2006), Reassessment of the Antarctic surface mass balance using calibrated output of a regional atmospheric climate model, *J. Geophys. Res.*, *111*.

van der Veen, C. J. (2013), *Fundamentals of Glacier Dynamics*, 2nd ed., CRC Press, Taylor & Francis Group, 6000 Broken Sound Parkway NW, Suite 300, Boca Raton, Florida.

van Ommen, T. D., and V. Morgan (2010), Snowfall increase in coastal East Antarctica linked with southwest Western Australian drought, *Nature Geoscience*, *3*(4), 267–272.

van Wessem, J. M., C. H. Reijmer, M. Morlighem, J. Mouginot, E. Rignot, B. Medley, I. Joughin, B. Wouters, M. A. Depoorter, J. L. Bamber, J. T. M. Lenaerts, W. J. De Van Berg, M. Van Den Broeke, and E. Van Meijgaard (2014), Improved representation of East Antarctic surface mass balance in a regional atmospheric climate model, *J. Glaciol.*, *60*(222), 761–770.

Vaughan, D. G. (1994), Investigating tidal flexure on an ice shelf using kinematic GPS, *Ann. Glaciol.*, *20*, 372–376.

Vaughan, D. G. (1995), Tidal Flexure at Ice Shelf Margins, *J. Geophys. Res.*, *100*(B4), 6213–6224.

Velicogna, I. (2009), Increasing rates of ice mass loss from the Greenland and Antarctic ice sheets revealed by GRACE, *Geophys. Res. Lett.*, *36*.

Velicogna, I., and J. Wahr (2006), Measurements of Time-Variable Gravity Show Mass Loss in Antarctica, *Science*, *311*, 1754–1756.

Velicogna, I., and J. Wahr (2013), Time-variable gravity observations of ice sheet mass balance: Precision and limitations of the GRACE satellite data, *Geophys. Res. Lett.*, *40*(12), 3055–3063.

Velicogna, I., T. C. Sutterley, and M. R. van den Broeke (2014), Regional acceleration in ice mass loss from Greenland and Antarctica using GRACE time-variable gravity data, *Geophys. Res. Lett.*, *41*(22), 8130–8137.

Weertman, J. (1957), Deformation of floating ice shelves, *J. Glaciol.*, *3*(21), 38–42.

Weertman, J. (1974), Stability of the junction of an ice sheet and an ice shelf, *J. Glaciol.*, *13*(67), 3–11.

Williams, G., A. J. S. Meijers, A. Poole, P. Mathiot, T. Tamura, and A. Klocker (2011), Late winter oceanography off the Sabrina and BANZARE coast (117128E), East Antarctica, *Deep-Sea Res. Pt II*, *58*(9-10), 1194–1210.

Williams, S. D., P. Moore, M. a. King, and P. L. Whitehouse (2014), Revisiting GRACE Antarctic ice mass trends and accelerations considering autocorrelation, *Earth Planet. Sci. Lett.*, *385*, 12–21.

Wingham, D., A. Ridout, R. Scharroo, R. Arthern, and C. Shum (1998), Antarctic elevation change from 1992 to 1996, *Science*, *282*, 1996–1999.

Young, D. A., A. P. Wright, J. L. Roberts, R. C. Warner, N. W. Young, J. S. Greenbaum, D. M. Schroeder, J. W. Holt, D. E. Sugden, D. D. Blankenship, T. D. van Ommen, and M. J. Siegert (2011), A dynamic early East Antarctic Ice Sheet suggested by ice-covered fjord landscapes., *Nature*, *474*(7349), 72–5.

Young, D. A., L. E. Lindzey, D. D. Blankenship, J. S. Greenbaum, A. G. D. E. Gorordo, S. D. Kempf, J. L. Roberts, R. C. Warner, T. van Ommen, M. J. Siegert, and E. L. E. Meur (2015), Instruments and Methods: Land-ice elevation changes from photon-counting swath altimetry: first applications over the Antarctic ice sheet, *J. Glaciol.*, *61*(225), 17–28.

Young, N. (1979), Measured velocities of interior East Antarctica and the state of mass balance within the I.A.G.P. Area, *J. Glaciol.*, *24*(90), 77–87.

Zwally, H. J., J. Li, J. W. Robbins, J. L. Saba, D. Yi, and A. C. Brenner (2015), Mass gains of the Antarctic ice sheet exceed losses, *J. Glaciol.*, *61*(230), 1019–1036.

Zwally, J., M. B. Giovinetto, J. Li, H. G. Cornejo, M. A. Beckley, A. C. Brenner, J. L. Saba, and D. Yi (2005), Mass changes of the Greenland and Antarctic ice sheets and shelves and contributions to sea-level rise: 1992-2002, *J. Glaciol.*, *51*(175), 509–527.